# Absorption of Greenhouse Gases in Liquids

A Molecular Approach

# Absorption of Greenhouse Gases in Liquids

A Molecular Approach

## Proefschrift

ter verkrijging van de graad van doctor
aan de Technische Universiteit Delft,
op gezag van de Rector Magnificus prof. ir. K. C. A. M. Luyben,
voorzitter van het College voor Promoties,
in het openbaar te verdedigen op maandag, 23 november 2015 om 15:00 uur

door

**Sayee Prasaad Balaji**

Master of Science, Hamburg University of Technology,
geboren te Chennai, India.

Dit proefschrift is goedgekeurd door de promotoren:

| | |
|---|---|
| Promotor: | Prof. dr. ir. Thijs J. H. Vlugt |
| Copromotor: | Dr. David Dubbeldam |

Samenstelling promotiecommissie:

| | |
|---|---|
| Rector Magnificus, | voorzitter |
| Prof. dr. ir. T. J. H. Vlugt, | Technische Universiteit Delft, promotor |
| Dr. D. Dubbeldam, | Universiteit van Amsterdam, copromotor |

Onafhankelijke leden:

| | |
|---|---|
| Prof. dr. B. J. Thijsse, | Technische Universiteit Delft |
| Prof. dr. ir. B. De Schutter, | Technische Universiteit Delft |
| Prof. dr. E. J. Meijer, | Universiteit van Amsterdam |
| Prof. dr. H. Zuilhof, | Universiteit Wageningen |
| Prof. dr. S. Calero, | Universidad-Pablo de Olavide Sevilla |

This research is supported by the CATO-2 program, the Dutch national R&D program on $CO_2$ capture, transport and storage funded by the Dutch Ministry of Economic Affairs. In addition, this work was supported by NWO Exacte Wetenschappen (Physical Sciences) for the use of supercomputing facilities, with financial support from the Nederlandse Organisatie voor Wetenschappelijk Onderzoek (Netherlands Organization for Scientific Research, NWO).



*Keywords:* Molecular simulations, carbon dioxide capture, liquid solvents

*Printed by:* Ipskamp Drukkers BV, The Netherlands

*Front & Back:* S. P. Balaji



ISBN/EAN 978-94-6186-543-4

An electronic version of this dissertation is available at
`http://repository.tudelft.nl/`.

ॐ अज्ञान-तिमिरान्धस्य ज्ञानाञ्जन-शलाकया ।
चक्षुरुन्मीलितं येन तस्मै श्री गुरवे नमः ॥

*Dedicated to all my Teachers*

# Contents

# 1

# Introduction

## 1.1 The Need for $CO_2$ Capture

The advent of the industrial revolution in the 18th century brought about the use of fossil fuels to satisfy the demand in energy [1–5]. The combustion of these fossil fuels release greenhouse gases like carbon dioxide, oxides of nitrogen, sulphur into the atmosphere. According to the fifth assessment report of the Intergovernmental Panel on Climate Change (IPCC) [1, 3], the increase in concentration of these greenhouse gases in the atmosphere has resulted in global warming. Global warming is characterized by warming up of the atmosphere and water bodies, melting of the polar ice caps and increase in sea water levels. Increasing concentrations of carbon dioxide ($CO_2$) have led to an average increase in global temperatures of the earth's atmosphere and oceans.

Rising demand for energy stems from the worldwide economic growth and development [6]. The energy sector is responsible for the release of around 70% of the anthropogenic greenhouse gases into the atmosphere [2, 3]. Fossil fuels account for 82% of the global total energy supply. In 2012, global $CO_2$ emissions were measured to be 31.7 Giga ton $CO_2$ [2, 3]. Effluent gases from power plants and industries account for the majority of the global carbon dioxide emissions into the atmosphere [3]. In order to mitigate the effects of climate change and to lower the global average temperatures, the emissions of greenhouse gases, mainly $CO_2$, must be reduced [1]. Carbon Capture and Storage (CCS) is one of the important methods to reduce the emissions of $CO_2$ in the atmosphere. CCS describes a set of technologies which can be used to collect $CO_2$ from industrial processes and power generation. This captured $CO_2$ is then separated and purified and then it is transported and compressed to a form suitable for storage. This compressed form of $CO_2$ is stored in a storage site which is usually situated underground in geological formations [4, 5, 7]. The different $CO_2$ capture methods are shown schematically in Fig. 1.1 and they are explained in detail below.

### 1.1.1. Pre-combustion $CO_2$ Capture

Pre-combustion capture refers to the capture of $CO_2$ from fossil fuels before combustion. In the pre-combustion capture process, fossil fuel is converted to gaseous fuel through a high temperature process known as gasification. The fossil fuel, usually

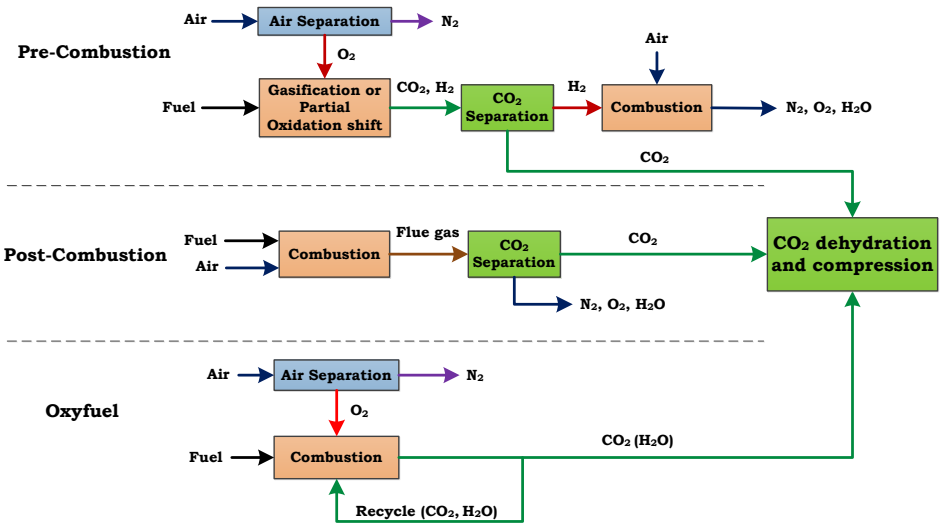


Figure 1.1: An overview of the different $CO_2$ capture methods from the combustion of fossil fuels. Pre-combustion $CO_2$ capture method is when the capture of $CO_2$ takes place prior to the combustion of fossil fuels [4, 5, 8]. Post-combustion $CO_2$ capture is the capture of $CO_2$ from flue gas streams produced by combustion of fossil fuels [9–12]. Oxyfuel combustion is when $CO_2$ is captured from $CO_2$ rich streams produced from combustion in presence of a pure oxygen stream [5, 13, 14].

coal or heavy residue, undergoes a partial oxidation to produce synthesis gas which mainly comprises of carbon monoxide (CO) and hydrogen ($H_2$) along with $CO_2$, methane, hydrocarbons and other compounds at high pressures. This synthesis gas then undergoes a water-gas shift reaction where the CO reacts with the steam to produce $CO_2$ and $H_2$.

$$CO + H_2O \rightleftharpoons CO_2 + H_2 \tag{R1}$$

The generated $CO_2$ can be removed using absorption using physical solvents [4, 5, 8], pressure swing adsorption [4, 5, 15, 16] or membranes [17]. The captured $CO_2$ is later recovered and transported to various sites to be stored.

### 1.1.2. Post-combustion $CO_2$ Capture

Post-combustion $CO_2$ capture refers to the capture of $CO_2$ from the flue gas streams that are produced by combustion of fossil fuels like coal, natural gas or biomass. These "huge volume" flue gas streams have low $CO_2$ partial pressures and also contain other contaminants like $SO_x$ and $NO_x$. Absorption processes using chemical solvents are widely used in the industry for the removal of $CO_2$ from flue gas [9, 10, 18, 19]. The chemisorption process is economical in principle and provides the option to retrofit existing industries without major modifications to the plant setup [20]. Chemisorption processes have high selectivities and capacities towards capturing $CO_2$ at atmospheric pressures but require high energies to regenerate

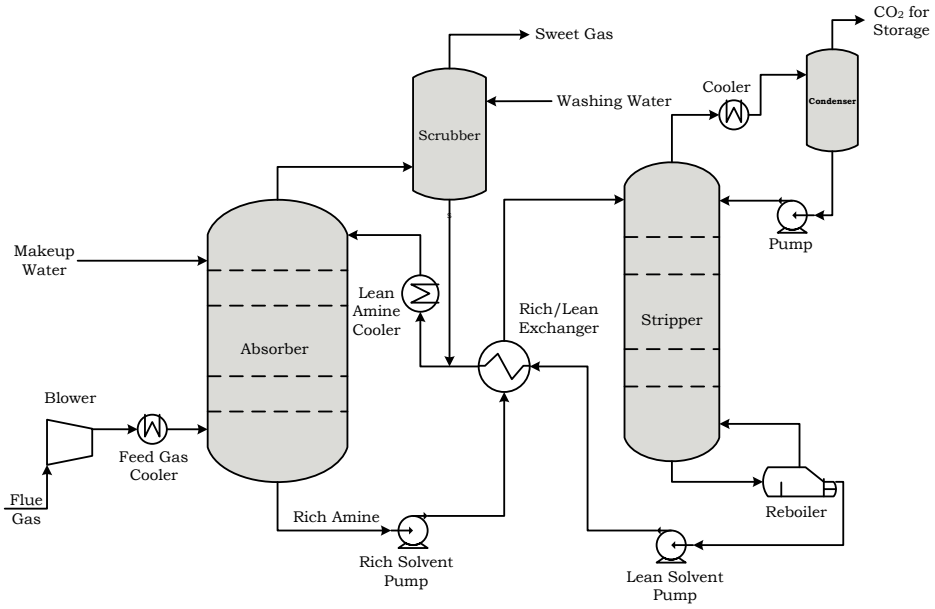


Figure 1.2: Process flow scheme of a chemisorption based post-combustion $CO_2$ capture plant [11, 12, 20]. The flue gas rich in $CO_2$ enters the absorber where it is contacted with the lean amine solvent. After the chemisorption of $CO_2$ with the amine solvent, the $CO_2$ free flue gas is let off into the atmosphere. The $CO_2$ rich amine solvent is pumped to the stripper column where the amine solvent is regenerated by the application of heat energy. The lean amine solvent is circulated back to the absorber while the $CO_2$ is collected in the condenser to be compressed for storage [11, 12].

the $CO_2$ from the rich solvent [8, 11, 12]. The $SO_x$ and $NO_x$ are usually removed to acceptable levels in a pre-treatment process before the actual chemisorption of $CO_2$ takes place. Other methods for post-combustion $CO_2$ capture include adsorption using zeolites, metal organic frameworks, membrane separations, etc. are still in the development phase [7, 21–25]. A typical absorption-desorption based post-combustion $CO_2$ capture process is shown in Fig. 1.2.

The flue gas from the coal-fired power plant is cooled and is pre-treated to remove the $SO_2$ before it enters the absorber. In the absorption column, the flue gas, rich in $CO_2$, comes into contact with the lean chemical solvent. Monoethanolamine is one of the most widely used solvents in the industry to capture $CO_2$ [11, 12]. $CO_2$ from the flue gas reacts with the amine and the $CO_2$ rich amine solvent is pumped to the stripper column via a heat exchanger which preheats the rich amine solvent. In the stripper/regenerator, heat is supplied to the rich solvent and the desorption of $CO_2$ from the amine solvent takes place. The lean solvent is pumped back to the absorber and the $CO_2$ stream gets collected in the condenser to be compressed for storage.

1

### 1.1.3. Oxyfuel Combustion

Oxyfuel combustion involves the burning of hydrocarbon fossil fuel in the presence of pure oxygen. The flue gas resulting from the products of combustion are primarily $CO_2$ and water vapor along with gases like argon and nitrogen as contaminants.

$$C(\text{fossilfuel}) + O_2 \rightarrow CO_2 \quad \text{(R2)}$$

$$4H(\text{fossilfuel}) + O_2 \rightarrow 2H_2O \quad \text{(R3)}$$

The heat released from combustion is used to produce steam which in turn runs the turbines to generate electricity. The flue gas is cooled to condense the water vapor which results in a highly concentrated $CO_2$ stream [5, 13, 14]. The $CO_2$ can then be compressed and transferred for storage. One of the methods to achieve oxyfuel combustion is the chemical looping mechanism where a metal/metal oxide is used to "carry" the oxygen from an air stream to a fuel reactor. The oxygen produced this way is cheaper and less energy intensive [26].

## 1.2 Solvents for $CO_2$ Capture

Post-combustion $CO_2$ capture is a mature technology which can be implemented in fossil fuel fired power plants without significant changes to the plant setup [20]. Conventionally, both physical and chemical solvents have been proposed for use in $CO_2$ capture [10, 15, 19]. Physical solvents maybe used in the pre-combustion $CO_2$ capture method where the partial pressure of the $CO_2$ is quite high [8]. Physical solvents like dimethyl ethers of polyethylene glycol (Selexol), methanol (Rectisol), N-methyl 2-pyrrolidone (Purisol), propylene carbonate (Fluor solvent) are commercially available for separating $CO_2$ from gas mixtures [8]. For post-combustion $CO_2$ capture, chemical solvents are mostly preferred since the partial pressure of $CO_2$ in the flue gas streams is quite low [8, 10, 11, 15]. Traditionally, amine solvents are used in industries for acid gas treatment of effluent gas streams since they have high reactivity with $CO_2$ [27, 28]. Primary and secondary amines react with $CO_2$ to form carbamates, while tertiary and sterically hindered amines predominantly form bicarbonates [18]. Monoethanolamine (MEA) is the most commonly used industrial solvent which has been used for more than sixty years in process plants for sweetening sour gases [11, 12]. The advantages of using MEA as a solvent is the high reactivity with $CO_2$ leading to high $CO_2$ solubilities, low solvent cost, and low molecular weight [29–35]. However, MEA is volatile, corrosive, subjected to degradation and requires high energy to regenerate the solvent [36, 37]. Other solvents like methyldiethanolamine (MDEA) are also used for $CO_2$ capture. MDEA is a tertiary amine and forms bicarbonates which increases the capacity for $CO_2$ absorption. As MDEA is a tertiary amine, it suffers from reduced reactivity with $CO_2$ [30, 33, 38–41]. Sterically hindered solvents like 2-amino-2-methyl-1-propanol (AMP) are also used for $CO_2$ capture in the industry. AMP has a higher capacity of $CO_2$ absorption due to the formation of bicarbonates. AMP also suffers from low reactivity with $CO_2$ [35, 42–44]. A promoter, like piperazine (PZ), is added to AMP to increase the reactivity of $CO_2$ in AMP [41, 45, 46]. There are other new materials which have been studied in recent times to capture $CO_2$: zeolites [7, 25],

metal-organic frameworks (MOFs), zeolitic imidazolate frameworks (ZIFs) [23, 24], metal oxides [7, 25], ionic liquids [8, 47–49], etc. Many of these new materials are promising, since they can be tailor-made to suit certain conditions, but are not suited for $CO_2$ capture from industrial flue gases due to high costs, instability when in contact with water, etc. Liquid solvents still remain the most preferred choice in chemical industries for $CO_2$ capture from flue gases.

## 1.3 Need for New Solvents

It is inevitable that fossil fuel based power plants are required to fill the gap between the demand for power and use of renewable sources of energy [1, 3]. CCS remains one of the most attractive and feasible processes to decrease the amount of greenhouse gases in the atmosphere to mitigate global warming. Since fossil fuel powered power plants emit most greenhouse gases, there is a need for a reliable and efficient post-combustion $CO_2$ capture technology to be implemented in these power plants to capture the $CO_2$ from the effluent flue gas [20]. Chemical solvents available in the industry require energy to regenerate the solvents and therefore makes the CCS process expensive [36, 37]. It is imperative that new solvents are formulated which are less energy intensive and less toxic and less corrosive than the existing ones. There might exist millions of structures which can be used for $CO_2$ capture, but to select the most promising ones is extremely difficult and time consuming. Experimental approaches to this issue include synthesizing new molecules and studying the solubilities, diffusivities of $CO_2$ in the solvents, which are time consuming and challenging. An alternate approach is to use a pre-screening tool to potentially screen out few solvent structures from the database [50]. This pre-screening tool should take into account the thermodynamic processes that take place during the chemisorption/physisorption of $CO_2$ in solvents. In this thesis, we discuss the role of molecular simulations in describing the thermodynamic processes that take place during chemisorption of $CO_2$ with liquid solvents.

## 1.4 Molecular Simulation

The emergence of computational power since the Second World War has spurred the growth of computer simulations [51]. Computer simulations use models to study behaviours of a system. They are used in many applications in the fields of chemistry, physics, weather forecasting, engineering, etc [51–55]. Computational methods are useful in solving complex problems where analytical solutions cannot be applied. With the advent of computational methods, it is possible to support or reinterpret experimental observations and also to understand fundamental processes from a molecular perspective [51, 54]. To make rapid advancements in developing new catalysts, solvents, organic electronics, new pharmaceutical drugs, etc. a molecular understanding of absorption, reaction and diffusion processes is important. Molecular simulations model the microscopic interactions of the system to obtain the macroscopic properties that are of interest. Molecular modeling methods can be classified into two broad categories: ab-initio and semi-empirical electronic structure calculations and molecular mechanics [52]. Ab-initio methods are based upon

quantum mechanics and describe the electronic structures of molecules and their reactivities. Ab-initio methods are very accurate and extremely computer intensive. Molecular mechanics methods are based on the principles of classical physics and as such are computationally fast. Molecular mechanics neglect the explicit treatment of the electronic structures and provide more efficient means to determine bulk properties [52, 53].

Classical molecular simulations are used in predicting the behaviour of large systems. Classical molecular simulations neglect the explicit treatment of electrons and rely only on laws of classical physics to predict the chemical properties of the molecules [51, 53, 56]. Classical simulations compute values of thermodynamic properties by simulating microscopic representative configurations of the macroscopic systems. Some of the properties to be computed depend on the positions of the molecules and/or their momenta. The properties fluctuate as a function of time depending on the interactions of the atoms/molecules. The interactions between atoms/molecules are described by a force field [53]. The force field consists of a functional form and parameter sets based on the positions of the atoms and parameter sets to calculate the potential energy of the system. The functional form of the force fields includes non-bonded interactions and bonded interactions. The non-bonded interactions include the van der Waals and electrostatic interactions [53]. The Lennard-Jones potential is commonly used for the computation of the van der Waals interactions and repulsions [53]:

$$u_{\mathrm{LJ}} = 4\epsilon \left[ \left(\frac{\sigma}{r}\right)^{12} - \left(\frac{\sigma}{r}\right)^{6} \right] \tag{1.1}$$

where $u$ is the interatomic potential energy, $\sigma$ is the finite distance at which the inter-particle potential is zero, $\epsilon$ is the depth of the potential well, and $r$ is the distance between the particles. Bonded interactions include the energies of bond stretching, bending, torsion and intra-molecular Lennard-Jones interactions. The value of the force field parameters are usually obtained from different methods. Bonded interactions are usually obtained from quantum mechanical simulations while Lennard-Jones parameters are usually obtained by fitting to experimental data [53, 57–64].

There are two approaches to performing classical molecular simulations: Monte Carlo and Molecular Dynamics simulations. Monte Carlo simulations, which are stochastic in nature, sample configuration states to probe the potential energy surface [51, 53]. The second method, called Molecular Dynamics, simulates the time evolution of the molecular system to provide the trajectory of the system [51, 53]. Macroscopic systems are described by the partition function $Q$, which can be a function of the number of particles $N$, volume $V$, temperature $T$ (for a canonical system) [52–54]. For a complete understanding in molecular simulations, the reader is referred to several textbooks on this subject [51, 53, 54, 56].

Monte Carlo (MC) simulations computes macroscopic properties of a system by sampling configurations from a chosen statistical ensemble [53]. There are a huge number of possible configuration states that are available and it is practically impossible to compute the energy of all of them. Most of these configuration

states have statistically zero weight in the partition function and relatively only few states have significant non-zero weights. It is therefore advantageous to generate configurations with a weight that is proportional to the statistical weight for a partition function [51, 53]. This is called importance sampling. Using the method of importance sampling, the Metropolis algorithms generates random configurations according to the Boltzmann distribution [65]. From an initial configuration in configuration space, a proposed Monte Carlo trial move is generated resulting in a new configuration. The new configuration is accepted or rejected according to the Boltzmann factor. Monte Carlo methods can be used to compute phase diagrams, pressures, densities, free energies [53, 56].

Molecular Dynamics (MD) simulations are able to calculate the time averages of properties by numerically solving the Newton's equations of motion [53]. From the spatial derivative of the potential energy, the force on the molecule can be calculated and the system is integrated to obtain positions and velocities at the new time step [53]. Given the positions, masses and forces of the molecules in the system, representative single particle trajectories can be calculated. Molecular Dynamics is predominantly a deterministic method, which means that the state of the system at any future time can be calculated from the current state. The evolution of the molecular system is studied as a series of snapshots taken at close time intervals. This integration is repeated many times to obtain trajectories over a specified time interval. Average properties can be calculated from these atomic or molecular trajectories. In order to maintain constant temperatures and/or pressures, appropriate thermostats and/or barostats are used [53]. MD simulations can be used to compute dynamic properties like diffusion, heat conductivities, viscosities [51, 53].

The main aim of the thesis is to understand the various thermodynamic processes that occur when greenhouse gases like $CO_2$ are captured using a chemical solvent. Understanding the thermodynamic processes taking place during chemisorption help in studying the effects of solvents on the absorption/desorption of $CO_2$ in the solvents and their constituent reactions. Ultimately, these aid in developing new solvents that have high capacity to absorb $CO_2$ and low energy penalties to regenerate the $CO_2$ rich solvents. Some of the thermodynamic processes that take place are absorption/desorption from the gas phase, the reaction of $CO_2$ with the aqueous solvent and the diffusion of $CO_2$ molecules into the aqueous solvent mixture. Understanding these processes can help in developing a screening tool that can predict the solubilities, equilibrium constants and conversions, diffusivities of $CO_2$ in different solvents. Molecular simulations can be used in this regard to great effect. Monte Carlo simulations can be used to study equilibrium conversions of the different species in the reacting mixture with great efficiency and accuracy [66–69]. They can also measure the absorption/desorption of $CO_2$ from the gas phase into the solvent [49, 70, 71]. Molecular Dynamics simulations can help calculate diffusion coefficients of $CO_2$ in the reacting mixture [71]. The high accuracies and efficiencies of molecular simulations make it an attractive tool in designing new solvents which are more efficient, less toxic and less corrosive than the ones that are available in the market.

1

## 1.5 Scope and Outline of this Thesis

The overall aim of this thesis is to understand the various thermodynamic processes (*i.e.* solubility and diffusion) that take place during the absorption of greenhouse gases in liquid solvents. In more detail, this means:

1. To develop advanced Monte Carlo methods to compute the thermodynamic factors which are used to calculate Fick diffusivities for multicomponent systems

2. To develop advanced Monte Carlo methods to efficiently simulate open ensemble systems and to study the reactions of $CO_2$ in liquid solvents like aqueous monoethanolamine

3. To validate the so-called "$CO_2/N_2O$ analogy" used to obtain diffusivities and Henry coefficients in chemical solvents using molecular simulations

4. To obtain physical solubilities of pre-combustion gases in complex solvents using advanced Monte Carlo methods

In chapter 2, a new method called Permuted Widom Test Particle Insertion (PWTPI) method is introduced and discussed in detail. In chemical industries, the knowledge of the values of Fick diffusion coefficients is essential in order to design separation equipment. It is very difficult to obtain the Fick diffusivities for multicomponent systems from Fick's laws as multicomponent Fick diffusivities are unrelated to their binary counterparts [72]. The Maxwell-Stefan approach is a thermodynamically more correct approach and the Maxwell-Stefan diffusivities usually depend less on the concentration [72, 73]. Maxwell-Stefan diffusivities can be calculated from molecular simulations [74, 75]. Since both Fick's laws and Maxwell-Stefan theory describe the same diffusion process, the value of the diffusion coefficients can be related using the so-called thermodynamic factor [72, 73, 76]. Existing methods to calculate these thermodynamic factors from experiments and molecular simulations are either inaccurate or require a non-trivial interpretation of the results from simulations. In this regard, the PWTPI method is developed which can calculate the matrix of thermodynamic factors from a single simulation without any additional computational cost. The PWTPI method has been used to validate the application of the newly developed Kirkwood-Buff theory in closed systems to ionic species.

Chemisorption of $CO_2$ in a chemical solvent involves the transfer of $CO_2$ molecules to/from the gas phase to the liquid phase and the reactions of $CO_2$ with the chemical solvent. Existing methods are inefficient to handle simulations of the chemisorption process, since probability of successful insertions and deletions of molecules in a dense system is extremely low [77]. The Continuous Fractional Component Monte Carlo method (CFCMC) was developed by Maginn *et al.* [78, 79] to increase the efficiency of the insertions/deletions. In chapter 3, the CFCMC has been compared with the well-known Configurational-Bias Monte Carlo (CBMC) at high densities. A new hybrid method Configurational-Bias/Continuous Fractional Component Monte Carlo (CB/CFCMC) which combines the CBMC and the CFCMC methods is proposed. This CB/CFCMC method is also compared with the CBMC and the CFCMC

in high densities as well as in complex systems. The CB/CFCMC method is found to be more efficient than the CBMC and CFCMC at medium to high densities since it combines the "biased growth" of the CBMC with the insertion/deletion of the "fractional molecule" in the CFCMC.

To model the chemisorption of the $CO_2$ in a chemical solvent, it is necessary to model the reactions of the $CO_2$ with the liquid solvent and to study the impact of different reaction pathways on the equilibrium concentrations of all the species in the reacting mixture. Chapter 4 discusses the Reaction Ensemble Monte Carlo using the Continuous Fractional Component method (RxMC/CFC) which is developed to obtain the different equilibrium concentrations of $CO_2$ reacting with aqueous MEA solutions using classical molecular simulations [66–68, 80, 81]. The effect of different reaction pathways can be studied using this RxMC/CFC method and also opens up the possibilities to investigate effects of different solvents in the reactions. This RxMC/CFC method along with the CFCMC method in the osmotic ensemble is used to compute the solubilities of $CO_2$ in aqueous MEA solutions.

It is imperative to study the diffusion and physical solubility of $CO_2$ molecules in aqueous amine solutions in order to obtain the Fick diffusivities and the Henry's constant respectively. The diffusivities and the Henry's constant of $CO_2$ in amine solvents are extremely difficult to calculate using experiments since the reactions and diffusion of $CO_2$ take place simultaneously and there is almost no unreacted $CO_2$ [39, 82]. The so-called "$CO_2/N_2O$ analogy" has been used to calculate these physical constants by substituting $CO_2$ with the molecularly similar $N_2O$ [32, 82]. In chapter 5, molecular simulations are used to validate the "$CO_2/N_2O$ analogy". Diffusivities and solubilities of $CO_2$ in various solvents can be computed using classical molecular simulations and compared to the diffusivities and solubilities obtained using the "$CO_2/N_2O$ analogy".

In chapter 6, the physical solubilities of gases in physical solvents are studied. The Continuous Fractional Component Monte Carlo method (CFCMC) [70, 78, 79] in open ensemble is used to study the physical solubilities of various gases in ionic liquids (ILs) and compared to experimental results. The success of these simulations in predicting the physical solubilities in complex solvents like ILs can be exploited in pre-screening potential solvents for pre-combustion $CO_2$ capture as well.

# 2

# Calculating Thermodynamic Factors for Multicomponent Liquid Mixtures

Parts of this chapter is based on (1) S.P. Balaji, S.K. Schnell, E.S. McGarrity, T.J.H. Vlugt, *A direct method for calculating thermodynamic factors for liquid mixtures using the Permuted Widom test particle insertion method*, Mol. Phys. **2012**, 111(2), 287-296 [83]; (2) S.P. Balaji, S.K. Schnell, T.J.H. Vlugt, *Calculating thermodynamic factors of ternary and multicomponent mixtures using the Permuted Widom test particle insertion method*, Theo. Chem. Acc. **2013**, 132(3), 1-8 [84]; (3) S.K. Schnell, P. Englebienne, J.M. Simon, P. Krüger, S.P. Balaji, S. Kjelstrup, D. Bedeaux, A. Bardow, T.J.H. Vlugt, *How to apply the Kirkwood–Buff theory to individual species in salt solutions*, Chem. Phys. Lett. **2013**, 582, 154-157 [85]

## 2.1 Introduction

Understanding mass transfer in multicomponent systems is important as it plays an important role in many industrial processes [86–92]. Since diffusion-controlled reactions are often prevalent in chemical processes and separations involving a liquid phase, knowledge of the diffusion coefficients for ternary and multicomponent mixtures is very relevant due to their frequent use in industrial processes [72, 87, 91, 92]. To describe mass transport by diffusion in liquid mixtures, both the Maxwell-Stefan theory and extensions to Fick laws are used. Maxwell-Stefan diffusivities can be obtained directly from Molecular Dynamics simulations [74, 75] and theory, while Fick diffusivities are obtained from experiments [72, 73, 93]. Fick's law for an $n$-component system in a molar reference frame is given by [87]

$$J_i = -c \sum_{k=1}^{n-1} D_{ik}^{\text{Fick}} \nabla x_k \tag{2.1}$$

where $J_i$ is the molar flux of component $i$, $c$ is the total molar concentration, $D_{ik}^{\text{Fick}}$ is the Fick's multicomponent diffusion coefficient for components $i$ and $k$, and $x_k$ is the mole fraction of component $k$. The diffusivity $D_{ik}^{\text{Fick}}$ is concentration dependent but independent of $\nabla x_k$. As a molar reference frame is used in Eq. (2.1), the fluxes are constraint by $\sum_{i=1}^{n} J_i = 0$. The Maxwell-Stefan theory is an alternative formulation which uses a gradient in chemical potential at constant temperature and pressure as driving force for mass transport [72, 73]. This driving force is balanced by friction forces between the species, which are proportional to differences in average molar velocities. The Maxwell-Stefan theory for a $n$-component system is given by [72, 88, 89, 91, 92]

$$-\frac{1}{RT} \nabla_{T,P} \mu_i = \sum_{j=1, j\neq i}^{n} \frac{x_j (u_i - u_j)}{Đ_{ij}} \tag{2.2}$$

in which $R$ is the universal gas constant, $T$ is the absolute temperature, $\nabla_{T,P}\mu_i$ is the chemical potential gradient of component $i$ at constant $T$,$P$ and $u_i$ and $u_j$ are the average velocities of the components $i$ and $j$, respectively. The Maxwell-Stefan diffusivity $Đ_{ij}$, can be considered as an inverse friction coefficient between components $i$ and $j$ and often depends less strongly on the concentration than Fick diffusivities [72].

On a macroscopic scale, Fick diffusivities are required, since they can be directly calculated from measurable quantities (*i.e.* concentrations) obtained from experiments. To describe diffusion in multicomponent systems, direct application of Fick's law is difficult as multicomponent Fick diffusivities are unrelated to their binary counterparts [72]. Maxwell-Stefan diffusivities can be computed directly from molecular simulations [74–76, 88–90, 94–98] and predictive models for $Đ_{ij}$ are available that work reasonably well for systems in which molecules do not strongly interact [89]. It is possible to relate both Fick's law and the Maxwell-Stefan theory, since they both describe the same diffusion process [72, 73, 76]. From Eqs. (2.1)

and (2.2) it can be derived that [72, 73, 76]

$$[D^{\text{Fick}}] = [B]^{-1}[\Gamma] \tag{2.3}$$

where $[D^{\text{Fick}}]$ is the $(n-1)\times(n-1)$ matrix of Fick diffusivities. Matrix $[B]$ is a square matrix of dimension $(n-1)\times(n-1)$ and its elements are given by [73, 76, 99]

$$B_{ii} = \frac{x_i}{Đ_{in}} + \sum_{j=1,j\neq i}^{n} \frac{x_j}{Đ_{ij}} \quad \text{with } i = 1, ..., (n-1) \tag{2.4}$$

$$B_{ij} = -x_i \left( \frac{1}{Đ_{ij}} - \frac{1}{Đ_{in}} \right) \quad \text{with } i,j = 1, ..., (n-1), i \neq j. \tag{2.5}$$

$[\Gamma]$ is the so-called matrix of thermodynamic factors in which the elements are defined as [72, 73, 76, 99]

$$\Gamma_{ij} = \delta_{ij} + x_i \left( \frac{\partial \ln \gamma_i}{\partial x_j} \right)_{T,P,\Sigma} \tag{2.6}$$

with $i \leq n$ and $j < n$. Although the matrix $[\Gamma]$ is a $(n-1)\times(n-1)$ matrix, we will see later that it is convenient to define $\Gamma_{ij}$ for $i \leq n$ and $j < n$. In Eq. (2.6), $\delta_{ij}$ is the Kronecker delta and $\gamma_i$ is the activity coefficient of component $i$ with $i, j < n$. The symbol $\Sigma$ is used to indicate that the differentiation is carried out while keeping the mole fractions of all components constant except the $n$-th, so that during the differentiation, $\sum_{i=1}^{n} x_i = 1$ [93]. The thermodynamic factor can be considered as a measure of the non-ideality of the mixture. For an ideal mixture, $\Gamma_{ij} = \delta_{ij}$.

The matrix $[\Gamma]$ can be obtained in two ways: (1) from experiments, and (2) from molecular simulations. The calculation of $[\Gamma]$ from experiments involves obtaining activity coefficients from vapor-liquid equilibrium data or by an equation of state, and in a next step evaluating $[\Gamma]$ from physical models for the excess Gibbs energy or by numerical differentiation of the activity coefficients. Since Maxwell-Stefan diffusivities can be calculated from molecular simulations, it is desirable to also compute $[\Gamma]$ from simulations [93] for the sake of consistency. Predicting $[\Gamma]$ from experiments often introduces large inaccuracies as there is only limited experimental data available for verification of the models [93, 100]. Model predictions for obtaining $[\Gamma]$ from vapor-liquid equilibrium data can differ up to 25% for certain systems [99]. Computing $[\Gamma]$ from simulations can be done in three ways: (1) from Kirkwood-Buff integrals [88, 101–104], (2) from activity coefficients obtained from conventional Widom test particle simulations or related methods, and (3) simulations in the grand-canonical ensemble. Calculation of $[\Gamma]$ from Kirkwood-Buff integrals involves the computation of the radial distribution function, $g(r)$ and its integration over volume [104]. This method has the advantage that insertions of particles (either as test particles or in the grand-canonical ensemble) are avoided as these are inefficient at high densities [53]. A major disadvantage is that the integral of the radial distribution function over volume only converges for large systems and a non-trivial interpretation of simulation results is needed in this case. Schnell *et al.* [102, 103] have presented a method for calculating the thermodynamic factor

using these Kirkwood-Buff integrals directly from equilibrium MD simulations for Lennard-Jones fluids. These authors sample concentration fluctuations inside small sub volumes inside a large simulation box and correct for finite size effects. Liu *et al.* [88, 101] have demonstrated the calculation of the thermodynamic factors for binary acetone-methanol and acetone-tetrachloromethane liquid mixtures and found excellent agreement when compared to the experimental values. Wedberg *et al.* [105, 106] and Christensen *et al.* [107, 108] have also calculated thermodynamic factors using the Kirkwood-Buff integrals, but used truncation and interpolation of the radial distribution function. Calculation of the thermodynamic factors from Kirkwood-Buff integrals involves the computation of the radial distribution function $g(r)$ and its integration over volume. The integral of $(g(r) - 1)$ over volume only converges for large systems in the thermodynamic limit and thus a non-trivial interpretation of simulation results is needed [91, 102–104]. The conventional Widom test particle insertion method is often used to obtain activity coefficients [109]. These activity coefficients can be fitted with a physical model for the excess Gibbs energy like Margules, van Laar, NRTL [93], or by numerical differentiation [109] to obtain $[\Gamma]$. The disadvantage of this method is that more than one simulation is required for the computation of $[\Gamma]$ and also numerical differentiation is less accurate. Our method of using a modified version of Widom test particle insertion method computes $[\Gamma]$ in a single simulation. This has the following advantages: (1) The problem of numerical differentiation is avoided and no physical model needs to be fitted to the simulation data; (2) Only minor modifications of the conventional Widom test particle method are needed. Therefore, $[\Gamma]$ can be calculated at virtually no extra computational cost at the same time when the activity coefficients are calculated.

Our method of calculating the thermodynamic factors directly follows from MC simulations without any numerical differentiation is presented below. We use a modified version of Widom Test Particle Insertion (WTPI) method using the simultaneous insertion of two test particles for the computation of $[\Gamma]$. Since conventional Widom two test particle insertions are not efficient, we introduce a new method called the Permuted Widom Test Particle Insertion (PWTPI) method. We derive a general expression for the thermodynamic factors for multicomponent systems and this is verified for a binary and ternary system. Our method is compared to the standard method of calculating thermodynamic factors which is numerically differentiating the activity coefficients computed from the conventional WTPI method. We find an excellent agreement between these approaches. The advantage of our approach is that, we can compute the thermodynamic factors for multicomponent systems directly from a single simulation. There is no need for an explicit numerical differentiation of activity coefficients to calculate thermodynamic factors. For the same computational cost required for calculating activity coefficients, all elements of the matrix $[\Gamma]$ can be calculated from the same simulation.

We apply the PWTPI method to validate the application of the newly derived Kirkwood-Buff theory for closed systems [85, 104] to ionic systems. For ionic systems consisting of monovalent fully dissociated ions (A and B) in a solvent (denoted by W), the constraints in the mole fractions of $x_{\mathrm{A}}$ and $x_{\mathrm{B}}$ introduce a singularity in the equations for calculating macroscopic properties, so whenever these constraints

simultaneously hold, the KB approach for closed systems cannot be used [110]. A way around the singularity is to consider the system as pseudo-binary and treat A and B as indistinguishable [111], but then one cannot obtain thermodynamic data for A and B individually. Krüger and co-workers [85, 104] have developed a new theory to treat the system mentioned earlier (W, A, B, with $x_A = x_B$) as a ternary one and to compute accurate ternary KB coefficients from MD simulations in the canonical ($NVT$) ensemble (*i.e.* a closed system), in sharp contrast to the fact that the traditional KB formalism only applies to infinitely large open systems. These authors derived the correct expressions for KB coefficients of open systems of volume $V$: [104]

$$\begin{aligned} G^V_{\alpha\beta} &\equiv \frac{1}{V}\int_V\int_V (g_{\alpha\beta}(r_{12})-1)\mathrm{d}\mathbf{r}_1\mathrm{d}\mathbf{r}_2 \\ &= 4\pi\int_0^{2R}(g_{\alpha\beta}(r)-1)r^2\left(1-\frac{3r}{4R}+\frac{r^3}{16R^3}\right)\mathrm{d}r \\ &\equiv G_{\alpha\beta}(R) \end{aligned} \tag{2.7}$$

where $R$ is the radius of a sphere with volume $V$, $\alpha,\beta$ are the component types, $N_\alpha$ is the number of molecules of component $\alpha$, $g_{\alpha\beta}(r_{12})$ is the pair correlation function for $\alpha,\beta$ pairs and $r_{12} = |\mathbf{r}_1 - \mathbf{r}_2|$. The thermodynamic factors $\Gamma_{ij}$ from KB coefficients can then be calculated [91, 112]. The PWTPI method can be as an independent check to compute the thermodynamic factors of ternary systems which are derived from chemical potentials and are not affected by the singularities in calculation of KB coefficients.

This chapter is organised as follows. In section 2.2, we derive expressions for the thermodynamic factors for multicomponent systems. In section 2.3, we discuss how to obtain these thermodynamic factors from MC simulation using the PWTPI method. Section 2.4 provides the details of the Monte Carlo simulations. Section 2.5 provides a comparison of our approach with the numerical differentiation method. Our findings are summarized in section 2.6.

## 2.2 Thermodynamic Factors for Multicomponent Systems

In an $n$-component system, we can express the activity coefficient $\gamma_i$ for component $i$ in terms of the chemical potential $\mu_i$ [109]:

$$\ln\gamma_i = \left(\frac{\mu_i - \mu_i^o}{k_\mathrm{B}T}\right) - \ln x_i \tag{2.8}$$

where $\mu_i^o$ is the chemical potential of the pure component. The chemical potential $\mu_i$ directly follows from the Gibbs energy:

$$\mu_i = \left(\frac{\partial G(N_1, N_2, ..., N_n, P, T)}{\partial N_i}\right)_{T,P,N_{j\neq i}} \tag{2.9}$$

in which $N_i$ is the number of molecules of component $i$, and $T$ and $P$ are the absolute temperature and pressure of the system. The Gibbs energy is related to the partition function $Q(N_1, N_2, ..., N_n, P, T)$ in the $NPT$ ensemble by

$$G(N_1, N_2, ..., N_n, P, T) = -k_{\mathrm{B}} T \ln Q(N_1, N_2, ..., N_n, P, T). \tag{2.10}$$

The chemical potential $\mu_i$ of component $i$ in principle follows from Widom's test particle insertion method [51, 53]

$$\begin{aligned} \mu_i &= -k_{\mathrm{B}} T \ln \frac{Q(N_1, N_2, ..., N_i + 1, ..., P, T)}{Q(N_1, N_2, ..., N_i, ..., P, T)} \\ &= -k_{\mathrm{B}} T \ln \left\langle \frac{V}{N+1} \exp[-\beta \Delta U] \right\rangle \end{aligned} \tag{2.11}$$

where $\langle \cdots \rangle$ denotes the ensemble average in the $NPT$ ensemble and $\Delta U^{+i}$ is the change in energy of the system when a single test particle of component $i$ is inserted in the system. It can be seen from Eq. (2.9) that $\mu_i$ is the first derivative of the Gibbs energy. Obtaining the elements of $[\Gamma]$ thus requires the second derivative of the Gibbs energy. This can be derived as follows. For $\Gamma_{ii}$ and $\Gamma_{ij}$, we have [83],

$$\Gamma_{ii} = 1 + x_i \left[ \frac{\partial \ln \gamma_i}{\partial x_i} \right]_{T,P,\Sigma} = x_i \left[ \frac{\partial \beta \mu_i}{\partial x_i} \right]_{T,P,\Sigma} \tag{2.12}$$

$$\Gamma_{ij} = x_i \left[ \frac{\partial \ln \gamma_i}{\partial x_j} \right]_{T,P,\Sigma} = x_i \left[ \frac{\partial \beta \mu_i}{\partial x_j} \right]_{T,P,\Sigma} \tag{2.13}$$

The differentiation is carried keeping the sum of the mole fractions constant. This can be expressed as

$$\left( \frac{\partial x_i}{\partial N_i} \right)_{\Sigma} = \frac{(N_1 + N_2 + ... + N_{i-1} + N_{i+1} + ... + N_n)}{(N_{\mathrm{total}})^2} - \frac{-N_i}{(N_{\mathrm{total}})^2} = \frac{1}{N_{\mathrm{total}}} \tag{2.14}$$

where $N_{\mathrm{total}}$ is the total number of particles in the system. Substituting Eqs. (2.14) and (2.9) into Eqs. (2.12), (2.13) yields

$$\begin{aligned} \Gamma_{ii} =& x_i \cdot N_{\mathrm{total}} \cdot \left( \left[ \frac{\partial^2 \beta G(N_i, N_j, ..., N_n, P, T)}{\partial N_i^2} \right]_{T,P,N_{j,j\neq i,n}} \right. \\ & \left. - \left[ \frac{\partial^2 \beta G(N_i, N_j, ..., N_n, P, T)}{\partial N_i \partial N_n} \right]_{T,P,N_{j,j\neq i,n}} \right) \end{aligned} \tag{2.15}$$

$$\begin{aligned} \Gamma_{ij} =& x_i \cdot N_{\mathrm{total}} \cdot \left( \left[ \frac{\partial^2 \beta G(N_i, N_j, ..., N_n, P, T)}{\partial N_i \partial N_j} \right]_{T,P,N_{j,j\neq i,n}} \right. \\ & \left. - \left[ \frac{\partial^2 \beta G(N_i, N_j, ..., N_n, P, T)}{\partial N_j \partial N_n} \right]_{T,P,N_{j,j\neq i,n}} \right) \end{aligned} \tag{2.16}$$

where $\beta = 1/(k_{\mathrm{B}}T)$ and $N_{\mathrm{total}}$ is the total number of molecules in the system. The Gibbs energy can be expressed as,

$$\begin{aligned} G(N_i, N_j, ..., N_n, P, T) =& G^{\mathrm{idealgas}}(N_i, N_j, ..., N_n, P, T) \\ &+ [G(N_i, N_j, ..., N_n, P, T) \\ &- G^{\mathrm{idealgas}}(N_i, N_j, ..., N_n, P, T)] \end{aligned} \tag{2.17}$$

in which $G^{\mathrm{idealgas}}$ is the Gibbs energy of the system if it would be an ideal gas mixture. The first term $G^{\mathrm{idealgas}}(N_i, N_j, ..., N_n, P, T)$ from Eq. (2.17) results in a contribution of the ideal gas term ($\delta_{ij}$) to the thermodynamic factor $\Gamma_{ij}$. For the term $G - G^{\mathrm{idealgas}}(N_i, N_j, ..., N_n, P, T)$, we use the partition function from Eq. (2.10) and use a numerical differentiation scheme to carry out the differentiation of Eq. (2.15). When the second derivative of the Gibbs free energy without the ideal gas term is evaluated, the contribution of the ideal gas term is ignored and this introduces finite size effects. The approach of Eq. (2.17) takes into account the contribution of the ideal gas term and eliminates finite size effects. The central assumption is that the second order derivative can be approximated by a forward differencing scheme [113]. Using the right hand side of Eq. (2.17) leads to

$$\begin{aligned} \left(\frac{\partial^2 G(N_i, N_j, ..., N_n, P, T)}{\partial N_i^2}\right)_{T,P,N_{j,j\neq i,n}} \approx& \frac{1}{\beta N_i} + [G(N_i + 2, N_j, ..., N_n, P, T) \\ &- 2G(N_i + 1, N_j, ..., N_n, P, T) \\ &+ G(N_i, N_j, ..., N_n, P, T)] - \\ &[G^{\mathrm{idealgas}}(N_i + 2, N_j, ..., N_n, P, T) \\ &- 2G^{\mathrm{idealgas}}(N_i + 1, N_j, ..., N_n, P, T) \\ &+ G^{\mathrm{idealgas}}(N_i, N_j, ..., N_n, P, T)] \end{aligned} \tag{2.18}$$

$$\begin{aligned} \left(\frac{\partial^2 G(N_i, N_j, ..., N_n, P, T)}{\partial N_i \partial N_n}\right)_{T,P,N_{j,j\neq i,n}} \approx& [G(N_i + 1, N_j, ..., N_n + 1, P, T) \\ &- G(N_i + 1, N_j, ..., N_n, P, T) \\ &- G(N_i, N_j, ..., N_n + 1, P, T) \\ &+ G(N_i, N_j, ..., N_n, P, T)] \\ &- \big[G^{\mathrm{idealgas}}(N_i + 1, N_j, ..., N_n + 1, P, T) \\ &- G^{\mathrm{idealgas}}(N_i + 1, N_j, ..., N_n, P, T) \\ &- G^{\mathrm{idealgas}}(N_i, N_j, ..., N_n + 1, P, T) \\ &+ G^{\mathrm{idealgas}}(N_i, N_j, ..., N_n, P, T)\big] . \end{aligned} \tag{2.19}$$

Applying the forward difference method from Eqs. (2.18) and (2.19) and substituting the expression for Gibbs energy from Eq. (2.10) in Eq. (2.15), we finally obtain,

$$
\begin{aligned}
\Gamma_{ii} \approx \delta_{ii} - x_i \cdot N_{\text{total}} \cdot [\{&(\ln Q(N_i+2, N_j, ..., N_n, P, T) \\
&- \ln Q(N_i+1, N_j, ..., N_n, P, T)) - (\ln Q(N_i+1, N_j, ..., N_n, P, T) \\
&- \ln Q(N_i, N_j, ..., N_n, P, T))\} \\
&- \{(\ln Q(N_i+1, N_j, ..., N_n+1, P, T) - \ln Q(N_i, N_j, ..., N_n+1, P, T)) \\
&- (\ln Q(N_i+1, N_j, ..., N_n, P, T) - \ln Q(N_i, N_j, ..., N_n, P, T))\}] \\
+ x_i \cdot N_{\text{total}} \cdot [\{&(\ln Q^{\text{idealgas}}(N_i+2, N_j, ..., N_n, P, T) \\
&- \ln Q^{\text{idealgas}}(N_i+1, N_j, ..., N_n, P, T)) \\
&- (\ln Q^{\text{idealgas}}(N_i+1, N_j, ..., N_n, P, T) \\
&- \ln Q^{\text{idealgas}}(N_i, N_j, ..., N_n, P, T))\} \\
&- \{(\ln Q^{\text{idealgas}}(N_i+1, N_j, ..., N_n+1, P, T) \\
&- \ln Q^{\text{idealgas}}(N_i, N_j, ..., N_n+1, P, T)) \\
&- (\ln Q^{\text{idealgas}}(N_i+1, N_j, ..., N_n, P, T) \\
&- \ln Q^{\text{idealgas}}(N_i, N_j, ..., N_n, P, T))\}] \qquad (2.20) \\
= 1 - x_i \cdot N_{\text{total}} \cdot &\left[\ln \left\langle \frac{V^2}{(N_i+1)(N_i+2)} \exp(-\beta \Delta U^{+ii}) \right\rangle \right. \\
&- \ln \left\langle \frac{V}{N_i+1} \exp(-\beta \Delta U^{+i}) \right\rangle \\
&- \ln \left\langle \frac{V^2}{(N_i+1)(N_n+1)} \exp(-\beta \Delta U^{+in}) \right\rangle \\
&\left. + \ln \left\langle \frac{V}{N_n+1} \exp(-\beta \Delta U^{+n}) \right\rangle \right] \\
+ x_i \cdot N_{\text{total}} \cdot &\left[\ln \left\langle \frac{V^2}{(N_i+1)(N_i+2)} \right\rangle - \ln \left\langle \frac{V}{N_i+1} \right\rangle \right. \\
&\left. - \ln \left\langle \frac{V^2}{(N_i+1)(N_n+1)} \right\rangle + \ln \left\langle \frac{V}{N_n+1} \right\rangle \right]. \qquad (2.21)
\end{aligned}
$$

$\langle \cdots \rangle$ represents an ensemble average in the $NPT$ ensemble (where $N_i, N_j, ..., N_n, P, T$ are constant) as well as an average over all possible positions of the test particles. The notation $\Delta U^{+i}$ refers to the change in energy of the system when a single test particle of component $i$ is inserted at a random position [53]. The notation $\Delta U^{+ij}$ refers to the change in energy of the system when test particles of type $i$ and $j$ are inserted simultaneously. When one test particle of type $i$ and one test particle of type $j$ are inserted simultaneously, the interaction energy between these particles is included in $\Delta U^{+ij}$. The accuracy of calculating [$\Gamma$] not only depends on finding reasonable positions for inserting two test particles simultaneously according to the Permuted Widom test-particle insertion method, but also depends on the error due to the forward difference method (Eqs. (2.18) and (2.19)). The relative error in our

case is $(1/N_i)$ so the convergence to the correct value of $[\Gamma]$ will scale as $(1/N_i)$ [113]. The derivation of $\Gamma_{ij,j\neq i}$ follows in an analogous way from the derivation of $\Gamma_{ii}$ resulting in,

$$\begin{aligned}
\Gamma_{ij,j\neq i} \approx & -x_i \cdot N_{\text{total}} \cdot [\{(\ln Q(N_i+1, N_j+1, ..., N_n, P, T) \\
& - \ln Q(N_i+1, N_j, ..., N_n, P, T)) - (\ln Q(N_i, N_j+1, ..., N_n, P, T) \\
& - \ln Q(N_i, N_j, ..., N_n, P, T))\} \\
& - \{(\ln Q(N_i+1, N_j, ..., N_n+1, P, T) - \ln Q(N_i, N_j, ..., N_n+1, P, T)) \\
& - (\ln Q(N_i+1, N_j, ..., N_n, P, T) - \ln Q(N_i, N_j, ..., N_n, P, T))\}] \\
& + x_i \cdot N_{\text{total}} \cdot [\{(\ln Q^{\text{idealgas}}(N_i+, N_j+1, ..., N_n, P, T) \\
& - \ln Q^{\text{idealgas}}(N_i+1, N_j, ..., N_n, P, T)) \\
& - (\ln Q^{\text{idealgas}}(N_i, N_j+1, ..., N_n, P, T) \\
& - \ln Q^{\text{idealgas}}(N_i, N_j, ..., N_n, P, T))\} \\
& - \{(\ln Q^{\text{idealgas}}(N_i+1, N_j, ..., N_n+1, P, T) \\
& - \ln Q^{\text{idealgas}}(N_i, N_j, ..., N_n+1, P, T)) \\
& - (\ln Q^{\text{idealgas}}(N_i+1, N_j, ..., N_n, P, T) \\
& - \ln Q^{\text{idealgas}}(N_i, N_j, ..., N_n, P, T))\}] \qquad (2.22)
\end{aligned}$$

$$\begin{aligned}
= & -x_i \cdot N_{\text{total}} \cdot \left[ \ln \left\langle \frac{V^2}{(N_i+1)(N_j+1)} \exp(-\beta \Delta U^{+ij}) \right\rangle \right. \\
& - \ln \left\langle \frac{V}{N_j+1} \exp(-\beta \Delta U^{+j}) \right\rangle \\
& - \ln \left\langle \frac{V^2}{(N_i+1)(N_n+1)} \exp(-\beta \Delta U^{+in}) \right\rangle \\
& \left. + \ln \left\langle \frac{V}{N_n+1} \exp(-\beta \Delta U^{+n}) \right\rangle \right] \\
& + x_i \cdot N_{\text{total}} \cdot \left[ \ln \left\langle \frac{V^2}{(N_i+1)(N_j+1)} \right\rangle - \ln \left\langle \frac{V}{N_j+1} \right\rangle \right. \\
& \left. - \ln \left\langle \frac{V^2}{(N_i+1)(N_n+1)} \right\rangle + \ln \left\langle \frac{V}{N_n+1} \right\rangle \right]. \qquad (2.23)
\end{aligned}$$

We can derive the different matrices of thermodynamic factors for the multicomponent system from these set of equations. If we substitute $n = 2$ for a binary system in Eq. (2.21), we obtain the expression for the thermodynamic factor:

$$\begin{aligned}\Gamma = 1 - x_1 \cdot N_{\text{total}} \cdot \Bigg[ & \ln \left\langle \frac{V^2}{(N_1+1)(N_1+2)} \exp(-\beta \Delta U^{+11}) \right\rangle \\ & - \ln \left\langle \frac{V}{N_1+1} \exp(-\beta \Delta U^{+1}) \right\rangle \\ & - \ln \left\langle \frac{V^2}{(N_1+1)(N_2+1)} \exp(-\beta \Delta U^{+12}) \right\rangle \\ & + \ln \left\langle \frac{V}{N_2+1} \exp(-\beta \Delta U^{+2}) \right\rangle \Bigg] \\ + x_1 \cdot N_{\text{total}} \cdot \Bigg[ & \ln \left\langle \frac{V^2}{(N_1+1)(N_1+2)} \right\rangle - \ln \left\langle \frac{V}{N_1+1} \right\rangle \\ & - \ln \left\langle \frac{V^2}{(N_1+1)(N_2+1)} \right\rangle + \ln \left\langle \frac{V}{N_2+1} \right\rangle \Bigg] . \end{aligned} \tag{2.24}$$

The elements of the matrix of thermodynamic factors [Γ] for a ternary system are,

$$\begin{aligned}\Gamma_{11} = 1 - x_1 \cdot N_{\text{total}} \cdot \Bigg[ & \ln \left\langle \frac{V^2}{(N_1+1)(N_1+2)} \exp(-\beta \Delta U^{+11}) \right\rangle \\ & - \ln \left\langle \frac{V}{N_1+1} \exp(-\beta \Delta U^{+1}) \right\rangle \\ & - \ln \left\langle \frac{V^2}{(N_1+1)(N_3+1)} \exp(-\beta \Delta U^{+13}) \right\rangle \\ & + \ln \left\langle \frac{V}{N_3+1} \exp(-\beta \Delta U^{+3}) \right\rangle \Bigg] \\ + x_1 \cdot N_{\text{total}} \cdot \Bigg[ & \ln \left\langle \frac{V^2}{(N_1+1)(N_1+2)} \right\rangle - \ln \left\langle \frac{V}{N_1+1} \right\rangle \\ & - \ln \left\langle \frac{V^2}{(N_1+1)(N_3+1)} \right\rangle + \ln \left\langle \frac{V}{N_3+1} \right\rangle \Bigg] \end{aligned} \tag{2.25}$$

$$\begin{aligned}\Gamma_{12} = -x_1 \cdot N_{\text{total}} \cdot \Bigg[ & \ln \left\langle \frac{V^2}{(N_1+1)(N_2+1)} \exp(-\beta \Delta U^{+12}) \right\rangle \\ & - \ln \left\langle \frac{V}{N_2+1} \exp(-\beta \Delta U^{+2}) \right\rangle \\ & - \ln \left\langle \frac{V^2}{(N_1+1)(N_3+1)} \exp(-\beta \Delta U^{+13}) \right\rangle \\ & + \ln \left\langle \frac{V}{N_3+1} \exp(-\beta \Delta U^{+3}) \right\rangle \Bigg] \\ + x_1 \cdot N_{\text{total}} \cdot \Bigg[ & \ln \left\langle \frac{V^2}{(N_1+1)(N_2+1)} \right\rangle - \ln \left\langle \frac{V}{N_2+1} \right\rangle \\ & - \ln \left\langle \frac{V^2}{(N_1+1)(N_3+1)} \right\rangle + \ln \left\langle \frac{V}{N_3+1} \right\rangle \Bigg] \end{aligned} \tag{2.26}$$

$$\begin{aligned}\Gamma_{21} = -x_2 \cdot N_{\text{total}} \cdot \Bigg[ & \ln \left\langle \frac{V^2}{(N_1+1)(N_2+1)} \exp(-\beta \Delta U^{+12}) \right\rangle \\ & - \ln \left\langle \frac{V}{N_1+1} \exp(-\beta \Delta U^{+1}) \right\rangle \\ & - \ln \left\langle \frac{V^2}{(N_2+1)(N_3+1)} \exp(-\beta \Delta U^{+23}) \right\rangle \\ & + \ln \left\langle \frac{V}{N_3+1} \exp(-\beta \Delta U^{+3}) \right\rangle \Bigg] \\ + x_2 \cdot N_{\text{total}} \cdot \Bigg[ & \ln \left\langle \frac{V^2}{(N_1+1)(N_2+1)} \right\rangle - \ln \left\langle \frac{V}{N_1+1} \right\rangle \\ & - \ln \left\langle \frac{V^2}{(N_2+1)(N_3+1)} \right\rangle + \ln \left\langle \frac{V}{N_3+1} \right\rangle \Bigg] \end{aligned} \tag{2.27}$$

$$\begin{aligned}\Gamma_{22} = 1 - x_2 \cdot N_{\text{total}} \cdot \Bigg[ & \ln \left\langle \frac{V^2}{(N_2+1)(N_2+2)} \exp(-\beta \Delta U^{+22}) \right\rangle \\ & - \ln \left\langle \frac{V}{N_2+1} \exp(-\beta \Delta U^{+2}) \right\rangle \\ & - \ln \left\langle \frac{V^2}{(N_2+1)(N_3+1)} \exp(-\beta \Delta U^{+23}) \right\rangle \\ & + \ln \left\langle \frac{V}{N_3+1} \exp(-\beta \Delta U^{+3}) \right\rangle \Bigg] \\ + x_2 \cdot N_{\text{total}} \cdot \Bigg[ & \ln \left\langle \frac{V^2}{(N_2+1)(N_2+2)} \right\rangle - \ln \left\langle \frac{V}{N_2+1} \right\rangle \\ & - \ln \left\langle \frac{V^2}{(N_2+1)(N_3+1)} \right\rangle + \ln \left\langle \frac{V}{N_3+1} \right\rangle \Bigg] \end{aligned} \tag{2.28}$$

It is helpful to use the Gibbs-Duhem equation in the calculation of the elements of [Γ]. At constant temperature and pressure, the general expression for the Gibbs-Duhem equation is

$$\sum_{i=1}^{n} N_i \mathrm{d}\mu_i = 0 \tag{2.29}$$

For a binary system, the Gibbs-Duhem equation reduces to

$$x_1 \left[ \frac{\partial \ln \gamma_1}{\partial x_1} \right]_{p,T} = x_2 \left[ \frac{\partial \ln \gamma_2}{\partial x_2} \right]_{p,T} \tag{2.30}$$

Applying the Gibbs-Duhem equation (Eq. (2.30)) for a binary system, we obtain an expression equivalent to Eq. (2.24),

$$\begin{aligned}\Gamma = 1 - x_2 \cdot N_{\text{total}} \cdot \Bigg[ & \ln \left\langle \frac{V^2}{(N_2+1)(N_2+2)} \exp(-\beta \Delta U^{+22}) \right\rangle \\ & - \ln \left\langle \frac{V}{N_2+1} \exp(-\beta \Delta U^{+2}) \right\rangle \\ & - \ln \left\langle \frac{V^2}{(N_1+1)(N_2+1)} \exp(-\beta \Delta U^{+12}) \right\rangle \\ & + \ln \left\langle \frac{V}{N_1+1} \exp(-\beta \Delta U^{+1}) \right\rangle \Bigg] \\ + x_1 \cdot N_{\text{total}} \cdot \Bigg[ & \ln \left\langle \frac{V^2}{(N_2+1)(N_2+2)} \right\rangle - \ln \left\langle \frac{V}{N_2+1} \right\rangle \\ & - \ln \left\langle \frac{V^2}{(N_1+1)(N_2+1)} \right\rangle + \ln \left\langle \frac{V}{N_1+1} \right\rangle \Bigg]. \end{aligned} \tag{2.31}$$

It is clear that $\Gamma$ calculated from both Eqs. (2.24) and (2.31) must converge to the same value for $\Gamma$. Eqs. (2.24) and (2.31) can be written as $-N_{\text{total}} x_1 A$ and $-N_{\text{total}} x_2 B$ respectively, where $A$ and $B$ are the sum of the logarithms of the different ensemble averages. Since Eqs. (2.24) and (2.31) should provide the same result, the magnitude of the terms $A$ and $B$ depend on the composition. $\langle \Gamma \rangle$ is defined as the weighted mean of the individual $\Gamma$ calculated from Eqs. (2.24) and (2.31) to significantly improve the statistics, avoid propagation of the relative error in $A$ and $B$ and to arrive at the converged value faster. The weights are the mole fractions of the components. $\langle \Gamma \rangle$ is defined as

$$\langle \Gamma \rangle = x_2 \Gamma_{\text{Eq.(2.24)}} + x_1 \Gamma_{\text{Eq.(2.31)}} \tag{2.32}$$

For a ternary system, the Gibbs-Duhem equation can be expressed as,

$$x_1 \left[ \frac{\partial \ln \gamma_1 x_1}{\partial x_1} \right]_{T,P,\Sigma} + x_2 \left[ \frac{\partial \ln \gamma_2 x_2}{\partial x_1} \right]_{T,P,\Sigma} + x_3 \left[ \frac{\partial \ln \gamma_3 x_3}{\partial x_1} \right]_{T,P,\Sigma} = 0 \tag{2.33}$$

$$x_1 \left[ \frac{\partial \ln \gamma_1 x_1}{\partial x_2} \right]_{T,P,\Sigma} + x_2 \left[ \frac{\partial \ln \gamma_2 x_2}{\partial x_2} \right]_{T,P,\Sigma} + x_3 \left[ \frac{\partial \ln \gamma_3 x_3}{\partial x_2} \right]_{T,P,\Sigma} = 0 \tag{2.34}$$

resulting in,

$$\Gamma_{11} = 1 - \Gamma_{21} - \Gamma_{31} \tag{2.35}$$

$$\Gamma_{12} = 1 - \Gamma_{22} - \Gamma_{32} \tag{2.36}$$

with $\Gamma_{ij}$ defined according to Eq. (2.6). As explained for the binary system, the statistics of our calculation are significantly improved if the term $\Gamma_{ij}$ has a weight factor $x_i$ and the equivalent term from the Gibbs-Duhem equation a weight factor $(1 - x_i)$. Thus we define the term $\langle \Gamma_{ij} \rangle$ to obtain the converged value for $\Gamma_{ij}$

computed Eqs. (2.25)-(2.28) and by using the Gibbs-Duhem equations (substituting values of Eqs. (2.25)-(2.28) in Eqs. (2.35)-(2.36)). For a ternary system, the thermodynamic factors $\langle\Gamma\rangle$ then become

$$\langle\Gamma_{11}\rangle = x_1\Gamma_{11} + (x_2 + x_3)(1 - \Gamma_{21} - \Gamma_{31}) \tag{2.37}$$
$$\langle\Gamma_{12}\rangle = x_1\Gamma_{12} + (x_2 + x_3)(1 - \Gamma_{22} - \Gamma_{32}) \tag{2.38}$$
$$\langle\Gamma_{21}\rangle = x_2\Gamma_{21} + (x_1 + x_3)(1 - \Gamma_{11} - \Gamma_{31}) \tag{2.39}$$
$$\langle\Gamma_{22}\rangle = x_2\Gamma_{22} + (x_1 + x_3)(1 - \Gamma_{12} - \Gamma_{32}) \tag{2.40}$$

with all the elements of $\Gamma$ on the right hand side of the equation computed using Eqs. (2.25)-(2.28).

## 2.3 Permuted Widom Particle Insertion Method

For multicomponent systems, $\Gamma$ is calculated by carrying out Widom Test Particle Insertion (WTPI) method from simulations in the *NPT* ensemble (Eqs. (2.37)-(2.40)). Four different kinds of test particle insertions are performed:

1. Insertion of two test particles of component $i$ keeping the number of particles of component $j$ constant, thereby obtaining $< \exp(\Delta U^{+ii}) >$

2. Insertion of one test particle of component $i$ and one test particle of component $j$ simultaneously, thereby obtaining $< \exp(\Delta U^{+ij}) >$

3. Insertion of a single test particle of component $i$ keeping the number of particles of component $j$ constant, thereby obtaining $< \exp(\Delta U^{+i}) >$ which is the conventional WTPI method

4. Insertion of a single test particle of component $j$ keeping the number of particles of component $i$ constant, thereby obtaining $< \exp(\Delta U^{+j}) >$ which is the conventional WTPI method

Therefore, only a single simulation is needed to calculate $[\Gamma]$ from Eqs. (2.37)-(2.40).

Accurate calculation of thermodynamic factors depends on the probability of finding reasonable positions for the test particle(s) to be inserted. Reasonable positions are those which do not overlap with any existing particles (overlap of the positions causes the terms $\exp(\Delta U^{+i})$ or $\exp(\Delta U^{+ij})$ to be zero). The probability of finding reasonable positions for the two-test particle insertions in dense systems is very low. This is because, in a dense system, the number of positions that can be generated without overlap is less. To solve this issue, we have developed a new method called the "Permuted Widom Test Particle Insertion (PWTPI)" method. This method uses combinatorics to increase the probability of finding reasonable positions for the test particle insertions. We pre-generate a list of random trial positions before every insertion of two Widom test particles. The change in energy of inserting one test particle for each of the pre-generated positions ($\Delta U^{+i}$) is calculated and stored in memory. This is essentially the conventional Widom single test particle insertion method. For performing the Widom two-test particle insertion,

we insert the two test particles in all possible combinations of the pair of the pre-generated positions. To calculate the change in energy of the system for the two test particle insertion, we only need to calculate the mutual interaction energies of the two test particles. This significantly decreases the time for the actual computation of the change in energies as the change in energies of a two particle insertion for each position is not calculated every time.

The conventional Widom two-test particle insertion method essentially corresponds to calculating the average of a function $f(r_1, r_2)$, where $f(r_1, r_2)$ can be written as: $f(r_1, r_2) = g(r_1) + h(r_2) + k(r_1, r_2)$ in which the functions $g$ and $h$ are computationally expensive, but the function $k$ is not. The functions $g$ and $h$ denote interactions of the test particles with the medium, while $k$ denotes the interactions between the test particles themselves. The PWTPI method essentially pre-calculates the functions $g$ and $h$ for all the combinations of the pairs of pre-generated trial positions and only computes the function $k$ every time the two test particles are considered for different combination of the trial positions.

The algorithm for the insertion of two types of particles $i$ and $j$ is stated below.

1. Generate $N_{\text{trial}}$ random positions $(r_{k\in\{1,2,\ldots,N_{\text{trial}}\}})$
2. For each molecule type $i$ at position $r_k$, compute and store the value of $\exp(-\beta\Delta U^{+i}(r_k))$ which is used for the calculation of the activity coefficients (Eq. (2.8)).
3. For all pairs of positions $r_k$, $r_m$ $(k > m)$, compute $\exp(-\beta\Delta U^{+ij}(r_k, r_m))$ for particles of type $i$ and $j$. Here, only the interactions between the test particles need to be computed, so this computation is fast. The value of $\exp(-\beta\Delta U^{+ij}(r_k, r_m))$ follows from:

$$\exp(-\beta\Delta U^{+ij}(r_k, r_m)) = \exp(-\beta\Delta U^{+i}(r_k)) \cdot \exp(-\beta\Delta U^{+j}(r_m)) \times \exp(-\beta\varphi(r_k, r_m)), \tag{2.41}$$

   where $\varphi(r_k, r_m)$ is the interaction energy between particles at positions $r_k$ and $r_m$. The factors $\exp(-\beta\Delta U^{+i}(r_k))$ and $\exp(-\beta\Delta U^{+j}(r_m))$ have already been computed in step 2.

The number of pre-generated trial positions ($N_{\text{trial}}$) in the Permuted Widom test particle insertion algorithm is the demanding factor for the efficiency of the algorithm. If $N_{\text{trial}}$ is small, the algorithm essentially reduces to the conventional Widom two test particle method, which is inefficient as explained earlier. If $N_{\text{trial}}$ is large, there is an increase in the computational time but no additional gain in accuracy as many combinations of trial positions will provide essentially the same information for the current configuration of the system. To explain the gain in efficiency, in the thermodynamic limit we define a factor $p$, which is defined as the probability of finding a reasonable (*i.e.* a non-zero Boltzmann factor) position for the insertion of a single Widom test particle. For a conventional Widom two test particle insertion, the number of reasonable positions resulting from $N_{\text{trial}}$ random positions is $N_{\text{trial}} \cdot p^2$. In the Permuted Widom test particle, the number of reasonable positions resulting from $N_{\text{trial}}$ random positions for the two test particles insertion is

Table 2.1: The different Lennard-Jones parameters $\sigma_{ij}$ and $\epsilon_{ij}$ for the ternary mixture in reduced units.

| Lennard-Jones Interaction Parameters: $\sigma_{ij}$ | | | |
|---|---|---|---|
| $j/i$ | 1 | 2 | 3 |
| 1 | 1.0 | 1.1 | 1.05 |
| 2 | 1.1 | 1.2 | 1.15 |
| 3 | 1.05 | 1.15 | 1.1 |

| Lennard-Jones Interaction Parameters: $\epsilon_{ij}$ | | | |
|---|---|---|---|
| $j/i$ | 1 | 2 | 3 |
| 1 | 1.0 | 0.5 | 0.3 |
| 2 | 0.1 | 0.5 | 0.2 |
| 3 | 0.3 | 0.2 | 0.75 |

$(\frac{1}{2} \cdot N_{\text{trial}}^2 \cdot p^2)$. The factor $(\frac{1}{2} \cdot N_{\text{trial}}^2)$ arises from the fact that we insert the particles in different permutations of pre-generated positions and store this information. The PWTPI method is thus a factor $(\frac{1}{2} \cdot N_{\text{trial}})$ more efficient than the conventional WTPI for insertion of two test particles.

## 2.4 Monte Carlo Simulations

A binary system consisting of Lennard-Jones particles was studied [51, 53]. Reduced units are used in the remainder of this chapter [51, 53]. The two Lennard-Jones particles have different interaction parameters: $\sigma_1 = 1.0$, $\sigma_2 = 1.2$, $\epsilon_{11} = 1.0$ and $\epsilon_{22} = 0.5$. $\epsilon_{12} = \epsilon_{21} = 0.1$. A ternary system consisting of Lennard-Jones (LJ) particles was also studied. The different interaction parameters for the ternary system are tabulated in Table 2.1. Monte Carlo simulations in the $NPT$ ensemble were used to calculate the different thermodynamic factors for both binary and ternary systems. Periodic boundary conditions were applied to the simulation box. The LJ potential is shifted and truncated at $2.5\sigma_1$. The reduced temperature and reduced pressure for all systems were set at $T = 2.0$ and $P = 2.8$ respectively resulting in overall number densities of around 0.5. For the MC simulations, 99% of the trial moves were translation moves and 1% of the trial moves were volume change moves. The minimum displacements and volume changes were set such that the acceptance of the translation and the volume change moves were roughly 50%.

The simulations for the binary system were performed for different mole fractions ranging from $x_1 = 0.05$ to $x_1 = 0.95$ for $N_{\text{trial}} = 500$ and different number of particles in the system, $N_{\text{total}} = 100, 200, 400$. The thermodynamic factor was calculated using the PWTPI method from Eq. (2.32). The value of $N_{\text{trial}}$ (different number of trial positions) was set to 500. For ternary systems, the thermodynamic factor was calculated using the PWTPI method from Eqs. (2.25)-(2.28) and Eqs. (2.37)-(2.40). Chemical potentials were also computed using conventional WTPI

method to calculate the activity coefficients using Eq. (2.8). The value of $\mu_i^o$ follows by setting the reference state, *i.e.* $\lim_{x_i \to 1} \gamma_i(x_i) = 1$. The CPU time required to compute $\Gamma_{ij}$ ranged from 2 weeks to 3 weeks using state-of-the-art computation facilities.



To demonstrate that one indeed can compute thermodynamic factors $\Gamma_{ij}$ from KB theory, we simulated a ternary system (W, A, B) of particles interacting with WCA [114] potentials with $x_A = x_B$. The WCA potential is a soft-repulsive potential consisting of a shifted Lennard-Jones potential with the attractive tail cut off. As the KB theory is formulated regardless of the type of interactions between components, this system can be considered as a simple model for a salt solution with solvent W (albeit with significantly reduced interaction ranges). Reduced units are used in all cases for this system. All particles have the same diameter, $\sigma$, but the energy parameters $\epsilon$ are different: $\epsilon_{WW} = \epsilon_{AA} = \epsilon_{BB} = 1$, $\epsilon_{AW} = 4/10$, $\epsilon_{BW} = 2/10$, and $\epsilon_{AB} = 5/10$.

## 2.5 Results and Discussion

Fig. 2.1 shows the values of $\Gamma$ calculated from Eqs. (2.24) and (2.31) and the average $\Gamma$ calculated from Eq. (2.32) for a binary Lennard-Jones mixture of 400 particles with $T = 2.0$, $P = 2.8$ and $x_1 = 0.5$. We verified that, for much longer simulations, $\Gamma$ calculated from Eqs. (2.24) and (2.31) will converge to $\Gamma_{avg}$. Clearly, the convergence of $\Gamma_{avg}$ (Eq. (2.32)) is much faster due to the reasons described in section 2.2.

From section 2.3, it is expected that the PWTPI method leads to better statistics than the conventional Widom two test particle insertion method. Fig. 2.2 compares the $\Gamma$ obtained from different $N_{trial}$ for $N_{total} = 400$. We can observe from Fig. 2.2 that as the number of pre-generated trial positions, $N_{trial}$, increases, $\Gamma$ converges faster for the same number of MC steps. The conventional Widom two-test particle insertion method is when $N_{trial} = 2$ and this is very inefficient. It can already be observed that sufficiently accurate results are obtained for $N_{trial} = 1000$.

To test Eq. (2.32) for $\langle\Gamma\rangle$, molecular simulations were performed for binary systems for different numbers of particles, $N_{total} = 100, 200$ and 400 for $N_{trial} = 500$, $T = 2.0$, $P = 2.8$. The conventional WTPI method was used to compute the activity coefficients which were then fitted to the NRTL model to obtain $\Gamma$. This was compared to $\langle\Gamma\rangle$ calculated from Eq. (2.32). From Fig. 2.3, it can be observed that our results agree excellently with the prediction of $\Gamma$ from NRTL model. The value of $\Gamma$ obtained from the fitting of activity coefficients to the NRTL model show deviations for different number of particles for a given mole fraction. This is due to the finite size effect for $\gamma$, which apparently are stronger than that for $\langle\Gamma\rangle$. Since we incorporate the term $G^{idealgas}$ in the Gibbs free energy (Eq. (2.10)) leads to Eq. (2.17). Eq. (2.17) is then substituted instead of Eq. (2.10) when evaluating the second derivative using the first-order forward difference scheme to obtain the new expression for $\Gamma$ (Eq. (2.24)). Eq. (2.24) takes into account the contribution of the ideal gas term and thus suffers less from finite size effects.

Fig. 2.4 shows the values of $\Gamma_{11}$ calculated from Eq. (2.25), Eqs. (2.27)+(2.35)

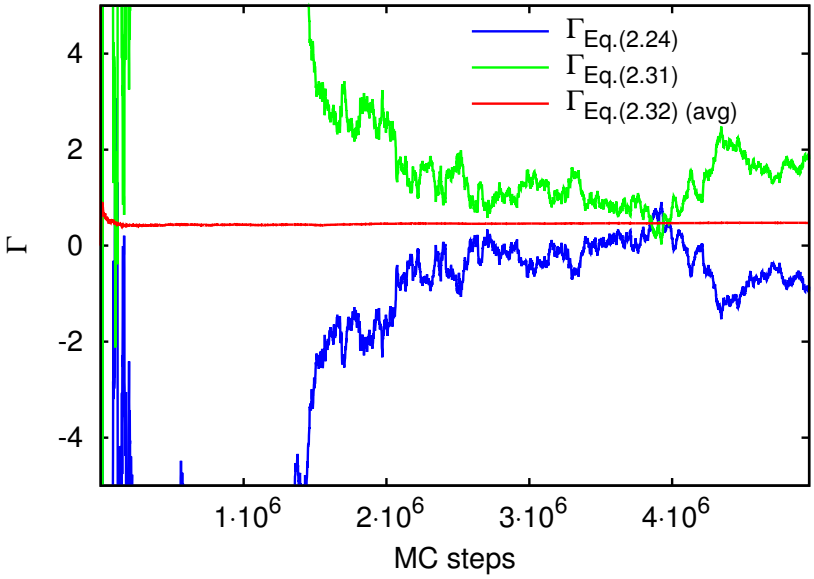


Figure 2.1: Average thermodynamic factor $\Gamma$ calculated from Eqs. (2.24), (2.31) and (2.32) for a binary Lennard-Jones system as a function of the number of trial moves for $x_1 = 0.5$, $N_{\text{total}} = 400$, $N_{\text{trial}} = 2000$, $T = 2.0$ and $P = 2.8$.

and $\langle\Gamma_{11}\rangle$ calculated from Eq. (2.37) for a ternary Lennard-Jones mixture of 100 particles with $T = 2.0$, $P = 2.8$, $x_1 = 0.25$, $x_2 = 0.25$ and $x_3 = 0.5$. It can be observed from Fig. 2.4 that the value of $\langle\Gamma_{11}\rangle$ computed from Eq. (2.37) converges to the result much faster than $\Gamma_{11}$ calculated from Eqs. (2.25) or (2.35). We verified that for longer simulations, $\Gamma_{11}$ calculated from Eqs. (2.25) and (2.35) converge to exactly the same value of $\langle\Gamma_{11}\rangle$ calculated from Eq. (2.37).

Fig. 2.5 compares the elements of $[\Gamma]$ obtained from numerically differentiating the activity coefficients obtained from the conventional WTPI method with our simulation results for $x_1 = 0.3, x_2 = 0.3, x_3 = 0.4$ for different total number of particles of the system, $N_{\text{total}} = 100, 200$. $\langle\Gamma_{11}\rangle$, $\langle\Gamma_{12}\rangle$, $\langle\Gamma_{21}\rangle$ and $\langle\Gamma_{22}\rangle$ (Eqs. (2.37)-(2.40)) are computed from simulation using the PWTPI method. The elements of $[\Gamma]$ are obtained from direct numerical differentiation by using a central difference method. The chemical potentials $\mu_1$, $\mu_2$, $\mu_3$ obtained from the conventional WTPI method were used to calculate the activity coefficients $\gamma_i$ and these are numerically differentiated to provide the elements of $[\Gamma]$ using the expression:

$$\Gamma_{ij} \approx \delta_{ij} + x_i \left[ \frac{\ln\left(\frac{\gamma_i(x_j')}{\gamma_i(x_j)}\right)}{x_j' - x_j} \right]. \tag{2.42}$$

Here $\Delta x = x_j' - x_j = 0.04$. The error from Eqs. (2.18), (2.19) also appear in the numerical calculation of $[\Gamma]$.

We observe an excellent agreement between thermodynamic factors computed from the PWTPI method and the $\Gamma_{ij}$ obtained from the central difference method Eq. (2.42). The central difference method requires two separate simulations (for two different mole fractions) to obtain an element of $[\Gamma]$ for a particular mole fraction. Our method requires only a single simulation to calculate all $[\Gamma]$ for a particular mole fraction. Finite size effects are observed in the computation of $[\Gamma]$ for $N_{\text{total}} = 100$ and $N_{\text{total}} = 200$ using the central difference method. Better statistics can be observed by having larger number of particles and simulating longer, but this is computationally expensive. It can be observed from Fig. 2.5 that our method for calculating $\Gamma$ has a much better convergence than the central difference method and does not suffer from finite size effects.

To test that the thermodynamic properties resulting from Eq. 2.7 indeed match those calculated in the open ensemble, we investigated the variation of the thermodynamic factors using the Permuted Widom test particle insertion method in a ternary system (W, A, B) of particles interacting with WCA potentials. Here, $x_{\text{A}} = x_{\text{B}}$. The matrix of thermodynamic factors were calculated as a function of $x_{\text{W}}$ with component B being chosen as the $n$-th component, but other choices lead to identical conclusions. The KB coefficients were obtained from MD simulations in the canonical (NVT) ensemble (with $x_{\text{A}} = x_{\text{B}}$). The expressions for $\Gamma_{ij}$ for ternary systems as a function of the KB coefficients can be found in Refs. [91, 112]. In Fig. 2.6, we plot the thermodynamic factors as a function of the mole fraction solvent (with number densities corresponding to a reduced pressure $P = 6.8$). There is an excellent agreement of the values of the thermodynamic factors calculated from KB coefficients as well as the PWTPI method. Clearly, the PWTPI method is not directly related to the KB theory approach. Fig. 2.6 shows that it leads to identical values of $\Gamma_{ij}$, confirming the validity of Eq. (2.7).

(a)

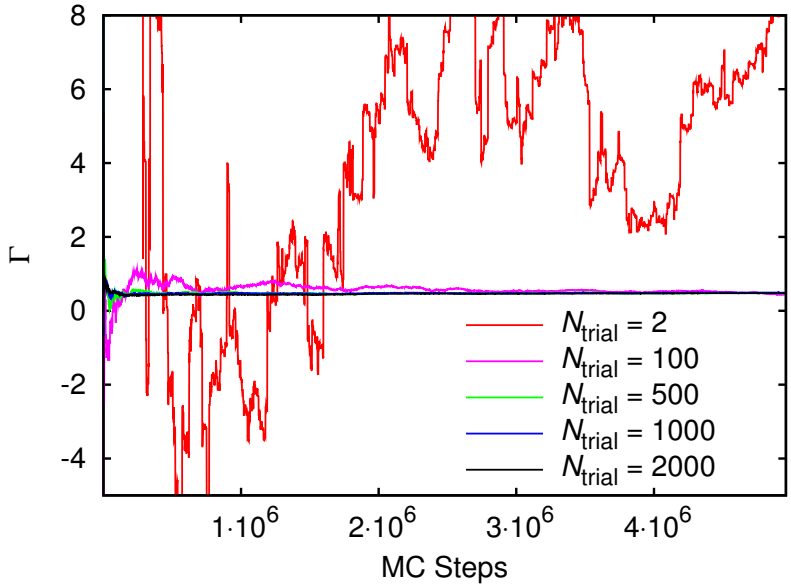


(b)

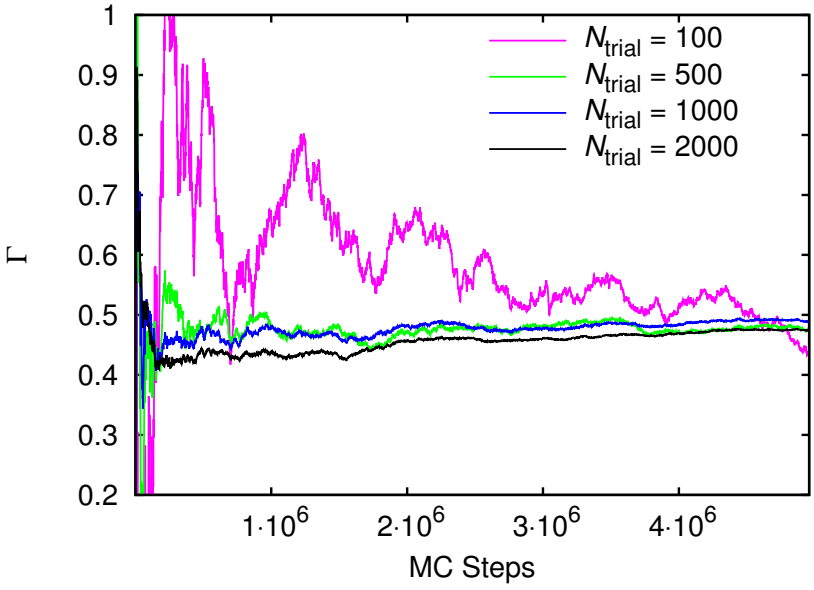


Figure 2.2: Thermodynamic factor $\Gamma$ as a function of the number of Monte Carlo steps for $N_{\text{total}} = 400$ for a different number of pre-generated trial positions ($N_{\text{trial}}$), $T = 2.0$ and $P = 2.8$. $N_{\text{trial}} = 2$ is the conventional WTPI method. Simulations for other values of $N_{\text{trial}}$ show that the convergence significantly improves for larger values of $N_{\text{trial}}$. Fig. (b) shows a closeup of Fig. (a).

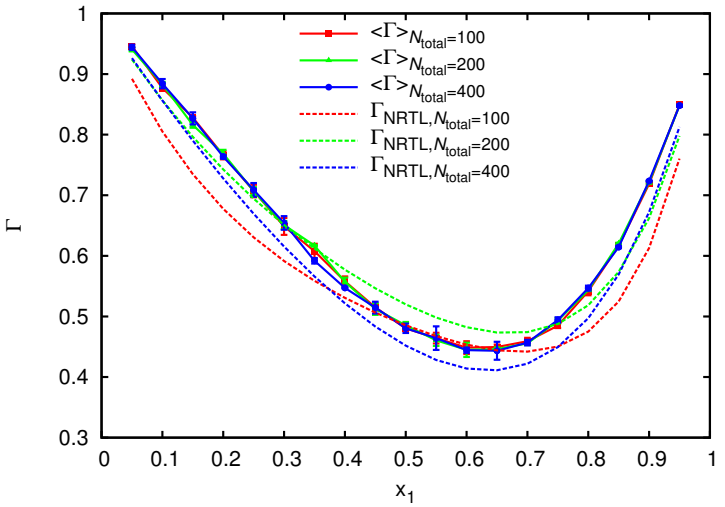


Figure 2.3: Thermodynamic factor $\Gamma$ for a binary Lennard-Jones system for different numbers of particles, $N_{\text{total}} = 100, 200, 400$, $N_{\text{trial}} = 500$, $T = 2.0$ and $P = 2.8$. The solid squares, triangles and circles denote $\langle\Gamma\rangle$ calculated by the PWTPI method for different number of particles (Eq. (2.32)). The dashed lines are the values for $\Gamma$ evaluated by fitting activity coefficients obtained via the conventional WTPI method to the NRTL model.

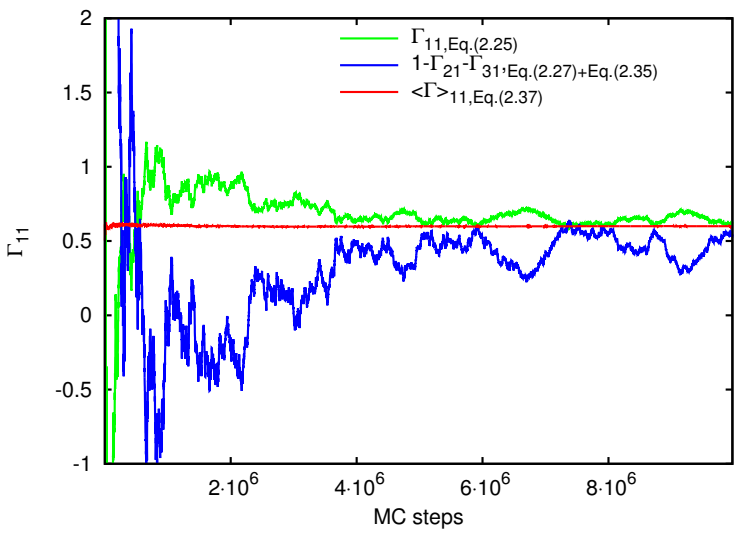


Figure 2.4: $\Gamma_{11}$ calculated from Eqs. (2.25), ((2.27)+(2.35)) and (2.37) for a ternary Lennard-Jones system as a function of the number of Monte Carlo steps for $N_{\text{total}} = 100$, $N_{\text{trial}} = 500$, $T = 2.0$, $P = 2.8$, $x_1 = 0.25$, $x_2 = 0.25$ and $x_3 = 0.5$.

(a)

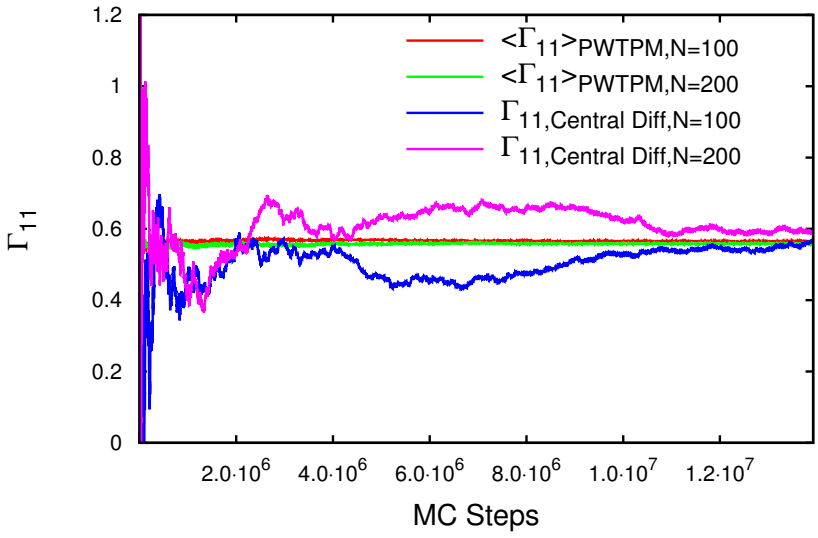
1.2
1
0.8
0.6
0.4
0.2
0
$\Gamma_{11}$
$<\Gamma_{11}>_{PWTPM,N=100}$
$<\Gamma_{11}>_{PWTPM,N=200}$
$\Gamma_{11,Central\ Diff,N=100}$
$\Gamma_{11,Central\ Diff,N=200}$
$2.0\cdot10^6$
$4.0\cdot10^6$
$6.0\cdot10^6$
$8.0\cdot10^6$
$1.0\cdot10^7$
$1.2\cdot10^7$
MC Steps

(b)

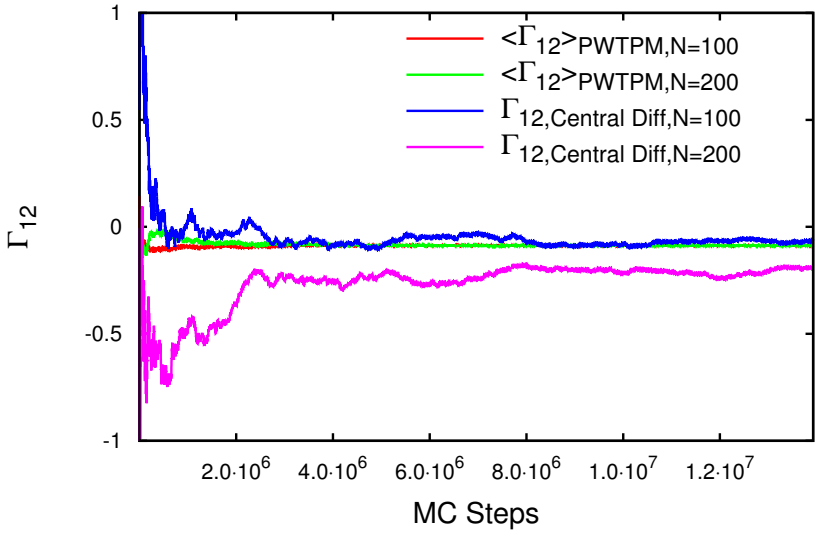
1
0.5
0
-0.5
-1
$\Gamma_{12}$
$<\Gamma_{12}>_{PWTPM,N=100}$
$<\Gamma_{12}>_{PWTPM,N=200}$
$\Gamma_{12,Central\ Diff,N=100}$
$\Gamma_{12,Central\ Diff,N=200}$
$2.0\cdot10^6$
$4.0\cdot10^6$
$6.0\cdot10^6$
$8.0\cdot10^6$
$1.0\cdot10^7$
$1.2\cdot10^7$
MC Steps

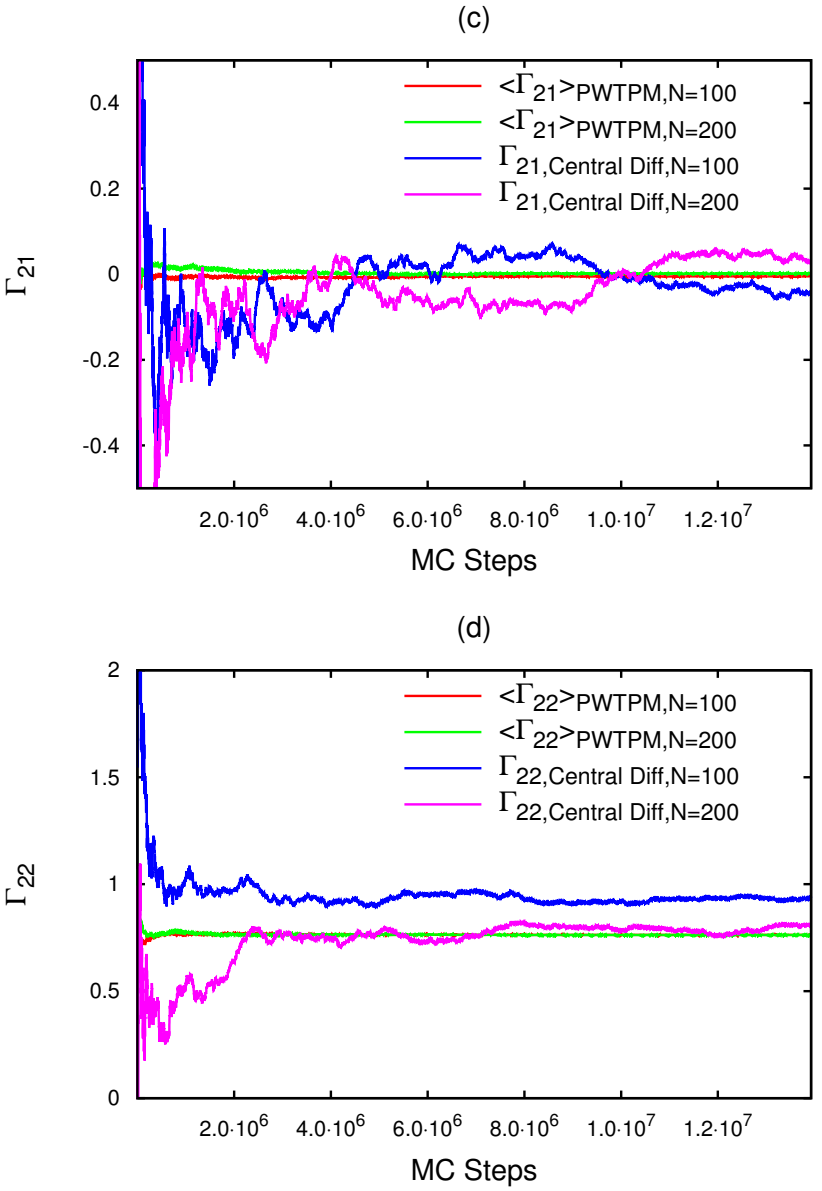


Figure 2.5: Thermodynamic factors (a) $\langle\Gamma_{11}\rangle$, (b) $\langle\Gamma_{12}\rangle$, (c) $\langle\Gamma_{21}\rangle$ and (d) $\langle\Gamma_{22}\rangle$ as a function of MC steps for a ternary Lennard-Jones system for $x_1 = 0.3, x_2 = 0.3, x_3 = 0.4$, $N_{\text{trial}} = 500$, $T = 2.0$ and $P = 2.8$. Two different methods are used to evaluate $\Gamma_{ij}$. The solid red line denote the $\langle\Gamma\rangle$ evaluated by the PWTPI method for $N_{\text{total}} = 100$. The solid green line denote the $\langle\Gamma\rangle$ evaluated by the PWTPI method for $N_{\text{total}} = 200$. The solid blue line is the $\Gamma$ evaluated from activity coefficients by a central difference method (Eq. (2.42)) for $N_{\text{total}} = 100$. The solid purple line is the $\Gamma$ evaluated from activity coefficients by a central difference method (Eq. (2.42)) for $N_{\text{total}} = 200$.

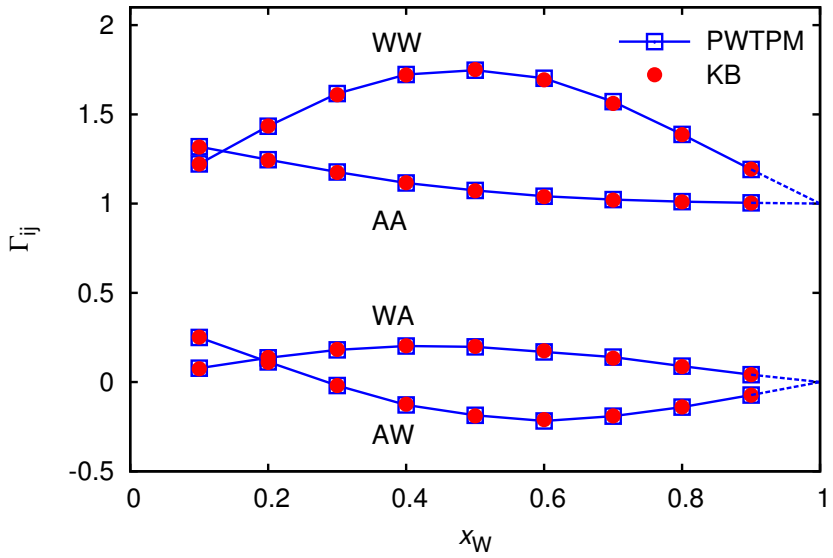


Figure 2.6: Thermodynamic factors for the ternary WCA system (W, A, B) with $x_A = x_B$ as a function of the mole fraction solvent ($x_W$) computed using two different methods: *(1)* KB coefficients computed from MD simulations in the canonical ensemble (Eq. 2.7, [91, 112]), circles; *(2)* MC simulations in the isobaric-isothermal ensemble using the PWTPI method, squares. $T = 2$ and in all cases $x_A = x_B$. The number densities of all systems are around $0.7$ and were set such that they correspond to a reduced pressure $P = 6.8$. AA, AW, WA, WW denote the various elements of the matrix of thermodynamic factors $\Gamma_{ij}$. The dotted lines denote the extrapolation to the $\Gamma_{ij}$ values at the limits. The matrix of thermodynamic factors computed from the PWTPI method agree excellently with the results computed from KB coefficients.

## 2.6 Conclusions

In this chapter, we have presented a new approach to compute the thermodynamic factors $\Gamma_{ij}$ of $n$-component systems using the PWTPI method. Our method was successfully tested for binary and ternary Lennard-Jones systems. We compared the results with the thermodynamic factors obtained from a numerical differentiation of activity coefficients using the central difference method and also the physical NRTL model. The results for the thermodynamic factors from both methods are in excellent agreement. Obtaining thermodynamic factors from computing/measuring activity coefficients and then differentiating these activity coefficients introduces numerical errors which can be reduced by computing the thermodynamic factors directly. The key advantage of our approach is that we can compute the matrix of thermodynamic factors [Γ] from a single simulation without any additional computational cost. By using the ideal gas reference state, the finite size effects in calculating the [Γ] have been eliminated. A practical approach to compute Kirkwood-Buff coefficients of individual ions in an ionic system directly from MD simulations in the canonical ensemble, leading to direct access of single-ion properties has been demonstrated. The applicability of this newly formulated Kirkwood-Buff theory has been independently validated by the PWTPI method.

# 3

# Advanced Monte Carlo Methods for Open Systems: CB/CFCMC vs. CFCMC vs. CBMC

Parts of this chapter are based on the following publication: A Torres-Knoop, S.P. Balaji, T.J.H. Vlugt, D. Dubbeldam, *A Comparison of Advanced Monte Carlo Methods for Open Systems: CFCMC vs. CBMC*, J. Chem. Theory Comput. **2014**, 10(3), 942-952 [70]

## 3.1 Introduction



When studying adsorption properties of materials, we are interested in the amount of molecules adsorbed (*e.g.* in units of mol/kg) as a function of the pressure and temperature. Computational studies, usually using Monte Carlo (MC) simulations, mimic this situation by attempting to insert and delete particles into and from the system in the grand-canonical ensemble or $\mu, V, T$ ensemble [51, 53, 77]. In this ensemble, the chemical potential $\mu$, the volume $V$ and the temperature $T$ are fixed. The fixed volume $V$ follows from the definition and volume of the studied crystal structure and the chemical potential $\mu$ can be directly related to the fugacity, which is obtained using an equation of state from the pressure. Because the chemical potential is fixed, the number of molecules fluctuates. Therefore the property that is computed is the average number of molecules per unit of volume. A system where the number of molecules varies is called an *open system*. All open-ensembles methods suffer from a major drawback: the probability that an insertion/deletion is accepted becomes vanishingly low at higher densities due to overlaps with the host structure and/or molecules that are already adsorbed. This makes it *e.g.* difficult to accurately compute the maximum loading of molecules in a structure (which is required in theoretical models like the Langmuir model).

To increase the number of successfully inserted molecules the Configurational-Bias Monte Carlo (CBMC) technique was developed [53, 115, 116]. In CBMC, instead of generating ideal gas configurations and trying to insert the molecule as a whole, chains are inserted segment by segment where the growth process is biased towards energetically favorable configurations. The scheme is therefore able to avoid (or at least reduce the amount of) configurations that overlap with the framework and other particles. This scheme also works for configurations of long molecules which become increasingly different from the gas phase as a function of chain length.

The CBMC method starts to have problems at medium densities and fails at high densities [77]. A new scheme to remedy this problem is the "Continuous Fractional Component Monte Carlo" (CFCMC) method of Shi and Maginn [78, 79, 81]. In this method the system is expanded with a single "fractional" molecule per component type that has a scaled interaction with the other molecules and with the framework. The scaling parameter $\lambda$ ranges from 0 to 1, with $\lambda = 0$ meaning the molecule is not felt by the surroundings (*i.e.* the host structure and the remaining molecules), while $\lambda = 1$ means the molecule is fully present and the interactions with the surrounding are at full strength. In addition to the usual set of MC moves, moves are now also performed on $\lambda$, attempting to increase and decrease it. Effectively, increasing $\lambda$ corresponds to "inflating" the molecule, and decreasing $\lambda$ corresponds to "deflating" the molecule. A change of $\lambda$ larger than 1 leads to insertion of a new chain. The fractional molecule is made integer, and a new molecule is randomly inserted into the system with the remainder of $\lambda$. This is the new fractional molecule. Similarly, a decrease of $\lambda$ below zero leads to a deletion of a molecule. Further details will be provided in the methodology section. The crucial point to note here, however, is that the $\lambda$ moves can be biased, ideally making the $\lambda$-histogram flat. The method therefore is able to *force* molecules in and out of the system, thereby allowing the

open ensemble to be efficiently implemented in a simulation.

There are few papers investigating the use of CFCMC for adsorption simulations. Ref. [77] demonstrated excellent agreement between CFCMC and CBMC for a few simple cases: single component adsorption isotherms of small guest molecules in several zeolites and MOFs. In this chapter, we combine the CFCMC and CBMC in a CB/CFCMC hybrid method and evaluate this method with simulations in the grand-canonical and Gibbs ensemble. We also compare the CB/CFCMC hybrid method with the CFCMC and CBMC in a more complex scenario: alkanes in $Fe_2(BDP)_3$. The algorithms are implemented in the RASPA code [117]. We will show that and CB/CFCMC and CFCMC are very significant improvements over conventional MC and even over CBMC.



## 3.2 Methodology

### 3.2.1. Configurational-Bias Monte Carlo

The CBMC framework is based on work by Rosenbluth and Rosenbluth [116] and developed by a variety of researchers [115, 118–123]. In the CBMC scheme, it is convenient to split the total potential energy $U$ of a segment of a molecule into two parts:

$$U = U^{\text{int}} + U^{\text{ext}}. \tag{3.1}$$

The first part of the potential, the internal bonded potential $U^{\text{int}}$, is used for the generation of trial positions. The second part, the external potential $U^{\text{ext}}$, is used to bias the selection of a site from a set of trial positions. This bias is exactly removed by adjusting the acceptance rules. In the CBMC technique a molecule is grown segment-by-segment. For each segment a set of $k$ trial positions is generated with a probability proportional to the Boltzmann factor of the internal energy $U^{\text{int}}$. The number of trial positions $k$ is usually between 10 and 20. For each trial position $j$ of segment $i$ the external energy $U_i^{\text{ext}}(j)$ is computed [53]. One of these trial positions is selected with a probability proportional to its Boltzmann factor

$$p_i(j) = \frac{\exp[-\beta U_i^{\text{ext}}(j)]}{\sum_{l=1}^{k} \exp[-\beta U_i^{\text{ext}}(l)]} = \frac{\exp[-\beta U_i^{\text{ext}}(j)]}{w(i)}. \tag{3.2}$$

where $\beta = 1/k_{\text{B}}T$ is the inverse temperature, $k_{\text{B}}$ the Boltzmann factor. The selected trial position is added to the chain and the procedure is repeated until the entire molecule has been grown. For this newly grown molecule the Rosenbluth factor of the new configuration $W^{\text{new}}$ is computed

$$W^{\text{new}} = \prod_{i=1}^{n} w(i), \tag{3.3}$$

in which $n$ is the number of segments in the chain. To compute the old Rosenbluth factor $W^{\text{old}}$ of an already existing chain, $k-1$ trial positions are generated for each segment. These positions, together with the already existing position, form the set of $k$ trial positions. $W^{\text{old}}$ is calculated in an analogous way [53].

The acceptance rules for CBMC insertion and deletion moves in the grand-canonical ensemble are expressed as [53, 124, 125]

$$\mathrm{acc}(N \to N+1) = \min\left(1, \frac{f\beta V}{N+1}\frac{W^{\mathrm{new}}}{\langle W^{\mathrm{IG}}\rangle}\right) \tag{3.4}$$

$$\mathrm{acc}(N \to N-1) = \min\left(1, \frac{N}{f\beta V}\frac{\langle W^{\mathrm{IG}}\rangle}{W^{\mathrm{old}}}\right) \tag{3.5}$$



in which $\langle W^{\mathrm{IG}}\rangle$ is the average Rosenbluth factor of an isolated molecule in the gas phase, $f$ is the fugacity, $V$ the volume and $N$ the number of molecules. The pressures and fugacities are related via the equation of state of the gas phase. The "reinsertion"-move removes a randomly selected molecule and reinserts it at a random position. For rigid molecules it uses orientational biasing [77], and for chains the molecule is fully regrown (the internal configuration is modified). To properly sample the internal structure (*i.e.* bond/bend/torsions) the "partial reinsertion" move is useful. Several atoms of the molecule are kept fixed, while others are regrown. Because there is already space for the atoms the acceptance ratios are high. The acceptance rule for full and partial regrowth is

$$\mathrm{acc}\,(\mathrm{old} \to \mathrm{new}) = \min\left(1, \frac{W^{\mathrm{new}}}{W^{\mathrm{old}}}\right). \tag{3.6}$$

For mixtures, especially at higher density, the "identity-switch" move becomes crucial. The identity-change trial move [126–129] is called semi-grand ensemble. One of the component types is selected at random (here: A) and for a randomly selected molecule of this component type, an attempt is made to change its identity. The new identity of this component (here: B) is also selected randomly out of all component types (but excluding component type A). The expression for the acceptance rule is [124, 126, 129]

$$\mathrm{acc}\,(\mathrm{A} \to \mathrm{B}) = \min\left(1, \frac{W^{\mathrm{new}} f_B \langle W_A^{\mathrm{IG}}\rangle N_A}{W^{\mathrm{old}} f_A \langle W_B^{\mathrm{IG}}\rangle (N_B+1)}\right), \tag{3.7}$$

where $f_A$ and $f_B$ are the fugacities of components $A$ and $B$, and $N_A$ and $N_B$ are the number of particles. Since the introduction of CBMC, the method has been extended to include grow paths for branched molecules [53, 63, 64, 124, 130–133], cyclic molecules [134–137] and reactive CBMC [138, 139].

### 3.2.2. Continuous Fractional Component Monte Carlo

Continuous Fractional Component Monte Carlo (CFCMC) was developed by Shi and Maginn [78] inspired by a group of schemes known as "expanded ensembles" [140, 141]. The system is expanded with an additional particle which interactions with the surrounding molecules are scaled using a parameter $\lambda$. Various choices for the scaling are possible. In the original CFCMC method, and also in this work, Lennard-Jones

(LJ) interactions $u_{\mathrm{LJ}}(r)$ and electrostatic interactions $u_{\mathrm{Coul}}$ are scaled as [78]

$$u_{\mathrm{LJ}}(r) = \lambda 4\epsilon \left[ \frac{1}{\left[\frac{1}{2}(1-\lambda)^2 + \left(\frac{r}{\sigma}\right)^6\right]^2} - \frac{1}{\left[\frac{1}{2}(1-\lambda)^2 + \left(\frac{r}{\sigma}\right)^6\right]} \right] \tag{3.8}$$

$$u_{\mathrm{Coul}} = \lambda^5 \frac{1}{4\pi\varepsilon_0} \frac{q_i q_j}{r}. \tag{3.9}$$

where $\epsilon_0$ is the dielectric constant in vacuum, $r$ is the interatomic distance, $q$ is the atomic charge, $\epsilon$ is the LJ strength parameter and $\sigma$ is the LJ size parameter.



The modified form of the conventional LJ potential forces the potential to remain finite when $r \to 0$ for $\lambda \neq 1$. The scaled potential has the correct behavior at the limits of $\lambda = 0$ and $\lambda = 1$, *i.e.* for $\lambda = 0$ there are no interactions, and for $\lambda = 1$ the conventional LJ and Coulombic interactions are recovered. Note that only the inter-molecular energy ($U^{\mathrm{inter}}$) is scaled. Many variations on the algorithm are possible. For example $\lambda$ can be changed per molecule or per atom. In any case the method slowly "inflates" and "deflates" the molecule like a balloon.

CFCMC uses conventional MC for thermalization (such as translations, rotations, and/or MC-MD hybrid moves [142, 143]), but in addition attempts to change $\lambda$ of the fractional molecule using $\lambda_{\mathrm{n}} = \lambda_{\mathrm{o}} + \Delta\lambda$. The value of $\Delta\lambda$ is chosen uniformly between $-\Delta\lambda^{\max}$ and $+\Delta\lambda^{\max}$ and adjusted to achieve approximately 50% acceptance. However, many systems show behavior where $\lambda$-changes are difficult [77–79] because in the Boltzmann ensemble the distribution of $\lambda$ can go through a deep minimum. An additional bias $\eta$ on $\lambda$ can be used, where each state of $\lambda$ has an associated biasing factor $\eta$. This bias will be removed by the acceptance rules. A careful calibration of $\eta$ will make the $\lambda$ histograms flat and hence can avoid situations where the system gets stuck in a certain $\lambda$-range. There are three possible outcomes of a change from $\lambda_{\mathrm{o}}$ to $\lambda_{\mathrm{n}}$:

- $\lambda(n)$ remains between 0 and 1:
  The change in energy of the particle with the new $\lambda_{\mathrm{n}}$ compared to the old energy is computed and the move is accepted using

  $$p_{\mathrm{acc}} = \min\left(1, \exp[-\beta\left(U_{\mathrm{inter}}(n) - U_{\mathrm{inter}}(o)\right) + \eta(\lambda_{\mathrm{n}}) - \eta(\lambda_{\mathrm{o}})]\right) \tag{3.10}$$

  There is no change in the number of particles, the positions, or in the intra-molecular energies. Only $\lambda$ and the inter-molecular energy are changed.

- $\lambda_{\mathrm{n}}$ becomes larger than 1:
  When $\lambda_{\mathrm{n}}$ exceeds unity, *i.e* $\lambda_{\mathrm{n}} = 1 + \epsilon$, the current fractional molecule is made fully present ($\lambda = 1$), and an additional particle is randomly inserted with $\lambda = \epsilon$. In the original paper [78], an ideal gas molecule is taken form a reservoir of equilibrated gas phase molecules stored in the memory of the computer. In our implementation, the ideal gas molecule is generated "on the fly" during the simulation.

- $\lambda_{\mathrm{n}}$ becomes smaller than 0:
  When $\lambda_{\mathrm{n}}$ falls below 0, *i.e* $\lambda_{\mathrm{n}} = -\epsilon$, the current fractional molecule is removed from the system ($\lambda = 0$) and a new fractional molecule is chosen with $\lambda = 1 - \epsilon$.

The acceptance rules for insertion and deletion in the grand-canonical ensemble are [77, 78]

$$p_{\text{acc}}\left(N \rightarrow N+1\right) = \min\left(1, \frac{f\beta V}{N+1}\exp[-\beta\left(U_{\text{inter}}\left(n\right) - U_{\text{inter}}\left(o\right)\right)]\right.$$
$$\left.\exp[\eta\left(\lambda_{\text{n}}\right) - \eta\left(\lambda_{\text{o}}\right)]\right) \tag{3.11}$$

$$p_{\text{acc}}\left(N \rightarrow N-1\right) = \min\left(1, \frac{N}{f\beta V}\exp[-\beta\left(U_{\text{inter}}\left(n\right) - U_{\text{inter}}\left(o\right)\right)]\right.$$
$$\left.\exp[\eta\left(\lambda_{\text{n}}\right) - \eta\left(\lambda_{\text{o}}\right)]\right) \tag{3.12}$$

where $N$ is the number of *integer* molecules. Hence, measured properties and loadings should exclude the fractional molecule.

The CFCMC method is able to force molecules into and out of the system. If the molecule is too quickly removed after insertion then nothing is gained. The environment should be able to adjust to the new insertion and equilibrate properly. The adjustment is also called thermalization. CFCMC uses conventional MC moves such as translation, rotation, and/or MC-MD hybrid moves for thermalization. In our implementation we also use (partial-)reinsertion moves using configurational biasing (identical to CBMC), for both integer molecules and the fractional molecules. The insertion of an additional molecule is already biased using $\lambda$-biasing and as soon as the molecule is present in the system the reinsertion is able to efficiently move the molecules around in the system. For mixtures, we use the identity-switch move but only on integer molecules because each component should always have one and only one fractional molecule.

Shi and Maginn found that Wang-Landau sampling is very efficient in obtaining the biasing factors for CFCMC [78, 79, 81], and our experience confirms this. The objective of the Wang-Landau sampling method [144, 145] is to make all system energy states equally probable. In CFCMC this translates in making all system $\lambda$ states equally probable. During a random walk the weights are iteratively adjusted using importance sampling. The $\lambda$ range is for example divided into 20 bins. Initially, all biasing factors are set to zero. During equilibration the bin corresponding to the current $\lambda$ is modified according to $\eta\left(\lambda_j\right) \rightarrow \eta\left(\lambda_j\right) - \nu$ after a MC move attempt, where $\nu$ is a scaling parameter initially set to 0.01. Histograms are measured and every 10000 attempts checked for flatness. The histogram is considered sufficiently flat when all bins are at least 30% as often visited as the most visited bin. If so, then the histograms are set to zero and the scaling factor is modified to $\nu \rightarrow \frac{1}{2}\nu$. Equilibration of $\eta$ can be stopped once the value of $\nu$ is lower than $10^{-6}$.

### 3.2.3. Combining Configurational-Bias and Continuous Fractional Component Monte Carlo

The insertion and deletion scheme of CFCMC can in certain cases be improved by fractionally growing and retracing a molecule at a fixed $\lambda$ using CBMC. In this section, we derive the acceptance rules for the Continuous Fractional Component Monte Carlo method combined with Configurational-Bias Monte Carlo (CB/CFCMC) in the Gibbs Ensemble. In the Gibbs ensemble, the two simulation boxes are in equilibrium with each other. The two boxes are denoted by "1" and "2" respectively. In the Gibbs ensemble, the equilibrium conditions are $\mu_1 = \mu_2$, $P_1 = P_2$, $\beta_1 = \beta_2$, where $\mu_i$ is the chemical potential of molecules in box $i$, $P_i$ is the pressure and $\beta = 1/(k_{\mathrm{B}}T)$. We consider pure-component systems only, as the extension to mixtures is trivial [146]. Let $N_t$ denote the total number of molecules in the system. $N_1, N_2$ are the number of molecules in the two phases/boxes respectively. $V_1, V_2$ are the volumes of the boxes 1 and 2 respectively and $V_{\mathrm{t}}$ is the total volume ($V_{\mathrm{t}} = V_1 + V_2$). The partition function for the conventional Gibbs ensemble is [53],

$$Q(N_{\mathrm{t}}, V_1, V_2, T) = \sum_{N_1=0}^{N_{\mathrm{t}}} \frac{1}{\Lambda^{3N_{\mathrm{t}}} N_1! N_2! V_{\mathrm{t}}} \int_0^{V_{\mathrm{t}}} \mathrm{d}V_1 V_1^{N_1} (V_{\mathrm{t}} - V_2)^{N_2} \int \mathrm{d}s_2^{N_2} \exp[-\beta U_2(s_2^{N_2})] \int \mathrm{d}s_1^{N_1} \exp[-\beta U_1(s_1^{N_1})] \tag{3.13}$$

where $s_1^{N_1}, s_2^{N_2}$ are the configurations of all molecules in boxes 1 and 2 respectively and $U_1(s_1^{N_1}), U_2(s_2^{N_2})$ are the total potential energies of the molecules in boxes 1 and 2. For the Continuous Fractional Component Gibbs ensemble, we introduce one fractional molecule in each of the two boxes. We define $\lambda$ as the parameter to describe the interactions of the fractional molecule with the other molecules, with $\lambda \in [0, 1]$. If $\lambda = 0$, the molecule has no intermolecular interactions with the other molecules while for $\lambda = 1$, the interactions of the fractional molecule with the other molecules are fully developed. The fractional molecule in each box is denoted by $N_{\mathrm{f},1}, N_{\mathrm{f},2}$. $\lambda$ is constraint by $\lambda_1 + \lambda_2 = 1$ where $\lambda_1$ and $\lambda_2$ refer to the $\lambda$ in the simulation boxes 1 and 2 respectively. Henceforth, the coupling parameter will be denoted by $\lambda$ only and it will specifically refer to box 1. Therefore the coupling parameter for the fractional molecule inside box 2 is denoted by $1 - \lambda$. The potential energies of the boxes 1 and 2 are now denoted as $U_1(s_1^{N_1, N_{\mathrm{f},1}}, \lambda)$ and $U_2(s_2^{N_2, N_{\mathrm{f},2}}, 1 - \lambda)$ respectively. The CFCMC scheme now includes trial moves that change $\lambda$. The partition function for this system is [79]

$$Q(N_{\mathrm{t}}, V_1, V_2, T) = \int_0^1 \mathrm{d}\lambda \sum_0^{N_{\mathrm{t}}} \frac{1}{V_{\mathrm{t}}} \int_0^{V_{\mathrm{t}}} \mathrm{d}V_1 Z(N_1, N_2, V_1, V_2, N_{\mathrm{f},1}, N_{\mathrm{f},2}, \lambda, T) \tag{3.14}$$

where,

$$Z(N_1,N_2,V_1,V_2,N_{f,1},N_{f,2},\lambda,T) = \frac{V_1^{N_1+1}V_2^{N_2+1}}{\Lambda^{3N_t}N_1!N_2!} \int ds_2^{N_2,N_{f,2}} \exp[-\beta U_2(s_2^{N_2,N_{f,2}},1-\lambda)] \int ds_1^{N_1,N_{f,1}} \exp[-\beta U_1(s_1^{N_1,N_{f,1}},\lambda)] \quad (3.15)$$



Ideally, changes in $\lambda$ should be made in such a way that there is a flat distribution of $\lambda$. Suitable bias factors $\eta(\lambda)$ can be introduced to improve the probability of transitions in $\lambda$. The bias factors can be calculated on the fly using the Wang-Landau method [144]. The partition function including the bias factor for box 1, $\eta(\lambda)$, can now be expressed as

$$Q_{\text{biased}}(N_t,V_1,V_2,T) = \int_0^1 d\lambda \sum_0^{N_t}\sum_{j=0}^{M} \frac{1}{V_t}\int_0^{V_t} dV_1 \exp[\eta(\lambda)] Z_{\text{biased}}(N_1,N_2,V_1,V_2,N_{f,1},N_{f,2},\lambda,T) \quad (3.16)$$

$$Z_{\text{biased}}(N_1,N_2,V_1,V_2,N_{f,1},N_{f,2},\lambda,T) = \frac{V_1^{N_1+1}V_2^{N_2+1}}{\Lambda^{3N_t}N_1!N_2!} \int ds_2^{N_2,N_{f,2}} \exp[-\beta U_2(s_2^{N_2,N_{f,2}},1-\lambda)] \int ds_1^{N_1,N_{f,1}} \exp[-\beta U_1(s_1^{N_1,N_{f,1}},\lambda)] \quad (3.17)$$

The probability of the system to exist in a certain state "m" is expressed by

$$p_m = \frac{1}{Q(N_t,V_1,V_2,T)} \cdot \frac{V_1^{N_1+1}V_2^{N_2+1}}{\Lambda^{3N_t}N_1!N_2!V_t} \exp[-\beta(U_1(s_1^{N_1,N_{f,1}},\lambda)+U_2(s_2^{N_2,N_{f,2}},1-\lambda))+\eta(\lambda)] \quad (3.18)$$

Averages in the Boltzmann ensemble (denoted by $\langle\cdots\rangle$) follow directly from biased averages (denoted by $\langle\cdots\rangle_{\text{biased}}$) according to [51]

$$\langle A\rangle = \frac{\langle A\exp[-\eta(\lambda)]\rangle_{\text{biased}}}{\langle\exp[-\eta(\lambda)]\rangle_{\text{biased}}} \quad (3.19)$$

In the Monte Carlo simulation, there are three Monte Carlo moves possible:

1. Change the position or orientation of a randomly selected molecule in a randomly selected box (either the whole or a fractional molecule)
2. Change the volume of the boxes while keeping the total volume constant

3. Change the coupling parameter $\lambda$
   The change in $\lambda$ can be further divided into 3 cases ($\lambda_n$ being the value of $\lambda$ in the new configuration and $\lambda_o$ being the value of $\lambda$ in the old configuration):
   (a) $0 < \lambda_\mathrm{n} < 1$
   (b) $\lambda_\mathrm{n} < 0$
   (c) $\lambda_\mathrm{n} > 1$.



For the displacement or rotation move, a random molecule (a whole or the fractional molecule) is chosen and a random displacement (or rotation) is performed for the chosen molecule. The old state is denoted by "o" and the new state is denoted by "n". The probabilities to exist in states "o" and "n" are expressed as,

$$p_\mathrm{o} = \frac{1}{Q(N_\mathrm{t}, V_1, V_2, T)} \cdot \frac{V_{1,\mathrm{o}}^{N_{1,\mathrm{o}}+1} V_{2,\mathrm{o}}^{N_{2,\mathrm{o}}+1}}{\Lambda^{3N_\mathrm{t}} N_{1,\mathrm{o}}! N_{2,\mathrm{o}}! V_\mathrm{t}} \exp[-\beta(U_{1,\mathrm{o}}(s_1^{N_1,N_{\mathrm{f},1}}, \lambda_\mathrm{o}) + U_{2,\mathrm{o}}(s_2^{N_2,N_{\mathrm{f},2}}, 1-\lambda_\mathrm{o})) + \eta(\lambda_\mathrm{o})] \tag{3.20}$$

$$p_\mathrm{n} = \frac{1}{Q(N_\mathrm{t}, V_1, V_2, T)} \cdot \frac{V_{1,\mathrm{o}}^{N_{1,\mathrm{o}}+1} V_{2,\mathrm{o}}^{N_{2,\mathrm{o}}+1}}{\Lambda^{3N_\mathrm{t}} N_{1,\mathrm{o}}! N_{2,\mathrm{o}}! V_\mathrm{t}} \exp[-\beta(U_{1,\mathrm{n}}(s_1^{N_1,N_{\mathrm{f},1}}, \lambda_\mathrm{n}) + U_{2,\mathrm{n}}(s_2^{N_2,N_{\mathrm{f},2}}, 1-\lambda_\mathrm{n})) + \eta(\lambda_\mathrm{n})] \tag{3.21}$$

Since we are not performing a change in $\lambda$, the bias factors are equal: $\lambda_\mathrm{o} = \lambda_\mathrm{n}$. The acceptance rule is

$$\mathrm{acc}(\mathrm{o} \to \mathrm{n}) = \min(1, \exp[-\beta(U_{1,\mathrm{n}}(s_1^{N_1,N_{\mathrm{f},1}}, \lambda_\mathrm{n}) + U_{2,\mathrm{n}}(s_2^{N_2,N_{\mathrm{f},2}}, 1-\lambda_\mathrm{n}) - U_{1,\mathrm{o}}(s_1^{N_1,N_{\mathrm{f},1}}, \lambda_\mathrm{o}) - U_{2,\mathrm{o}}(s_2^{N_2,N_{\mathrm{f},2}}, 1-\lambda_\mathrm{o}))]) \tag{3.22}$$

For the volume change move, one of the simulation boxes is chosen randomly and a random walk is performed in $\ln(V_1/V_2)$. This has the advantages that the domain of the random walk coincides with all the possible values of $V_1$ and the maximum volume change turns out to be less sensitive to the density [53]. The probabilities to be in the old and new configurations are,

$$p_\mathrm{o} = \frac{1}{Q(N_\mathrm{t}, V_1, V_2, T)} \cdot \frac{V_{1,\mathrm{o}}^{N_{1,\mathrm{o}}+2} V_{2,\mathrm{o}}^{N_{2,\mathrm{o}}+2}}{\Lambda^{3N_\mathrm{t}} N_{1,\mathrm{o}}! N_{2,\mathrm{o}}! V_\mathrm{t}} \exp[-\beta(U_{1,\mathrm{o}}(s_1^{N_1,N_{\mathrm{f},1}}, \lambda_\mathrm{o}) + U_{2,\mathrm{o}}(s_2^{N_2,N_{\mathrm{f},2}}, 1-\lambda_\mathrm{o})) + \eta(\lambda_\mathrm{o})] \tag{3.23}$$

$$p_\mathrm{n} = \frac{1}{Q(N_\mathrm{t}, V_1, V_2, T)} \cdot \frac{V_{1,\mathrm{n}}^{N_{1,\mathrm{o}}+2} V_{2,\mathrm{n}}^{N_{2,\mathrm{o}}+2}}{\Lambda^{3N_\mathrm{t}} N_{1,\mathrm{o}}! N_{2,\mathrm{o}}! V_\mathrm{t}} \exp[-\beta(U_{1,\mathrm{n}}(s_1^{N_1,N_{\mathrm{f},1}}, \lambda_\mathrm{n}) + U_{2,\mathrm{n}}(s_2^{N_2,N_{\mathrm{f},2}}, 1-\lambda_\mathrm{n})) + \eta(\lambda_\mathrm{n})] \tag{3.24}$$

As $\lambda$ does not depend on the volume, we have $\lambda_{\rm o} = \lambda_{\rm n}$ and the acceptance rule becomes

$$\begin{aligned}\mathrm{acc}(\mathrm{o}\to\mathrm{n}) = \min\Bigg(1, \frac{V_{1,\mathrm{n}}^{N_{1,\mathrm{o}}+2} V_{2,\mathrm{n}}^{N_{2,\mathrm{o}}+2}}{V_{1,\mathrm{o}}^{N_{1,\mathrm{o}}+2} V_{2,\mathrm{o}}^{N_{2,\mathrm{o}}+2}} \exp[-\beta(U_{1,\mathrm{n}}(s_1^{N_1,N_{\mathrm{f},1}}, \lambda_{\mathrm{n}}) \\ + U_{2,\mathrm{n}}(s_2^{N_2,N_{\mathrm{f},2}}, 1-\lambda_{\mathrm{n}}) - U_{1,\mathrm{o}}(s_1^{N_1,N_{\mathrm{f},1}}, \lambda_{\mathrm{o}}) \\ - U_{2,\mathrm{o}}(s_2^{N_2,N_{\mathrm{f},2}}, 1-\lambda_{\mathrm{o}}))]\Bigg)\end{aligned} \tag{3.25}$$

Maginn *et al.* [79] have used random walks in $(V_1/V_2)$ instead. The acceptance rule is then expressed as

$$\begin{aligned}\mathrm{acc}(\mathrm{o}\to\mathrm{n}) = \min\Bigg(1, \frac{V_{1,\mathrm{n}}^{N_{1,\mathrm{o}}+1} V_{2,\mathrm{n}}^{N_{2,\mathrm{o}}+1}}{V_{1,\mathrm{o}}^{N_{1,\mathrm{o}}+1} V_{2,\mathrm{o}}^{N_{2,\mathrm{o}}+1}} \exp[-\beta(U_{1,\mathrm{n}}(s_1^{N_1,N_{\mathrm{f},1}}, \lambda_{\mathrm{n}}) \\ + U_{2,\mathrm{n}}(s_2^{N_2,N_{\mathrm{f},2}}, 1-\lambda_{n}) - U_{1,\mathrm{o}}(s_1^{N_1,N_{\mathrm{f},1}}, \lambda_{\mathrm{o}}) \\ - U_{2,\mathrm{o}}(s_2^{N_2,N_{\mathrm{f},2}}, 1-\lambda_{\mathrm{o}}))]\Bigg)\end{aligned} \tag{3.26}$$

In the $\lambda$ change move, the $\lambda$ is changed by an amount $\Delta\lambda$: $\lambda_{\rm o}$ and $\lambda_{\rm n}$ refer to the value of $\lambda$ in the old and new configurations respectively: $\lambda_{\rm n} = \lambda_{\rm o} + \Delta\lambda$. When $0 < \lambda_n < 1$, the pseudocoupling parameter increases/decreases. The probabilities of existing in the old and new configurations are expressed as,

$$\begin{aligned}p_{\mathrm{o}} =& \frac{1}{Q(N_{\mathrm{t}}, V_1, V_2, T)} \cdot \frac{V_{1,\mathrm{o}}^{N_{1,\mathrm{o}}+1} V_{2,\mathrm{o}}^{N_{2,\mathrm{o}}+1}}{\Lambda^{3N_{\mathrm{t}}} N_{1,\mathrm{o}}! N_{2,\mathrm{o}}! V_{\mathrm{t}}} \\ & \exp[-\beta(U_{1,\mathrm{o}}(s_1^{N_1,N_{\mathrm{f},1}}, \lambda_{\mathrm{o}}) + U_{2,\mathrm{o}}(s_2^{N_2,N_{\mathrm{f},2}}, 1-\lambda_{\mathrm{o}})) + \eta(\lambda_{\mathrm{o}})]\end{aligned} \tag{3.27}$$

$$\begin{aligned}p_{\mathrm{n}} =& \frac{1}{Q(N_{\mathrm{t}}, V_1, V_2, T)} \cdot \frac{V_{1,\mathrm{o}}^{N_{1,\mathrm{o}}+1} V_{2,\mathrm{o}}^{N_{2,\mathrm{o}}+1}}{\Lambda^{3N_{\mathrm{t}}} N_{1,\mathrm{o}}! N_{2,\mathrm{o}}! V_{\mathrm{t}}} \\ & \exp[-\beta(U_{1,\mathrm{n}}(s_1^{N_1,N_{\mathrm{f},1}}, \lambda_{\mathrm{n}}) + U_{2,\mathrm{n}}(s_2^{N_2,N_{\mathrm{f},2}}, 1-\lambda_{\mathrm{n}})) + \eta(\lambda_{\mathrm{n}})]\end{aligned} \tag{3.28}$$

As the number of molecules in each box is the same for the old and new configurations, the acceptance criterion becomes

$$\begin{aligned}\mathrm{acc}(\mathrm{o}\to\mathrm{n}) =& \min(1, \exp[-\beta(U_{1,\mathrm{n}}(s_1^{N_1,N_{\mathrm{f},1}}, \lambda_{\mathrm{n}}) + U_{2,\mathrm{n}}(s_2^{N_2,N_{\mathrm{f},2}}, 1-\lambda_{\mathrm{n}}) \\ & - U_{1,\mathrm{o}}(s_1^{N_1,N_{\mathrm{f},1}}, \lambda_{\mathrm{o}}) - U_{2,\mathrm{o}}(s_2^{N_2,N_{\mathrm{f},2}}, 1-\lambda_{\mathrm{o}})) + \eta(\lambda_{\mathrm{n}}) - \eta(\lambda_{\mathrm{o}})])\end{aligned} \tag{3.29}$$

When $\lambda_{\rm n} < 0$ or $\lambda_{\rm n} > 1$, molecules are exchanged between the phases/boxes. First, $\lambda_{\rm n}$ is set according to $\lambda_{\rm n} = \lambda_{\rm o} + \Delta\lambda$. If $\lambda_{\rm n} > 1$, then we set $\lambda_{\rm n} \to \lambda_{\rm n} - 1$. If $\lambda_{\rm n} < 0$, then we set $\lambda_{\rm n} \to \lambda_{\rm n} + 1$. We assume the molecule is transferred from box 2 to box 1 (the acceptance rule for the opposite transfer follows from a permutation

of the labels of the boxes). In box 1, the existing fractional molecule is converted to a whole molecule and a new fractional molecule with $\lambda_\mathrm{n}$ is randomly inserted in the box. In box 2, the existing fractional molecule is deleted and a random whole molecule is chosen and converted to a new fractional molecule with $1-\lambda_\mathrm{n}$. To make things clear, let us take an example. Assume the pseudocoupling factors are $\lambda_{1,\mathrm{o}}=0.9$ and $\lambda_{2,\mathrm{o}}=0.1$ for box 1 and 2 respectively. If $\Delta\lambda=+0.3$, $\lambda_{1,\mathrm{n}}=0.2$ and $\lambda_{2,\mathrm{n}}=0.8$.

For the particle swap move in the Continuous Fractional Gibbs ensemble, the condition for detailed balance is,

$$p_\mathrm{o}\cdot\alpha(\mathrm{o}\to\mathrm{n})\cdot\mathrm{acc}(\mathrm{o}\to\mathrm{n})=p_\mathrm{n}\cdot\alpha(\mathrm{n}\to\mathrm{o})\cdot\mathrm{acc}(\mathrm{n}\to\mathrm{o}) \tag{3.30}$$

where $\alpha(\mathrm{o}\to\mathrm{n})$ is the probability to select the trial move from $o$ to $n$ and $\mathrm{acc}(\mathrm{o}\to\mathrm{n})$ is the probability of accepting this trial move. Assume the molecule is inserted in box 1 and deleted from box 2. The probabilities of existing in a states "o" and "n"

$$\begin{aligned} p_\mathrm{o} =& \frac{1}{Q(N_\mathrm{t},V_1,V_2,T)}\cdot\frac{V_{1,\mathrm{o}}^{N_{1,\mathrm{o}}+1}V_{2,\mathrm{o}}^{N_{2,\mathrm{o}}+1}}{\Lambda^{3N_\mathrm{t}}N_{1,\mathrm{o}}!N_{2,\mathrm{o}}!V_\mathrm{t}} \\ & \exp[-\beta(U_{1,\mathrm{o}}(s_1^{N_1,N_{\mathrm{f},1}},\lambda_\mathrm{o})+U_{2,\mathrm{o}}(s_2^{N_2,N_{\mathrm{f},2}},1-\lambda_\mathrm{o}))+\eta(\lambda_\mathrm{o})] \end{aligned} \tag{3.31}$$

$$\begin{aligned} p_\mathrm{n} =& \frac{1}{Q(N_\mathrm{t},V_1,V_2,T)}\cdot\frac{V_{1,\mathrm{o}}^{N_{1,\mathrm{o}}+2}V_{2,\mathrm{o}}^{N_{2,\mathrm{o}}}}{\Lambda^{3N_\mathrm{t}}(N_{1,\mathrm{o}}+1)!(N_{2,\mathrm{o}}-1)!V_\mathrm{t}} \\ & \exp[-\beta(U_{1,\mathrm{n}}(s_1^{N_1+1,N_{\mathrm{f},1}},\lambda_\mathrm{n})+U_{2,\mathrm{n}}(s_2^{N_2-1,N_{\mathrm{f},2}},1-\lambda_\mathrm{n}))+\eta(\lambda_\mathrm{n})] \end{aligned} \tag{3.32}$$

Since the box where the molecule is to be inserted is chosen at random and the molecule is also inserted randomly, $\alpha(o\to n)=\alpha(n\to o)$. Hence, we obtain,

$$\frac{\mathrm{acc}(\mathrm{o}\to\mathrm{n})}{\mathrm{acc}(\mathrm{n}\to\mathrm{o})}=\frac{p_\mathrm{n}}{p_\mathrm{o}}\frac{\alpha(\mathrm{n}\to\mathrm{o})}{\alpha(\mathrm{o}\to\mathrm{n})} \tag{3.33}$$

$$\begin{aligned} &= \frac{V_{1,\mathrm{o}}^{N_{1,\mathrm{o}}+2}V_{2,\mathrm{o}}^{N_{2,\mathrm{o}}}}{V_{1,\mathrm{o}}^{N_{1,\mathrm{o}}+1}V_{2,\mathrm{o}}^{N_{2,\mathrm{o}}+1}}\frac{N_{1,\mathrm{o}}!N_{2,\mathrm{o}}!}{(N_{1,\mathrm{o}}+1)!(N_{2,\mathrm{o}}-1)!} \\ &\quad\frac{\exp[-\beta(U_{1,\mathrm{n}}(s_1^{N_1+1,N_{\mathrm{f},1}},\lambda_\mathrm{n})+U_{2,\mathrm{n}}(s_2^{N_2-1,N_{\mathrm{f},2}},1-\lambda_\mathrm{n}))+\eta(\lambda_\mathrm{n})]}{\exp[-\beta(U_{1,\mathrm{o}}(s_1^{N_1,N_{\mathrm{f},1}},\lambda_\mathrm{o})+U_{2,\mathrm{o}}(s_2^{N_2,N_{\mathrm{f},2}},1-\lambda_\mathrm{o}))+\eta(\lambda_\mathrm{o})]} \end{aligned} \tag{3.34}$$

The acceptance rules for this particle swap move from box 2 to box 1 is therefore

$$\begin{aligned} \mathrm{acc}(\mathrm{o}\to\mathrm{n})=\min\Bigg(1,\frac{N_{2,\mathrm{o}}}{N_{1,\mathrm{o}}+1}\frac{V_{1,\mathrm{o}}}{V_{2,\mathrm{o}}}\exp[-\beta(U_{1,\mathrm{n}}(s_1^{N_1+1,N_{\mathrm{f},1}},\lambda_\mathrm{n}) \\ +U_{2,\mathrm{n}}(s_2^{N_2-1,N_{\mathrm{f},2}},1-\lambda_\mathrm{n})-U_{1,\mathrm{o}}(s_1^{N_1,N_{\mathrm{f},1}},\lambda_\mathrm{o}) \\ -U_{2,\mathrm{o}}(s_2^{N_2,N_{\mathrm{f},2}},1-\lambda_\mathrm{o}))+\eta(\lambda_\mathrm{n})-\eta(\lambda_\mathrm{o})]\Bigg) \end{aligned} \tag{3.35}$$

Maginn *et al.* [79] have calculated the expanded ensemble bias factors, $\eta(\lambda)$ separately for both boxes 1 ($\eta_1(\lambda)$) and 2 ($\eta_2(\lambda)$) and arrived at the expression for the acceptance rule for the molecule transfer from box 2 to 1,

$$\begin{aligned}\mathrm{acc}(\mathrm{o}\rightarrow\mathrm{n}) = \min\Bigg(1, \frac{N_{2,\mathrm{o}}}{N_{1,\mathrm{o}}+1}\frac{V_{1,\mathrm{o}}}{V_{2,\mathrm{o}}}\exp[-\beta(U_{1,\mathrm{n}}(s_1^{N_1+1,N_{\mathrm{f},1}},\lambda_\mathrm{n}) \\ + U_{2,\mathrm{n}}(s_2^{N_2-1,N_{\mathrm{f},2}},1-\lambda_\mathrm{n}) - U_{1,\mathrm{o}}(s_1^{N_1,N_{\mathrm{f},1}},\lambda_\mathrm{o}) \\ - U_{2,\mathrm{o}}(s_2^{N_2,N_{\mathrm{f},2}},1-\lambda_\mathrm{o})) + \eta_1(\lambda_\mathrm{n}) + \eta_2(\lambda_\mathrm{n}) - \eta_1(\lambda_\mathrm{o}) - \eta_2(\lambda_\mathrm{o})]\Bigg)\end{aligned} \tag{3.36}$$

We can observe that Eqs. (3.35) and Eqs. (3.36) only differ in the inclusion of the expanded ensemble bias factors calculated separately for the two boxes while we calculate it only for one box. Both methods are essentially identical, since the expanded ensemble bias factors depend on $\lambda$ states and they are coupled between the boxes 1 and 2.

For dense systems, the fractional molecule is inserted/deleted randomly from the system. This would be better facilitated if we can insert/delete the fractional molecule using the Configurational-Bias Monte Carlo scheme [53]. Instead of a random insertion of the fractional molecule, we grow the molecule atom by atom. We denote the intramolecular energies (bond-stretching, bond-bending, torsion) by $U^{\mathrm{int}}_{\mathrm{atom},i}$ and the intermolecular energies of the molecule with the surroundings by $U^{\mathrm{ext}}_{\mathrm{atom},i}(\lambda)$. Here $i$ denotes the atom in consideration. We assume the molecule has $l$ atoms. We assume that the molecule is transferred from box 2 to box 1. In box 1, the molecule is grown and in box 2 the molecule is retraced. We denote the state "o" for the old configuration of the molecule in box 2 and state "n" for the new configuration of the molecule in box 1. The procedure for the Configurational-Bias Monte Carlo move for inserting a fractional molecule for a new configuration "n" and $\lambda_n$ is listed below:

1. For the first atom, we generate $k$ random trial positions. The Boltzmann factor of the first atom in trial position $j'$ is given by $\exp[-\beta U^{\mathrm{ext}}_{\mathrm{atom},1}(b_{j'},\lambda_\mathrm{n})]$. One trial configuration is selected from the $k$ trial configurations with the probability

$$p^{\mathrm{ext}}_{\mathrm{atom},1,j'}(b_{j'}) = \frac{\exp[-\beta U^{\mathrm{ext}}_{\mathrm{atom},1}(b_{j'},\lambda_\mathrm{n})]}{\sum_{\hat{j}=1}^{k}\exp[-\beta U^{\mathrm{ext}}_{\mathrm{atom},1}(b_{\hat{j}},\lambda_\mathrm{n})]} \tag{3.37}$$

   The Rosenbluth factor for the first atom is expressed as

$$w_{\mathrm{atom},1}(\mathrm{n}) = \frac{\sum_{\hat{j}=1}^{k}\exp[-\beta U^{\mathrm{ext}}_{\mathrm{atom},1}(b_{\hat{j}},\lambda_\mathrm{n})]}{k} \tag{3.38}$$

2. To insert the next atom $i$, $k$ trial orientations are randomly generated. These $k$ trial orientations are denoted as a set by $\{b\}_k = b_1, b_2, ..., b_k$. The probability of generating a trial orientation $b_j$ is,

$$p^{\text{int}}_{\text{atom},i}(b_j) = \frac{\exp[-\beta U^{\text{int}}_{\text{atom},i}(b_j)]}{\int \exp[-\beta U^{\text{int}}_{\text{atom},i}(b_j)]\text{d}b_j} = \frac{\exp[-\beta U^{\text{int}}_{\text{atom},i}(b_j)]}{C_{\text{atom},i}} \tag{3.39}$$

where $C_{\text{atom},i}$ is the normalization constant.

For all the $k$ trial orientations, we compute the external Boltzmann factors $\exp[-\beta U^{\text{ext}}_i(b_j, \lambda_{\text{n}})]$ and select one trial configuration/orientation denoted by $b_n$ with a probability,

$$p^{\text{ext}}_{\text{atom},i}(b_n) = \frac{\exp[-\beta U^{\text{ext}}_{\text{atom},i}(b_n, \lambda_{\text{n}})]}{\sum_{j=1}^{k} \exp[-\beta U^{\text{ext}}_i(b_j, \lambda_{\text{n}})]} = \frac{\exp[-\beta U^{\text{ext}}_{\text{atom},i}(b_n, \lambda_{\text{n}})]}{w_{\text{atom},i}(n)} \tag{3.40}$$

where the expression for the Rosenbluth factor for the $i$th atom is,

$$w_{\text{atom},i}(n) = \sum_{j=1}^{k} \exp[-\beta U^{\text{ext}}_{\text{atom},i}(b_j, \lambda_{\text{n}})]. \tag{3.41}$$

3. Step 2 is repeated for $l-1$ times until the entire molecule (with $l$ atoms) is grown. The Rosenbluth factor for the entire molecule is expressed as,

$$W(n) = \prod_{i=1}^{l} w_{\text{atom},i}(n) = \sum_{j=1}^{k} \exp[-\beta U^{\text{ext}}_{\text{atom},i}(b_j, \lambda_{\text{n}})] \tag{3.42}$$

To calculate the Rosenbluth factor of the old configuration "o" in box 2, we have the following steps. Recall that for box 2, the coupling factor is $1-\lambda_{\text{o}}$ in the old configuration (and $1-\lambda_{\text{n}}$ in the new configuration)

1. The fractional particle is selected.

2. $k-1$ trial positions are generated. The energy and the Rosenbluth factor of the first atom for the $k-1$ trial positions and the existing position of the first atom is determined by,

$$w_{\text{atom},1}(o) = \frac{\sum_{j'}^{k} \exp[-\beta U^{\text{ext}}_{\text{atom},1}(b_1, 1-\lambda_{\text{o}})]}{k} \tag{3.43}$$

3. To determine the Rosenbluth factor for the other $l-1$ atoms, we generate $k-1$ trial positions. These $k-1$ trial positions along with the existing position of the $i$th atom of the fractional molecule will determine the set of $k$ trial positions

$\{b'\}_k = b'_1, b'_2, ..., b'_k$. The equation for the Rosenbluth factor for the $i$th atom is,

$$w_{\text{atom},i}(o) = \sum_{j=1}^{k} \exp[-\beta U^{\text{ext}}_{\text{atom},i}(b'_j, 1-\lambda_{\text{o}})]. \tag{3.44}$$

4. Repeat the above step for all the $l$ atoms. The Rosenbluth factor for the entire molecule is

$$W(o) = \prod_{i=1}^{l} w_{\text{atom},i}(o) \tag{3.45}$$

For the insertion of the fractional molecule using CBMC in box 1, the probability of generating the chain of $l$ atoms with a certain configuration "n", $\alpha(o \to n)$, is the product of generating a trial configuration ($p^{\text{bond}}_{\text{atom},i}(n)$) and the probability of selecting that particular configuration ($p^{\text{ext}}_{\text{atom},i}(n)$) for all the $l$ atoms in the molecule. The probability of generating a new configuration "n" for a molecule with $l$ atoms is

$$\alpha(o \to n) = \prod_{i=1}^{l} p_{\text{atom},i}(o \to n) \tag{3.46}$$

$$= \prod_{i=1}^{l} p^{\text{bond}}_{\text{atom},i}(n) p^{\text{ext}}_{\text{atom},i}(n) \tag{3.47}$$

Similarly, the expression for the probability of generating the old configuration "o" is

$$\alpha(n \to o) = \prod_{i=1}^{l} p_{\text{atom},i}(n \to o) \tag{3.48}$$

$$= \prod_{i=1}^{l} p^{\text{bond}}_{\text{atom},i}(o) p^{\text{ext}}_{\text{atom},i}(o) \tag{3.49}$$

A given set of $k$ trial orientations generated for the insertion, which includes the orientation "n", is denoted by $(b_n, b^*)$. The term $(b_o, b'^*)$ is the given set of additionally generated trial orientations around the old orientation "o". The probability of generating the combined set of orientations $(b^*, b'^*)$ is given by $P^{\text{bond}}(b^*, b'^*)$. From Eqs. (3.39), (3.40), (3.41) and (3.47), we find that the probability of generating the new configuration "n" is expressed as

$$\alpha(o \to n, b^*, b'^*) = \prod_{i=1}^{l} \left( \frac{\exp[-\beta U^{\text{int}}_{\text{atom},i}(b_j)]}{C_{\text{atom},i}} \frac{\exp[-\beta U^{\text{ext}}_{\text{atom},i}(b_n, \lambda_{\text{n}})]}{w_{\text{atom},i}(n)} P^{\text{bond}}(b^*, b'^*) \right) \tag{3.50}$$

We know that $\prod_{i=1}^{l} \exp[-\beta U^{\text{ext}}_{\text{atom},i}(b_n, \lambda_\text{n})] = U^{\text{ext}}_{1,\text{frac}}(s_1^{N_1+1,N_{\text{f},1}}, \lambda_\text{n})$. Substituting this expression and Eq. (3.42) in Eq. (3.50), we have,

$$\alpha(o \to n, b^*, b'^*) = \frac{\exp[-\beta(U^{\text{ext}}_{1,\text{frac}}(s_1^{N_1+1,N_{\text{f},1}}, \lambda_\text{n}))]}{W(n)} \prod_{i=1}^{l} \left( \frac{\exp[-\beta U^{\text{int}}_{\text{atom},i}(b_j)]}{C} P^{\text{bond}}(b^*, b'^*) \right) \tag{3.51}$$



where $C$ is the total normalization constant for all the atoms given by $C = \prod_{i=0}^{l-1} C_{\text{atom},i}$. The probability to generate the old configuration "o" is,

$$\alpha(n \to o, b'^*, b^*) = \prod_{i=1}^{l} \left( \frac{\exp[-\beta U^{\text{int}}_{\text{atom},i}(b_j^*)]}{C_{\text{atom},i}} \frac{\exp[-\beta U^{\text{ext}}_{\text{atom},i}(b_o, 1-\lambda_\text{o})]}{w_{\text{atom},i}(o)} P^{\text{bond}}(b^*, b'^*) \right). \tag{3.52}$$

We know that $\prod_{i=1}^{l} \exp[-\beta U^{\text{ext}}_{\text{atom},i}(b_o, 1-\lambda_\text{o})] = \exp[-\beta(U^{\text{ext}}_{2,\text{frac}}(s_2^{N_2,N_{\text{f},2}}, 1-\lambda_\text{o}))]$. Thus we have,

$$\alpha(n \to o, b'^*, b^*) = \frac{\exp[-\beta(U^{\text{ext}}_{2,\text{frac}}(s_2^{N_2,N_{\text{f},2}}, 1-\lambda_\text{o}))]}{W(o)} \prod_{i=1}^{l} \left( \frac{\exp[-\beta U^{\text{int}}_{\text{atom},i}(b_j^*)]}{C} P^{\text{bond}}(b^*, b'^*) \right). \tag{3.53}$$

Detailed balance states that the probabilities of generating all possible configurations for both states "o" and "n" must be the same. We impose super detailed balance, which states that for a particular set of trial orientations $(b^*, b'^*)$, detailed balance must hold [53]. This is expressed as,

$$\begin{aligned} p_\text{o} \cdot \alpha(o \to n, b^*, b'^*) \cdot \text{acc}(o \to n, b^*, b'^*) = \\ p_\text{n} \cdot \alpha(n \to o, b'^*, b^*) \cdot \text{acc}(n \to o, b'^*, b^*) \end{aligned} \tag{3.54}$$

Rearranging, we obtain,

$$\frac{\text{acc}(o \to n, b^*, b'^*)}{\text{acc}(n \to o, b'^*, b^*)} = \frac{p_\text{n}}{p_\text{o}} \frac{\alpha(n \to o, b'^*, b^*)}{\alpha(o \to n, b^*, b'^*)} \tag{3.55}$$

The probabilities of existing in the old and the new states can be expressed as

$$\begin{aligned}\frac{p_{\rm n}}{p_{\rm o}} = \exp[ &- \beta(U_{1,{\rm n}}(s_1^{N_1+1,N_{{\rm f},1}},\lambda_{\rm n}) + U_{2,{\rm n}}(s_2^{N_2-1,N_{{\rm f},2}},1-\lambda_{\rm n}) \\ &- U_{1,{\rm o}}(s_1^{N_1,N_{{\rm f},1}},\lambda_{\rm o}) + U_{2,{\rm o}}(s_2^{N_2,N_{{\rm f},2}},1-\lambda_{\rm o})] \\ &\cdot \frac{N_{2,{\rm o}}}{N_{1,{\rm o}}+1}\frac{V_{1,{\rm o}}}{V_{2,{\rm o}}}\exp[\eta(\lambda_{\rm n})-\eta(\lambda_{\rm o})] \end{aligned} \tag{3.56}$$

3

According to the MC move, in box 1 where the molecule is inserted, the new configuration includes the energy for converting the existing fractional molecule into a whole molecule $U_{1,{\rm frac}\to{\rm whole}}(s_1^{N_1,N_{{\rm f},1}},\lambda_{\rm o})$ and the energy for inserting a new fractional molecule $U^{\rm ext}_{1,{\rm frac}}(s_1^{N_1+1,N_{{\rm f},1}},\lambda_{\rm n})$. We can write

$$\begin{aligned}U_{1,{\rm n}}(s_1^{N_1+1,N_{{\rm f},1}},\lambda_{\rm n}) =& U_{1,{\rm o}}(s_1^{N_1,N_{{\rm f},1}},\lambda_{\rm o}) + U_{1,{\rm frac}\to{\rm whole}}(s_1^{N_1,N_{{\rm f},1}},\lambda_{\rm o}) \\ &+ U^{\rm ext}_{1,{\rm frac}}(s_1^{N_1+1,N_{{\rm f},1}},\lambda_{\rm n}).\end{aligned} \tag{3.57}$$

Likewise, in box 2 where the molecule is deleted, the new configuration includes the energy for deleting the existing fractional molecule $U^{\rm ext}_{2,{\rm frac}}(s_2^{N_2,N_{{\rm f},2}},1-\lambda_{\rm o})$ and the energy for converting a whole molecule into a fractional molecule $U_{2,{\rm whole}\to{\rm frac}}(s_2^{N_2-1,N_{{\rm f},2}},1-\lambda_{\rm n})$.

$$\begin{aligned}U_{2,{\rm n}}(s_2^{N_2-1,N_{{\rm f},2}},1-\lambda_{\rm n}) =& U_{2,{\rm o}}(s_2^{N_2,N_{{\rm f},2}},1-\lambda_{\rm o}) - U^{\rm ext}_{2,{\rm frac}}(s_2^{N_2,N_{{\rm f},2}},1-\lambda_{\rm o}) \\ &- U_{2,{\rm whole}\to{\rm frac}}(s_2^{N_2-1,N_{{\rm f},2}},1-\lambda_{\rm n}).\end{aligned} \tag{3.58}$$

Including these expressions in Eq. (3.56), we obtain,

$$\begin{aligned}\frac{p_{\rm n}}{p_{\rm o}} =& \frac{N_{2,{\rm o}}}{N_{1,{\rm o}}+1}\frac{V_{1,{\rm o}}}{V_{2,{\rm o}}}\exp\Bigg[ - \beta(U_{1,{\rm frac}\to{\rm whole}}(s_1^{N_1,N_{{\rm f},1}},\lambda_{\rm o}) \\ &- U_{2,{\rm whole}\to{\rm frac}}(s_2^{N_2-1,N_{{\rm f},2}},1-\lambda_{\rm n}) + U^{\rm ext}_{1,{\rm frac}}(s_1^{N_1+1,N_{{\rm f},1}},\lambda_{\rm n}) \\ &- U^{\rm ext}_{2,{\rm frac}}(s_2^{N_2,N_{{\rm f},2}},1-\lambda_{\rm o}))\Bigg]\exp[\eta(\lambda_{\rm n})-\eta(\lambda_{\rm o})]\end{aligned} \tag{3.59}$$

Substituting Eqs. (3.59), (3.51), (3.53) in Eq. (3.55), we have,

$$\begin{aligned}\frac{\mathrm{acc}(o \to n, b^*, b'^*)}{\mathrm{acc}(n \to o, b'^*, b^*)} =& \frac{N_{2,\mathrm{o}}}{N_{1,\mathrm{o}}+1}\frac{V_{1,\mathrm{o}}}{V_{2,\mathrm{o}}} \exp\Big[-\beta(U_{1,\mathrm{frac}\to\mathrm{whole}}(s_1^{N_1,N_{\mathrm{f},1}}, \lambda_\mathrm{o}) \\ & - U_{2,\mathrm{whole}\to\mathrm{frac}}(s_2^{N_2-1,N_{\mathrm{f},2}}, 1-\lambda_\mathrm{n}) + U^{\mathrm{ext}}_{1,\mathrm{frac}}(s_1^{N_1+1,N_{\mathrm{f},1}}, \lambda_\mathrm{n}) \\ & - U^{\mathrm{ext}}_{2,\mathrm{frac}}(s_2^{N_2,N_{\mathrm{f},2}}, 1-\lambda_\mathrm{o}))\Big] \exp[\eta(\lambda_\mathrm{n}) - \eta(\lambda_\mathrm{o})] \\ & \frac{\exp[-\beta(U^{\mathrm{ext}}_{2,\mathrm{frac}}(s_2^{N_2,N_{\mathrm{f},2}}, 1-\lambda_\mathrm{o}))]}{W(o)} \\ & \prod_{i=1}^{l}\left(\frac{\exp[-\beta U^{\mathrm{int}}_{\mathrm{atom},i}(b_j^*)]}{C} P^{\mathrm{bond}}(b^*, b'^*)\right) \\ & \frac{W(n)}{\exp[-\beta(U^{\mathrm{ext}}_{1,\mathrm{frac}}(s_1^{N_1+1,N_{\mathrm{f},1}}, \lambda_\mathrm{n}))]} \\ & \prod_{i=1}^{l}\left(\frac{C}{\exp[-\beta U^{\mathrm{int}}_{\mathrm{atom},i}(b_j)] P^{\mathrm{bond}}(b^*, b'^*)}\right) \qquad (3.60) \\ =& \frac{N_{2,\mathrm{o}}}{N_{1,\mathrm{o}}+1}\frac{V_{1,\mathrm{o}}}{V_{2,\mathrm{o}}}\frac{W(n)}{W(o)} \exp[-\beta(U_{1,\mathrm{frac}\to\mathrm{whole}}(s_1^{N_1,N_{\mathrm{f},1}}, \lambda_\mathrm{o}) \\ & - U_{2,\mathrm{whole}\to\mathrm{frac}}(s_2^{N_2-1,N_{\mathrm{f},2}}, 1-\lambda_\mathrm{n})) + (\eta(\lambda_\mathrm{n}) - \eta(\lambda_\mathrm{o}))] \qquad (3.61)\end{aligned}$$

Therefore, the acceptance rule for the CB/CFCMC for the particle swap from box 2 to box 1 is,

$$\begin{aligned}\mathrm{acc}(\mathrm{o} \to \mathrm{n}, b^*, b'^*) = \min\Bigg(1, & \frac{N_{2,\mathrm{o}}}{N_{1,\mathrm{o}}+1}\frac{V_{1,\mathrm{o}}}{V_{2,\mathrm{o}}}\frac{W(n)}{W(o)} \exp[-\beta(U_{1,\mathrm{frac}\to\mathrm{whole}}(s_1^{N_1,N_{\mathrm{f},1}}, \lambda_\mathrm{o}) \\ & - U_{2,\mathrm{whole}\to\mathrm{frac}}(s_2^{N_2-1,N_{\mathrm{f},2}}, \lambda_\mathrm{n})) + (\eta(\lambda_\mathrm{n}) - \eta(\lambda_\mathrm{o}))]\Bigg) \qquad (3.62)\end{aligned}$$

We can follow the same procedure for a particle swap from box 1 to box 2. From the above, we can see that CB/CFCMC obeys detailed balance and it is possible to carry out such a Monte Carlo move. One can easily see that for $k = 1$ (only one trial direction) the acceptance rule for particle exchange reduces to the conventional one for CFCMC in the Gibbs ensemble.

Application to the grand-canonical ensemble is straightforward and can be effected by taking one of the simulation boxes as an infinitely large reservoir of non-interacting chain molecules. From the above derivation, we can show that the $\exp[-\beta\Delta U]$ term in Eqs. (3.11), (3.12) should be replaced by $\frac{W(n)}{W^{IG}}$ for insertion and by $\frac{W^{IG}}{W(o)}$ for deletion [77, 78].

The procedure for insertion/deletion attempts in the grand-canonical ensemble is

- Insertion, $\lambda_{\mathrm{n}} = 1 + \epsilon$
  1. The fractional molecule with $\lambda = \lambda_{\mathrm{o}}$ is made integer ($\lambda = 1$) and the energy difference $\Delta U$ is computed. This part of the CB/CFCMC move is unbiased.
  2. A new fractional molecule with $\lambda_{\mathrm{n}} = \epsilon$ is grown using CBMC giving $W(n)$. This part of the CB/CFCMC is biased since CBMC is used.
  3. Acceptance rule:
     $p_{\mathrm{acc}} = \min\left(1, \frac{f\beta V}{N+1} \frac{W(n)}{\langle W^{\mathrm{IG}} \rangle} \exp[-\beta \Delta U] \exp[\eta\,(\lambda_{\mathrm{n}}) - \eta\,(\lambda_{\mathrm{o}})]\right)$
- Deletion, $\lambda_{\mathrm{n}} = -\epsilon$
  1. The existing fractional particle is retraced using CBMC with $\lambda = \lambda_{\mathrm{o}}$ giving $W(o)$ and the fractional molecule is subsequently removed. This part of the CB/CFCMC is biased since CBMC is used
  2. A new fractional molecule is randomly chosen with $\lambda_{\mathrm{n}} = 1 - \epsilon$ and the energy difference $\Delta U$ is computed. This part of the CB/CFCMC move is unbiased.
  3. Acceptance rule:
     $p_{\mathrm{acc}} = \min\left(1, \frac{N}{f\beta V} \frac{\langle W^{\mathrm{IG}} \rangle}{W(o)} \exp[-\beta \Delta U] \exp[\eta\,(\lambda_{\mathrm{n}}) - \eta\,(\lambda_{\mathrm{o}})]\right)$

We tested CB/CFCMC method by computing the single component and mixture adsorption isotherms of hexane isomers in $Fe_2(BDP)_3$ at 433 K. The isotherms computed using CB/CFCMC, CBMC and CFCMC are equivalent within statistical error.

## 3.3 Results

### 3.3.1. Alkanes in $Fe_2(BDP)_3$

The separation of linear, mono-branched, and di-branched isomers of alkanes is of significant importance in the petrochemical industry. This separation can be achieved by selective adsorption in ordered crystalline nanoporous materials such as zeolites, MOFs, COFs, and ZIFs by exploiting subtle differences in molecular configurations [147, 148]. The alkane separation efficiency is generally described by the molecule-wall effective distance [149]. Small pore structures like ZIF-77, MFI, and $Fe_2(BDP)_3$ [150] can show very large selectivities, but have a relatively small pore volume. This class of systems generally favor the adsorption of the linear alkanes. Slightly larger pores show an opposite hierarchy with the dibranched molecules fitting best (*e.g.* UiO-66), while even larger pores revert back to having the linear alkane adsorb best, albeit with much lower selectivities than the small-pore structures.

In Fig. 3.1, we show isotherms of hexane isomers in $Fe_2(BDP)_3$ computed by CBMC, CFCMC and CB/CFCMC at 433 K. $Fe_2(BDP)_3$ is a highly stable framework with 1-dimensional triangular channels made of iron and benzene-1,4-dicarboxylic acid (BDP). The crystal data was taken from Ref. [150] and we used $5 \times 1 \times 1$ unit cells with periodic boundaries. The framework is modeled using the DREIDING force field [151], and atoms not defined in the DREIDING model are taken from the UFF [152]. The alkanes are modeled using the Transferable potentials for Phase Equilibria (TraPPE) force field by Martin and Siepmann [62, 63]. Despite the fact that the model lumps $CH_3$, $CH_2$, and CH into single interaction centers, it very accurately reproduces the experimental phase diagram and critical points. Cross interactions are mixed using Lorentz-Berthelot mixing rule [153, 154].



For both single components as well as the 5-component mixture, we find excellent agreement between the CFCMC, CB/CFCMC and the CBMC method. The simulations have been run the same number of cycles (where a cycle consist of $N$ Monte Carlo moves, $N$ the number of molecules present in the system with a minimum of 20 moves), and roughly for the same amount of CPU time. We note that for CB/CFCMC and CFCMC the error bars become larger in regions where the isotherms are more steep (however, note the average matches CBMC very well with CB/CFCMC and CFCMC). This is an indication that CB/CFCMC and the CFCMC is able to explore more phase-space than CBMC. Also note that CB/CFCMC and CFCMC matches CBMC even for loadings that are very small. It is the integer number of molecules that is the relevant property and the fractional molecule should be excluded in the analysis. Our simulations agree both qualitatively and quantitatively with the CBMC simulations of Ref. [150], further supporting the correctness of the simulation results. From our simulations we observe that, for these flexible molecules with internal degrees of freedom, the CB/CFCMC and CFCMC are just as efficient as CBMC.

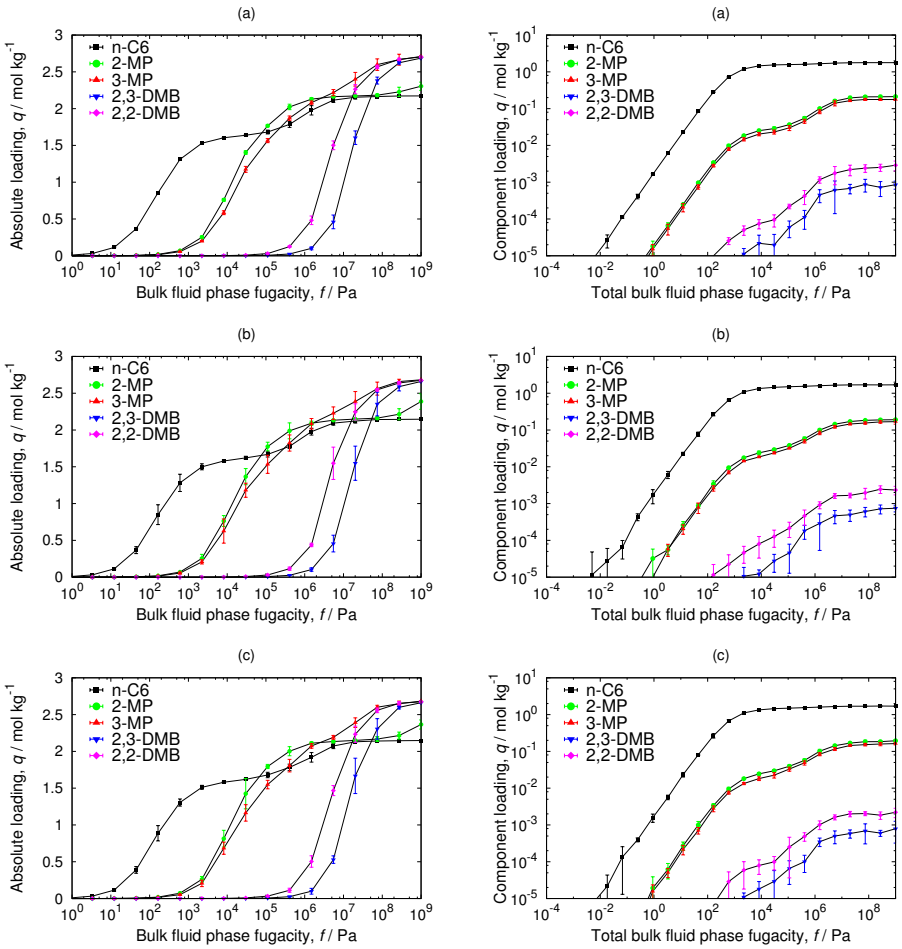


Figure 3.1: Adsorption isotherms calculated using (a) CBMC, (b) CFCMC and (c) CB/CFCMC of hexane isomers in $Fe_2BDP_3$ at 433K. Left column corresponds to the single component isotherms and right column to the 5-component mixture (hexane=n-C6, 2-methylpentane=2-MP, 3-methylpentane=3-MP, 2,2-dimethylbutane= 2,2DMB and 2,3-dimethylbutane=2,3DMB). Both single component and mixture isotherms are equivalent for the three methods.

Table 3.1: The vapor-liquid coexistence densities for Lennard-Jones chains of length *m=8* computed using CBMC, CFCMC, CB/CFCMC algorithms. The simulations were done with 500.000 cycles and 100.000 initialization/equilibration cycles. The number of Monte Carlo moves per Monte Carlo cycle is equal to the total number of particles with a minimum of 20. The errors are calculated as standard deviations of the block averages. Reduced units were used to compare with literature.

| Lennard-Jones chain length $m = 8$ | | | |
|---|---|---|---|
| Method | $T^*$ | $\langle\rho_1^*\rangle$ | $\langle\rho_2^*\rangle$ |
| Literature [120] | 1.887 | 0.033 ±0.005 | 0.521±0.006 |
| | 1.923 | 0.031±0.005 | 0.506±0.005 |
| | 1.980 | 0.058±0.004 | 0.453±0.005 |
| CBMC | 1.887 | 0.034±0.005 | 0.519±0.009 |
| | 1.923 | 0.043±0.005 | 0.494±0.009 |
| | 1.980 | 0.060±0.006 | 0.430±0.021 |
| CFCMC | 1.887 | 0.034±0.005 | 0.514±0.009 |
| | 1.923 | 0.038±0.005 | 0.484±0.009 |
| | 1.980 | 0.063±0.024 | 0.43±0.034 |
| CB/CFCMC | 1.887 | 0.029±0.003 | 0.510±0.007 |
| | 1.923 | 0.038±0.008 | 0.478±0.012 |
| | 1.980 | 0.073±0.019 | 0.433±0.020 |



### 3.3.2. Lennard-Jones Chains in the Gibbs Ensemble

To test the Continuous Fractional Monte Carlo combined with the Configurational-Bias MC algorithm, we computed the coexistence densities for Lennard-Jones chains of length $m = 8$ and octane using three different algorithms: CBMC, CFCMC, and CB/CFCMC in the Gibbs Ensemble. For the algorithms with CBMC, simulations were performed with 10 trial positions. The results for the coexistence densities ($\langle\rho_1\rangle$ and $\langle\rho_2\rangle$) are shown in Tables 3.1 and 3.2. For the Lennard-Jones 8-mers, the results are presented in reduced units to compare with the literature. They are in good agreement with each other and with the results reported by Ref. [120]. For the octanes, our results are in good agreement with each other and equivalent within the error bar to the results reported by Ref. [62].

The gas phase density value at $T^*$=1.923 of Mooij *et al.* [120] differs from our value. However this density is lower than the density at $T^*$=1.887 which seems inconsistent. Our data points have been run 10 times longer. Considering this difference, the data agree well. However, this raises a discussion on the magnitude of error bars. Our error bars are computed by dividing the simulation in five blocks and computing the error from the standard deviation of the averages of these five blocks. We report a 95% confidence interval. In Gibbs simulations the density fluctuates as the volume and the number of particles fluctuate individually. The magnitude of the fluctuations are the most sensitive to the frequency and magnitude of the volume move. Longer simulations times provide a better estimate of the "true" average but also an increased contribution to the error from exploring a larger region of phase space. In order to evaluate this "hidden" error, it is advisable to plot the density vs temperature of the full VLE curve and check the smoothness and continuity of

Table 3.2: The vapor-liquid coexistence densities for octane using the TraPPE model computed with CBMC, CFCMC, CB/CFCMC algorithms. The simulations were run with 50000 initialization cycles and 500000 cycles. The errors are calculated as standard deviations of the ensemble averages. The results are equivalent within the error bar to the results of Martin and Siepmann [62].

| Octane, TraPPE force field. | | | |
|---|---|---|---|
| Method | Temperature[K] | $\langle\rho_1\rangle$[kg/m$^3$] | $\langle\rho_2\rangle$[kg/m$^3$] |
| Literature [62] | 390 | 3.9±0.5 | 624±2 |
| | 440 | 12.9±0.6 | 574±1 |
| | 490 | 28.0±4.0 | 505±4 |
| | 515 | 54.0±6.0 | 473±5 |
| | 540 | 78±17 | 425±14 |
| CBMC | 390 | 4.2±0.3 | 629.1±1.7 |
| | 440 | 13.2±0.45 | 578.5±1.4 |
| | 490 | 36.3±1.7 | 521.5±2.2 |
| | 515 | 59.9±2.0 | 485.9±0.7 |
| | 540 | 102.1±20.0 | 420.9±20.60 |
| CFCMC | 390 | 4.2±0.6 | 625.0±1.6 |
| | 440 | 13.9±1.0 | 575.0±3.8 |
| | 490 | 37.7±4.4 | 512.2±4.2 |
| | 515 | 63.2±7.3 | 477.0±3.5 |
| | 540 | 78.6±7.7 | 426.6±14.7 |
| CB/CFCMC | 390 | 3.6±0.5 | 626.5±2.2 |
| | 440 | 12.2±1.0 | 575.0±1.0 |
| | 490 | 31.1±4.6 | 512.6±2.9 |
| | 515 | 48.9±1.8 | 471.8±5.5 |
| | 540 | 83.7±14.1 | 424.0±14.3 |

the vapor liquid equilibrium curve. This would also reveal that the $T^*$=1.923 data point of Mooij *et al.* [120] can be considered an outlier.

The gas and liquid branch are well separated by a free energy barrier at low temperatures. At high temperature the barrier becomes low, which makes Gibbs difficult to apply at these temperatures. This manifests itself as swapping between the liquid and gas boxes. This must be avoided to accurately compute the gas and liquid densities separately.

The performance and efficiency of the CB/CFCMC algorithm in the Gibbs Ensemble can be assessed by computing the number of accepted particle exchanges between the boxes per Monte Carlo cycles performed and also the number of accepted particle exchanges between the boxes per total CPU time for the different algorithms. Trial moves are chosen with the following probabilities: Gibbs-volume 0.2%, translation 19.96 %, rotation 19.96 %, reinsertion 19.96 %, partial reinsertion 19.96 % and Gibbs swap 19.96 %. For the CFCMC and CB/CFCMC, the number of accepted particle exchanges are defined as the total number of accepted moves in $\lambda$ that result in particle exchanges between the boxes. The measured time is the

time of just the Gibbs insertion/deletion move for an insertion. The clock-routine was used which measured only CPU time. We ran on a 12-core machine using 10 jobs simultaneously (and with 2 cores free for system tasks) to make sure none of them can make use of the cache (or at least all used the same cache). The results for the number of accepted particle exchanges per MC cycle and per CPU Time for the different algorithms for Lennard-Jones chains with chain length = 8 are presented in Fig. 3.2. We can observe that, as expected, that amount of accepted exchanges per MC cycle for both CBMC and CB/CFCMC increases with the number of trial positions. CB/CFCMC increases significantly the amount of acceptance percentage with respect to CBMC. In CBMC the efficiency as a function of the number of trial directions has not a pronounced maximum but rather a broad plateau while for CB/CFCMC there is a pronounced maximum at only a few trial directions . The acceptance probability cannot exceed 50% because of the choice of $\Delta\lambda$, so that having more trial directions (than the optimum) results in a decrease in acceptance. Note that we fixed $\lambda_{\max} = 0.332$ and fixed the biasing factors for all runs.

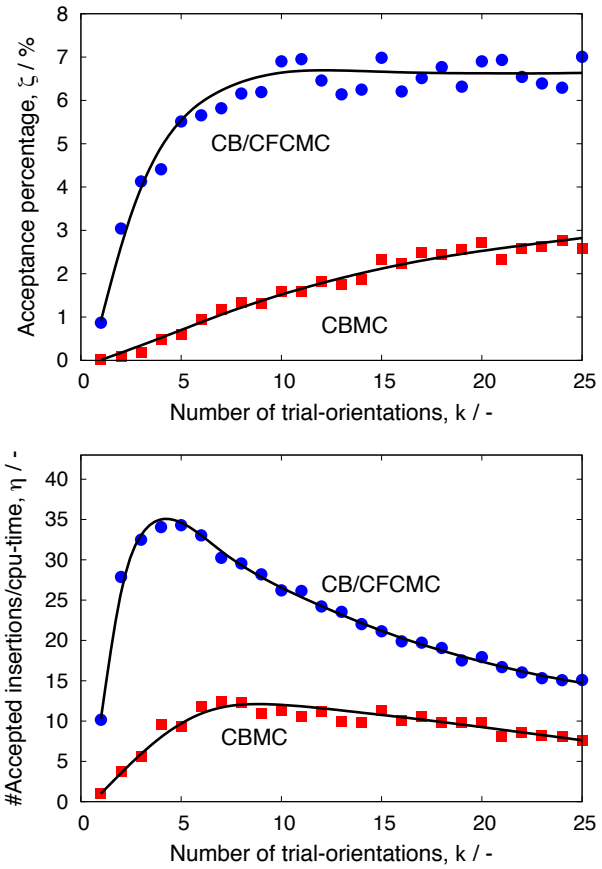


Figure 3.2: The efficiencies for CBMC, CFCMC, CB/CFCMC algorithms for Lennard-Jones chains in the Gibbs Ensemble with chain length = 8. Total number of chain molecules $N = 200$, temperature $T^* = 1.887$, total volume $V_t^* = 3456$. The number of MC production cycles equals 50000.

## 3.4 Conclusions

The efficiency of insertion, depends on the density of the system. At low densities and for a fixed number of Monte Carlo cycles, CBMC is more efficient, since the attempts of insertion are more frequent, no diffusion in $\lambda$-space is needed. At medium densities, the efficiency of insertion can be summarized by CB/CFCMC > CFCMC > CBMC > MC. Methods using CFCMC really shine, since they are rather insensitive to meta-stable states because of the $\lambda$ biasing. A molecular structure or packing can be broken down if the $\lambda$-histogram is relatively flat. This requires an equilibration period during which the $\lambda$-biasing is iteratively setup using *e.g.* Wang-Landau sampling but in our experience this does not require *longer* equilibration. After a simulation the $\lambda$-histogram can be examined. If it relatively flat then block-averages are an indication of equilibration. In contrast, CBMC can show a small error bar, no drift in block averages, but still being unconverged.



In addition, CB/CFCMC has a clear advantage for long chain molecules, since it avoids having to generate ideal gas configurations for the CFCMC insertions. Although this generation might be cheap, for increasing chain lengths the molecular configurations inside the host framework increasingly deviate from their ideal gas configuration. The CFCMC would fail here, while the CB/CFCMC could still work by growing the molecule atom by atom. However, also the CB/CFCMC and CFCMC are not applicable around saturation conditions. For relatively large pores systems the fluid inside the pores can be compressed further and further with no bounds (in practice, the bound is the maximum pressure the experimental equipment can handle and/or the the nanoporous material remains stable), but for small pores and relatively bulky molecules (using hard potentials) the saturation can be an *integer* number of molecules. A typical example is a xylene in UiO-66 or an heptane molecule in ERI-type zeolite. There fits only one heptane molecule in an ERI-type cage at reasonable pressures. For these cases it is impossible to insert an additional molecule at saturation conditions, and similarly, at saturation it is energetically highly unfavorable to delete a molecule. In this case however, for single components the loading is known, and for mixtures it is the ratio of components that is of interest. This ratio is better sampled using MC moves like identity-switches, or methods like replica exchange in temperature or mole fraction. Alternatively, especially when simulating flexible hosts, sampling efficiency can be increased by combining the insertion/deletion schemes with the MD methodology.

# 4

# Simulating the Reactions of $CO_2$ in Aqueous Monoethanolamine Solutions

This chapter is based on the following publication: S.P. Balaji, S. Gangarapu, M. Ramdin, A. Torres-Knoop, H. Zuilhof, E.L.V. Goetheer, D. Dubbeldam, T.J.H. Vlugt, *Simulating the reactions of $CO_2$ in aqueous monoethanolamine solution by Reaction Ensemble Monte Carlo using the Continuous Fractional Component method*, J. Chem. Theory Comput. **2015**, 11, 2661-2669 [69]

## 4.1 Introduction

Carbon dioxide ($CO_2$) is the most important greenhouse gas present in combustion flue gases. It accounts for an abundant portion of the emitted greenhouse gases [155, 156]. The capture of $CO_2$ from flue gases, its transport, and storage has been identified to be of crucial importance to reduce the carbon footprint in the atmosphere [157]. Post-combustion $CO_2$ capture processes are particularly important for power plants operating on fossil fuels like coal, natural gas, etc., as they contribute approximately around 25% of the global $CO_2$ emissions [25, 158]. Scientific progress has contributed to the rapid growth of industries and this has increased the demand for energy drastically. This translates to an increased dependency on fossil fuels, since alternate energy sources have not yet been fully developed [11]. To reduce $CO_2$ emissions into the atmosphere, it is necessary to capture $CO_2$ from the flue gas streams. Typically, the removal of $CO_2$ from flue gas streams is carried out using liquid amine solvents [159]. Monoethanolamine-containing (MEA) solutions were among the first alkanolamine based solvents used in the capture of $CO_2$. This system remains one of the most important solvents in the post-combustion $CO_2$ capture [31]. Some of the advantages of using MEA solutions for $CO_2$ capture are the high $CO_2$ absorption capacity and reaction rates and low cost of solvent [11, 31]. In order to regenerate the solvent back, heat must be supplied [11, 31, 160]. Some of the disadvantages of using the MEA solution as solvents include the high energy demand to regenerate the solvent and emissions of MEA solvents as aerosol [161, 162]. MEA solutions are also susceptible to oxidative and thermal degradation [161–163].

The mechanism of $CO_2$ absorption in MEA solutions is chemical in nature. $CO_2$ reacts with the MEA solution forming stable carbamates [31, 71, 159, 160, 164]. To study the chemisorption of $CO_2$ in MEA solutions and to reduce the heat required to regenerate the alkanolamine after $CO_2$ capture, it is necessary to study the chemical reactions that take place in the solution [164]. There are several possible mechanisms explaining how $CO_2$ reacts with alkanolamines [18, 160, 164, 165]. $CO_2$ reacts through an acid-base buffer mechanism with the alkanolamines to form protonated amines. $CO_2$ also reacts with some primary and secondary alkanolamines to form carbamates and reacts with tertiary alkanolamines to form bicarbonates [18, 160, 164]. To design a $CO_2$ amine treating process, it is important to understand the chemical equilibrium as well as the kinetics of the different reactions. There are many studies in the literature about the $CO_2$-MEA system [8, 159, 161, 166]. Sartori and Savage obtained the equilibrium constants for carbamate formation [35]. Batt *et al.* [34] and Maddox *et al.* [27] qualitatively investigated the reactions occurring in the MEA system. Poplsteinova *et al.* [167] have studied systems containing MEA and N-methyl-diethanolamine using NMR spectroscopy. Hasse and co-workers [160] have studied the chemical equilibria of $CO_2$ in aqueous alkanolamines using online NMR spectroscopy. Chemical equilibria and kinetics of $CO_2$-alkanolamine solutions are difficult to study experimentally at a molecular level because of the extremely fast reaction rates and the different reaction mechanisms.

Molecular simulations play an important role in bridging the gap between our understanding of the reaction phenomena on a molecular level and the experimental observations on a macroscopic scale [53]. The impact of individual reactions and

reaction mechanisms on the chemical equilibrium of the system can be studied using molecular simulations. Quantum chemical methods are widely applied to compute stationary points on the potential energy surface like transition states and activation barriers. Time dependent ab-initio methods like Car-Parrinello Molecular Dynamics [168] can be used to model the reactions directly. These methods scale poorly with system size and are sometimes difficult to apply to liquid phases. A classical based approach developed by Van Duin *et al.* uses "Reactive" force fields (ReaxFF) that are parameterized to study the chemical reactions of a few systems using classical Molecular Dynamics simulations [169]. ReaxFF treats the intermolecular interactions between the atoms and molecules through a classical force field which have been parameterized from experimental data or quantum simulations [169]. Another classical based approach called the Reaction Ensemble Monte Carlo (RxMC) for studying chemical reactions in equilibrium ignores transient events like bond breaking and formation (reaction mechanism in general). This approach is ideal to study the equilibrium distributions of the reacting species, since the effect of the intermolecular interactions with the surrounding molecules are taken into account. It is important to realize that equilibrium speciation is determined by thermodynamics of the system, and classical molecular simulations are a suitable tool to study this. The Reaction Ensemble Monte Carlo (RxMC) was developed independently by Johnson *et al.* [66] and Smith and Triska [170]. An important feature of Reaction Ensemble Monte Carlo (RxMC) is the actual reaction and its transition path is not simulated, but that only the equilibrium configurations of the molecules before and after the reaction are sampled. The forward and backward reactions are sampled using stochastic trial moves. In case of a forward reaction, the reactant molecules are chosen at random and are deleted from the simulation box while the product molecules are inserted randomly according to the stoichiometry of the reaction. This RxMC method requires the input of stoichiometric coefficients of the reactants and products and the ideal gas partition functions of isolated reactant and product molecules along with the intermolecular potential parameters to describe the interactions between the molecules. These ideal gas partition functions of isolated molecules can be obtained from thermophysical tables or quantum mechanical calculations [67, 68, 81]. The partition function of ideal gas molecules depend on the volume of the simulation box and this must be taken into account in the acceptance rules of the RxMC algorithm.

Previous research pertaining to RxMC has focused on small molecules with fixed internal degrees of freedom [66, 80, 170–173]. Lisal and co-workers [174, 175] have developed the Reaction Ensemble Monte Carlo for systems with flexible internal degrees of freedom to study the synthesis of Methyl-*tert*-butyl-ether (MTBE) from isobutene and methanol. The acceptance rules for the reaction move derived by Lisal and co-workers also include the change in energy due to intramolecular contributions. Intermolecular interactions are counted twice in their derivation of the acceptance rules, which is incorrect [81, 174, 175]. Rosch *et al.* [81] have derived the correct acceptance rules. Keil *et al.* [67, 68] have studied propene metathesis reactions within confined environments. These authors have combined the Configurational-Bias Monte Carlo (CBMC) approach with the Reaction Ensemble Monte Carlo

algorithm for linear alkanes and alkenes. The Configurational-Bias Monte Carlo algorithm is useful for simulating larger molecules as inserting these large molecules in confined systems is extremely difficult [53, 115, 116]. To the best of our knowledge, application of the Reaction Ensemble Monte Carlo algorithm for complex molecules and reactions in a dense liquid phase has not been studied.

A reaction in the Reaction Ensemble involved the deletion of reactants and the insertion of the reaction products. These so-called "insertions" and "deletions" are accepted in such a way that the correct equilibrium distribution is sampled. The efficiency and accuracy of these simulations depend on the probability of successful insertions and deletions of molecules. At high densities typically encountered in a liquid phase, the probability of successful insertions and deletions is very low due to a large number of overlaps with the existing molecules in the simulation box [53, 70, 78]. To increase the efficiency of the successful insertions and deletions, Maginn *et al.* [78, 79] have developed the Continuous Fractional Component Monte Carlo (CFCMC) method to insert/delete molecules in a more gradual manner. Torres-Knoop *et al.* [70] have combined the CBMC with the CFCMC to obtain higher computational efficiencies. Other works have been published proposing methods that try to increase the efficiency of insertion and deletion in dense liquids [83–85]. Rosch *et al.* have extended the CFCMC method for the Reaction Ensemble, coupling the CFCMC for inserting the product molecules and deleting the reactant molecules based on their respective stoichiometry [81]. To compute the absorption isotherms of $CO_2$ in aqueous MEA solutions, the CFCMC method in the osmotic ensemble is used [70, 78].

In this chapter, we use the Reaction Ensemble Monte Carlo using the Continuous Fractional Component (RxMC/CFC) method to simulate the chemical equilibrium of $CO_2$ in the MEA solution and determine computationally the equilibrium concentrations of the different species in the system. The solubility of $CO_2$ in the MEA solution was also computed for different partial pressures. The computational results are compared to experimental results from literature. We study the effects of different reaction mechanisms on the equilibrium concentrations of the various species. The rest of this chapter is organized as follows: section 4.2 deals with simulating the reactions and solubility of $CO_2$ in the MEA solution along with the derivation of the acceptance rules for the RxMC/CFC algorithm. Section 4.4 contains the different results and discussions and our findings are summarized in section 4.5.

## 4.2 Reactions of $CO_2$ in Aqueous MEA Solutions

The reactions of $CO_2$ with primary and secondary amine solutions usually takes place through an acid-base buffer mechanism which results in the formation of stable carbamates and bicarbonate followed by the subsequent protonation of the amine [27]. Non-hindered primary and secondary amines react rapidly with $CO_2$ to form carbamate ions and the addition of water increases the absorption capacity and rate. Tertiary amines react with $CO_2$ via the bicarbonate pathway to form bicarbonate ion and the ammonium salt of the amine. Since monoethanolamine ($HOCH_2CH_2NH_2$) is a primary amine, the reactions take place via the carbamate ion pathway [18, 164]:

Reactions: MEA + $CO_2$ (carbamate pathway)

$$CO_2 + 2H_2O \rightleftharpoons HCO_3^- + H_3O^+ \quad \text{(R1)}$$

$$HCO_3^- + H_2O \rightleftharpoons CO_3^{2-} + H_3O^+ \quad \text{(R2)}$$

$$HOCH_2CH_2NH_2 + H_3O^+ \rightleftharpoons HOCH_2CH_2NH_3^+ + H_2O \quad \text{(R3)}$$

$$HOCH_2CH_2NH_2 + HCO_3^- \rightleftharpoons HOCH_2CH_2NHCOO^- + H_2O \quad \text{(R4)}$$

These reactions are generally described in the literature [18, 160, 164, 167]. It is important to note that in the reactions mentioned above, the appearance of $H_3O^+$ is to avoid the presence of $H^+$ in the system, as $H^+$ does not obey the Born-Oppenheimer approximation for classical simulations [53]. Some other additional reactions have also been described in the literature [160]. MEA is also able to form 2-oxazolidone which is a heterocyclic component [37, 160]. Other amine degradation reaction mechanisms are also possible [36, 37]. In spite of the different possible reaction mechanisms, the aim of all modeling and experimental studies is to obtain the equilibrium concentrations of the different species. In this regard, Reactions R1, R3 and R4 may be combined to result in a simplified Reaction R5 which is given by,

$$CO_2 + 2HOCH_2CH_2NH_2 \rightleftharpoons HOCH_2CH_2NH_3^+ + HOCH_2CH_2NHCOO^- \quad \text{(R5)}$$



## 4.3 Derivation of RxMC/CFC Algorithm

### 4.3.1. Molecular Partition Function

Consider the RxMC algorithm for a single reaction system involving $n$ species. Equilibrium is achieved when

$$\sum_{i=1}^{n} \nu_i \mu_i = 0 \quad (4.1)$$

where $\nu_i$ and $\mu_i$ are the stoichiometric coefficient and the chemical potential of species $i$, respectively [176]. The molecular partition function $q_i$, of an isolated molecule of type $i$ in the ideal gas phase is defined by [66]

$$q_i = q_{i,\mathrm{qm}} q_{q,\mathrm{cl}} = \frac{q_{i,\mathrm{qm}}}{\hbar^{f_i}} \int \exp[-\beta \mathcal{H}_{i,\mathrm{cl}}(p_i, r_i)] \mathrm{d}p_i \mathrm{d}r_i \quad (4.2)$$

where $\hbar$ is Planck's constant, $q_{i,\mathrm{cl}}$ is the classical molecular partition function, $q_{i,\mathrm{qm}}$ is the quantum molecular partition function of isolated molecules of type $i$, $\beta = 1/(k_\mathrm{B}T)$, $p_i$ and $r_i$ are the momenta and generalized coordinates associated with all the classical degrees of freedom of species $i$, and $\mathcal{H}_{i,\mathrm{cl}}$ is the classical Hamiltonian of the system. The molar standard chemical potential of an isolated molecule in the gas phase $\mu_i^0$ is related to the total molecular partition function $q_i$ by [66]

$$\frac{\mu_i^0}{k_\mathrm{B}T} = -\ln\left(\frac{q_i}{\beta p^0 \Lambda_i^3}\right) \quad (4.3)$$

where $p^0$ is the standard state pressure (1 bar) and $\Lambda_i$ is the thermal de Broglie wavelength of molecules of type $i$. The Hamiltonian of a molecule $\mathcal{H}_i$ can be approximated as a sum of Hamiltonians for the various degrees of freedom of the molecule [52]

$$\mathcal{H}_i \approx \mathcal{H}_{i,\text{trans}} + \mathcal{H}_{i,\text{rot}} + \mathcal{H}_{i,\text{vib}} + \mathcal{H}_{i,\text{elec}} \tag{4.4}$$

where $\mathcal{H}_{i,\text{trans}}, \mathcal{H}_{i,\text{rot}}, \mathcal{H}_{i,\text{vib}}, \mathcal{H}_{i,\text{elec}}$ are the Hamiltonian of the translational, rotational, vibrational, and electronic degrees of freedom respectively of a molecule of type $i$. Consequently, the molecular partition function $q_i$ can be expressed in terms of the various degrees of freedom of the molecule as [52]

$$q_i = q_{i,\text{trans}} q_{i,\text{rot}} q_{i,\text{vib}} q_{i,\text{elec}} \tag{4.5}$$

$$= q_{i,\text{trans}} q_{i,\text{int}} \tag{4.6}$$



where $q_{i,\text{trans}}$, $q_{i,\text{rot}}$, $q_{i,\text{vib}}$, $q_{i,\text{elec}}$ are the translational, rotational, vibrational and electronic contributions to the molecular partition function of a molecule of type $i$. The internal contributions to the molecular partition function $q_{i,\text{int}}$ are the rotational, vibrational and electronic degrees of freedom:

$$q_{i,\text{int}} = q_{i,\text{rot}} q_{i,\text{vib}} q_{i,\text{elec}} \tag{4.7}$$

The translational partition function depends on temperature as well as the volume [52]:

$$q_{i,\text{trans}} = \left( \frac{2\pi m_i k_\text{B} T}{h^2} \right)^{3/2} V \tag{4.8}$$

$$= \frac{V}{\Lambda_i^3} \tag{4.9}$$

$$= \frac{q_i}{q_{i,\text{int}}} \tag{4.10}$$

where $m_i$ is the mass of the molecule of type $i$ and $V$ is the volume of the system. In our case, the volume $V$ is the volume of the simulation box. This molecular partition function $q_i$ can be split into two parts, one part which depends on only the temperature $\hat{q}_i(T)$, and the other which depends only on the volume. Incorporating this in Eq. (4.5), we obtain,

$$q_i = \hat{q}_i(T) V \tag{4.11}$$

Quantum mechanical simulations using GAUSSIAN 09 [177] are performed to obtain the molecular partition functions. The output of GAUSSIAN 09 [177] provides the values for the individual contributions to the partition functions (translational, rotational, vibrational and electronic). The volume term in the translational partition function is calculated in GAUSSIAN 09 using the ideal gas law for a single isolated molecule: $V = k_\text{B}T/P$ [178]. Since the volume changes in our Monte Carlo simulations one needs to consider that $q_i$ changes when $V$ changes. To this end, we have explicitly separated the volume term and used $\hat{q}_i(T)$ as input to our simulations. The values of the computed partition functions are listed in Table 4.1.

Table 4.1: Partition Functions ($\hat{q}_i(T)$) of the isolated molecules at different temperatures 293 K, 333 K, 353 K computed using quantum mechanical simulations using GAUSSIAN 09 [177, 178].

| Molecule | $\hat{q}_i$ (293 K) ($\text{Å}^{-3}$) | $\hat{q}_i$ (333 K) ($\text{Å}^{-3}$) | $\hat{q}_i$ (353 K) ($\text{Å}^{-3}$) |
|---|---|---|---|
| $CO_2$ | $7.8752 \cdot 10^4$ | $1.1294 \cdot 10^5$ | $1.3368 \cdot 10^5$ |
| MEA | $6.9980 \cdot 10^7$ | $1.4048 \cdot 10^8$ | $1.9685 \cdot 10^8$ |
| $MEAH^+$ | $8.8994 \cdot 10^7$ | $1.8468 \cdot 10^8$ | $2.6286 \cdot 10^8$ |
| $MEACOO^-$ | $5.1046 \cdot 10^9$ | $1.3078 \cdot 10^{10}$ | $2.0653 \cdot 10^{10}$ |
| $H_2O$ | $3.0134 \cdot 10^3$ | $4.4259 \cdot 10^3$ | $5.2742 \cdot 10^3$ |
| $H_3O^+$ | $4.8631 \cdot 10^3$ | $7.2028 \cdot 10^3$ | $8.6279 \cdot 10^3$ |
| $HCO_3^-$ | $1.6616 \cdot 10^7$ | $2.7090 \cdot 10^7$ | $3.4201 \cdot 10^7$ |
| $CO_3^{2-}$ | $6.8336 \cdot 10^6$ | $1.0663 \cdot 10^7$ | $1.3155 \cdot 10^7$ |



### 4.3.2. RxMC/CFC Algorithm

To obtain the equilibrium concentrations of the different species in a reacting mixture, the Reaction Ensemble Monte Carlo (RxMC) [66–68, 179] is used. The RxMC algorithm samples the reactions directly and bypasses transition states. The RxMC algorithm only requires the stoichiometric coefficients of the reactions as an input and the partition functions of the isolated molecules or ions, along with the force field parameters to compute the intermolecular interactions. Therefore, the RxMC method allows for a systematic study of the effect of the medium (or solvent) on the reaction equilibrium constant.

The reaction trial move within the RxMC framework involves choosing the forward or reverse reaction at random. If the forward reaction is chosen, the reactant molecules are deleted and the product molecules are inserted according to their stoichiometries. For dense systems, these insertions and deletions of molecules, if performed in a single step, often lead to overlaps with the surrounding molecules. The probabilities of successful insertions/deletions of the molecules are very low. To circumvent this problem, Maginn *et al.* [78, 79] have developed the Continuous Fractional Component Monte Carlo method. Fractional molecules of the reactants and products are introduced into the system. By controlling the interactions of these fractional molecules with the surrounding molecules, the reactants/products are gradually inserted or removed. This is controlled by a pseudocoupling factor, $\lambda$. Changes in $\lambda$ will gradually insert or delete the molecules appropriately. Section 3.2.2 provides a detailed explanation on the Continuous Fractional Component Monte Carlo method.

The reaction ensemble is best described by taking the osmotic ensemble as the starting point, since most chemical reactions take place in a system at constant pressure. Let $N_i$ denote the number of molecules of type $i$, $P$ the imposed hydrostatic pressure, $V$ the volume, and $\mu_i$ the chemical potential of the species $i$. For an expanded osmotic ensemble, the partition function for a system of $n$ species can

be expressed as [81]

$$\Xi_{\text{biased}}(\mu_1,..,\mu_n,p,T) = \beta P \int_0^1 \mathrm{d}\lambda \sum_{N_i=0}^{\infty} \cdots \sum_{N_n=0}^{\infty} \int \mathrm{d}s^{N_1}\mathrm{d}\omega^{N_1} \cdots \mathrm{d}s^{N_n}\mathrm{d}\omega^{N_n}\mathrm{d}V \exp\left[\beta \sum_{i=1}^{n} N_i\mu_i - \sum_{i=1}^{n} \ln N_i! + \sum_{i=1}^{n} N_i \ln(\hat{q}_i(T)V) - \beta PV - \beta U(s^N,\omega^N,\lambda)\right] \exp[\eta(\lambda)/k_{\text{B}}T] \tag{4.12}$$

where $s^{N_i}$ are the configurations of the $N_i$ molecules of type $i$, $\omega^{N_i}$ are the orientations and internal configurations of $N_i$ molecules of type $i$ and $U(s^N,\omega^N,\lambda)$ is the potential energy of the system. $\beta = 1/k_BT$, $\hat{q}_i(T)$ is the temperature dependent term in the molecular partition function $q_i$ for the molecule of type $i$. $q_i = \hat{q}_i(T)V$. $\eta(\lambda)$ are the biasing factors introduced to improve the probabilities of transitions in $\lambda$. From Eq. (4.12), it follows that the probability that the system is in a certain state is

$$p_{\text{biased}} \sim \exp\left[\beta \sum_{i=1}^{n} N_i\mu_i - \sum_{i=1}^{n} \ln N_i! + \sum_{i=1}^{n} N_i \ln(\hat{q}_i(T)V) - \beta PV - \beta U(s^N,\omega^N,\lambda)\right] \exp[\eta(\lambda)/k_{\text{B}}T] \tag{4.13}$$

This equation can be used to derive the acceptance rules in our Monte Carlo algorithm.

### 4.3.3. Reaction Ensemble Monte Carlo using the Continuous Fractional Component Algorithm

Let us consider a reaction involving $c$ species in a system consisting of $n$ molecule types. For the species not involved in the reaction, the stoichiometric coefficient $\nu_i$ is set to 0 by definition. If a reaction takes place in the forward or reverse direction, there will be a change in the molecules of each component. The state before the reaction takes place is now denoted by old state "o", while the state after the reaction takes place is denoted by new state "n". Since the reaction has taken place, we know how the number of molecules of each component changes:

$$N_{i,\text{n}} = N_{i,\text{o}} + \nu_i \tag{4.14}$$

The probabilities to exist in states "o" and "n" can be obtained from Eq. (4.13). Substituting Eq. (4.14) in Eq. (4.13) for the new state, the expressions for the

probabilities to exist in the old and the new states are,

$$p_{\mathrm{o,biased}} \sim \exp\Bigg[\beta\sum_{i=1}^{n} N_{i,\mathrm{o}}\mu_i - \sum_{i=1}^{n}\ln N_{i,\mathrm{o}}! + \sum_{i=1}^{n} N_{i,\mathrm{o}}\ln(\hat{q}_i(T)V_{\mathrm{o}}) - \beta PV_{\mathrm{o}} - \beta U_{\mathrm{o}}(s^{N,\mathrm{o}},\omega^{N,\mathrm{o}},\lambda_{\mathrm{o}})\Bigg]\exp[\eta(\lambda_{\mathrm{o}})/k_{\mathrm{B}}T] \tag{4.15}$$

$$p_{\mathrm{n,biased}} \sim \exp\Bigg[\beta\sum_{i=1}^{n}\nu_i\mu_i + \beta\sum_{i=1}^{n} N_{i,\mathrm{o}}\mu_i - \sum_{i=1}^{n}\ln(N_{i,\mathrm{o}}+\nu_i)! + \sum_{i=1}^{n} N_{i,\mathrm{o}}\ln(\hat{q}_i(T)V_{\mathrm{n}}) + \sum_{i=1}^{n}\nu_i\ln(\hat{q}_i(T)V_{\mathrm{n}}) - \beta PV_{\mathrm{n}} - \beta U_{\mathrm{n}}(s^{N,\mathrm{n}},\omega^{N,\mathrm{n}},\lambda_{\mathrm{n}})\Bigg]\exp[\eta(\lambda_{\mathrm{n}})/k_{\mathrm{B}}T] \tag{4.16}$$

### 4.3.4. Acceptance Rules of RxMC/CFC

Averages in the Boltzmann ensemble (denoted by $\langle\cdots\rangle$) follow directly from biased averages (denoted by $\langle\cdots\rangle_{\mathrm{biased}}$) according to Eq. (3.19) [51]. In the Reaction Ensemble Monte Carlo using Continuous Fractional Component method, there are four types of trial moves possible:

1. Change the position of a randomly selected molecule (either a regular or a fractional molecule)
2. Change the orientation of a randomly selected molecule (either a regular or a fractional molecule)
3. Change the volume of the system
4. Change the coupling parameter $\lambda$ of a randomly selected reaction. The reactions are chosen with equal probability. This can be further divided into 3 cases ($\Delta\lambda$ is the change in $\lambda$):
   (a) $0 \leq \lambda + \Delta\lambda \leq 1$
   (b) $\lambda + \Delta\lambda < 0$
   (c) $\lambda + \Delta\lambda > 1$

The first two Monte Carlo moves are trivial and have the same acceptance rules as the ones derived previously [51, 53]. For the Volume Change Monte Carlo trial move, random walks are made in $\ln(V_{\mathrm{n}}/V_{\mathrm{ref}})$ [53] in which $V_{\mathrm{ref}}$ is an arbitrary reference

volume. The probabilities of existing in the old state "o" and the new state "n" are

$$p_{\mathrm{o,biased}} \sim \beta P V_{\mathrm{o}} \exp\Bigg[\beta \sum_{i=1}^{n} N_{i,\mathrm{o}}\mu_i - \sum_{i=1}^{n} \ln N_{i,\mathrm{o}}! + \sum_{i=1}^{n} N_{i,\mathrm{o}} \ln(\hat{q}_i(T)V_{\mathrm{o}}) - \beta P V_{\mathrm{o}} - \beta U_{\mathrm{o}}(s^N, \omega^N, \lambda)\Bigg] \exp[\eta(\lambda_{\mathrm{o}})/k_{\mathrm{B}}T] \tag{4.17}$$

$$p_{\mathrm{n,biased}} \sim \beta P V_{\mathrm{n}} \exp\Bigg[\beta \sum_{i=1}^{n} N_{i,\mathrm{o}}\mu_i - \sum_{i=1}^{n} \ln N_{i,\mathrm{o}}! + \sum_{i=1}^{n} N_{i,\mathrm{o}} \ln(\hat{q}_i(T)V_{\mathrm{n}}) - \beta P V_{\mathrm{n}} - \beta U_{\mathrm{n}}(s^N, \omega^N, \lambda)\Bigg] \exp[\eta(\lambda_{\mathrm{n}})/k_{\mathrm{B}}T] \tag{4.18}$$



For random walks in $\ln(V_{\mathrm{n}}/V_{\mathrm{ref}})$, $\lambda_{\mathrm{o}} = \lambda_{\mathrm{n}}$ and $\eta(\lambda_{\mathrm{o}}) = \eta(\lambda_{\mathrm{n}})$. The acceptance rule is therefore

$$\mathrm{acc}(o \to n) = \min\Bigg(1, \left(\frac{V_{\mathrm{n}}}{V_{\mathrm{o}}}\right)^{N+1} \exp[-\beta P(V_{\mathrm{n}} - V_{\mathrm{o}})] \exp[-\beta(U_{\mathrm{n}}(s^N, \omega^N, \lambda) - U_{\mathrm{o}}(s^N, \omega^N, \lambda))]\Bigg) \tag{4.19}$$

This expression is the same as the acceptance rule derived previously [53].

We now consider the reaction move as a change in $\lambda$ of the system. For the reaction move, $V_{\mathrm{o}} = V_{\mathrm{n}}$. Looking into more detail at the three different cases when $\lambda$ is changed, we have:

**First case (a)**, where $0 \leq \lambda + \Delta\lambda \leq 1$, is the case where there is no addition or deletion of molecules. The old state is denoted by "o" and $\lambda_{\mathrm{o}}$ is the old coupling factor of the reaction. The new state is denoted by "n" and $\lambda_{\mathrm{n}} = \lambda_{\mathrm{o}} + \Delta\lambda$. From Eq. (4.13), we can obtain the probabilities to exist in old and new states. As the number of molecules in the system remain the same for the old and the new configurations, the acceptance rule is

$$\mathrm{acc}(o \to n) = \min\Bigg(1, \exp[-\beta(U_{\mathrm{n}}(s^N, \omega^N, \lambda_{\mathrm{n}}) - U_{\mathrm{o}}(s^N, \omega^N, \lambda_{\mathrm{o}}))] \exp[(\eta(\lambda_{\mathrm{n}}) - \eta(\lambda_{\mathrm{o}}))/k_{\mathrm{B}}T]\Bigg) \tag{4.20}$$

**Second case (b)**, where $\lambda + \Delta\lambda > 1$, is the case of a reverse reaction. The $\lambda$ of the old fractional reactant and product molecules are set to 1 and 0 respectively. New fractional reactant molecules are inserted into the system with $\lambda_{\mathrm{n}} = (\lambda_{\mathrm{o}} + \Delta\lambda) - 1$. Random product molecules are selected from the system and their $\lambda$ is set from 1 to $1 - \lambda_{\mathrm{n}}$.

**Third case (c)**, where $\lambda + \Delta\lambda < 0$, is when there is a forward reaction. The $\lambda$ of the old fractional reactant and product molecules are set to 0 and 1 respectively. New

fractional product molecules are inserted into the system with $\lambda_n = (\lambda_o + \Delta\lambda) - 1$. Random reactant molecules are selected from the system and their $\lambda$ is set to $1 - \lambda_n$.

In cases two and three, the reaction has proceeded, either in the forward direction or the backward direction. Substituting Eq. (4.1) in Eq. (4.16) since the reaction takes place at equilibrium, the expression for the acceptance rule for the forward/reverse reaction (cases (b) and (c)) is

$$\begin{aligned} \mathrm{acc}(o \to n) = \min \Bigg(1, \prod_{i=1}^{n} \left( \frac{N_i^o!}{(N_i^o + \nu_i)!} (\hat{q}_i(T)V)^{\nu_i} \right) \\ \exp[-\beta(U_n(s^N, \omega^N, \lambda_n) - U_o(s^N, \omega^N, \lambda_o))] \\ \exp[(\eta(\lambda_n) - \eta(\lambda_o))/k_B T]) \end{aligned} \tag{4.21}$$

The acceptance rule for the RxMC derived above for one reaction can be generalized easily to include many reactions in the same system. It is important to note that in the acceptance rule (Eq. (4.21)), the volume term is included explicitly, since during the simulation the volume of the system changes.
It is instructive to consider the case of a reaction in a mixture of ideal gases. In that case, the acceptance rule of Eq. (4.21) reduces to

$$\mathrm{acc}(o \to n) = \min \left(1, \prod_{i=1}^{n} \left( \frac{N_i^o!}{(N_i^o + \nu_i)!} (\hat{q}_i(T)V)^{\nu_i} \right) \right) \tag{4.22}$$

If the total number of molecules does not change during the reaction ($\sum_{i=0}^{n} \nu_i = 0$), it is well known from classical thermodynamics that the equilibrium constant is only a function of the molecular partition functions [180]. From Eq. (4.22), it can also be observed that there will be no dependence on the volume of the system when $\sum_{i=0}^{n} \nu_i = 0$ as the volume term $V$ cancels out in Eq. (4.22) and the expression reduces to

$$\mathrm{acc}(o \to n) = \min \left(1, \prod_{i=1}^{n} \left( \frac{N_i^o!}{(N_i^o + \nu_i)!} (\hat{q}_i(T))^{\nu_i} \right) \right). \tag{4.23}$$

If there is a change in the number of molecules during the reaction ($\sum_{i=0}^{n} \nu_i \neq 0$), the acceptance rule will now depend on the volume of the system, as can be seen from Eq. (4.22). It is important to consider the volume dependent term of the partition function explicitly in the acceptance rules since in many cases, the number of molecules during the reaction changes ($\sum_{i=0}^{n} \nu_i \neq 0$). It is unclear whether or not this volume term was taken into account correctly in previous studies from literature. Of course, the final results will not be affected if the simulations consider reactions where the number of molecules does not change due to the reaction [67, 68, 81].

### 4.3.5. Simulation Details

Two different sets of reactions are studied to obtain the equilibrium speciations by including: (1) Reactions R1-R4; (2) only Reaction R5. All simulations are performed

in the Reaction Monte Carlo Ensemble (RxMC) in the constant temperature, constant pressure ensemble. The hydrostatic pressure of the system equals 1 bar. The effect of temperatures on the equilibrium compositions of the mixture is also studied. Different loadings of $CO_2$ have also been investigated. The initial concentration of MEA in the aqueous MEA solution is 30 weight percent. Böttinger *et al.* [160] measured the speciations at different loadings higher than 0.5 mole $CO_2$/mole MEA using online NMR spectroscopy. To achieve high loadings of $CO_2$ in experiments, the partial pressure of $CO_2$ ranged from 5 bar to 25 bar. In our simulations, a system with a fixed number of $CO_2$ molecules is simulated and only the hydrostatic pressure of the system needs to be specified. As the properties of a liquid phase do not depend much on the hydrostatic pressure and the total loading of $CO_2$ is specified, one can safely assume a hydrostatic pressure of 1 bar.



Quantum mechanical simulations using GAUSSIAN 09 [177] are performed to obtain the partition functions $\hat{q}_i$ of the isolated molecules required for the RxMC/CFC molecular simulations. All molecular species involved in the reaction were optimized with a second order Møller-Plesset perturbation method (MP2) in combination with a 6-311+G(2d,2p) basis set at different temperatures (293 K, 333 K, 353 K). A frequency analysis was performed on the optimized geometries to confirm the true minima on the potential energy surface and to obtain partition functions of all the molecules. All the calculations were performed with GAUSSIAN 09 [177]. Mulliken atomic charges were obtained from population analysis of self-consistent field density matrix. The individual contributions of translational, vibrational, rotational and electronic motions are considered for the calculation of the partition function for every molecule. [178]. The partition functions were split into a temperature dependent part and a volume dependent part.

Simulations to compute the absorption isotherms of $CO_2$ in aqueous MEA solutions combine both the RxMC/CFC and the Continuous Fractional Component Monte Carlo (CFCMC) method in the osmotic ensemble. The osmotic ensemble using the CFCMC simulates the equilibrium absorption and desorption of $CO_2$ molecules in the aqueous MEA solvent. The processes of absorption/desorption as well as the reaction of $CO_2$ molecules with aqueous MEA solvent take place simultaneously. The simulations are performed in the osmotic ensemble, which implies that the fugacity of the gas ($f$), the number of MEA and $H_2O$ molecules (non volatile) ($N$), the total hydrostatic pressure ($P$) and the temperature ($T$) are all fixed. The volume of the system and the number of gas molecules in the liquid phase will change as a consequence of the imposed pressure and fugacity in order to satisfy the equilibrium condition $f_i^V = f_i^L$. It is important to note that the Gibbs phase rule is not violated by disallowing MEA and $H_2O$ molecules in the gas phase, because the number of equilibrium conditions and the number of intensive variables are both reduced. Furthermore, since MEA has a negligible vapor pressure, our assumption that only $CO_2$ molecules will be present in the gas phase is valid. The results from simulation are compared with the results from Jou *et al.* [31].

Force fields for the MEA have been taken from the OPLS force field [57]. Intermolecular potential parameters and intramolecular potential parameters for $MEAH^+$ and $MEACOO^-$ have also been taken from the OPLS force field. Force field param-

eters for $CO_2$ have been taken from the TraPPE force field [181] and for water from the Tip4p water model has been used [59]. The force field parameters for $H_3O^+$ are taken from Vacha *et al.* [182] The force field parameters for the $HCO_3^-$ and $CO_3^{2-}$ have been taken from the OPLS database. Water, MEA, $MEA^+$, $MEACOO^-$, $H_3O^+$, $HCO_3^-$ and $CO_3^{2-}$ are modeled as rigid molecules. The partial charges for $HCO_3^-$, $CO_3^{2-}$, $MEACOO^-$ and $MEAH^+$ have been computed from quantum mechanical simulations in GAUSSIAN 09 [177]. Electrostatic interactions were handled by the Ewald summation algorithm [183] with a relative precision of $10^{-5}$. The cut-off radius was set at 12 Å for the Lennard-Jones interactions. $\sigma$ and $\epsilon$ are the Lennard-Jones (LJ) parameters [117]. The Lorentz-Berthelot mixing rules were used to calculate the Lennard-Jones parameters between different atoms ($\sigma_{ij}$ and $\epsilon_{ij}$). The values of all the force field parameters can be found in the Supporting Information of Ref. [69]. Monte Carlo simulations in the RxMC/CFC ensemble were performed using RASPA [117], a program for Monte Carlo and Molecular Dynamics simulations. Monte Carlo simulations of 1-2 million cycles were performed for equilibration and production runs of 4-8 million cycles were performed, where one MC cycle is equal to the total number of molecules in the system. For simulating equilibrium concentrations, the probabilities of selecting a translation move, a rotation move, a partial reinsertion move and a reaction move were all 0.245. The probability of selecting a volume change move was 0.02. For obtaining adsorption isotherms, the probabilities of selecting a translation move, a rotation move, a reaction move and an insertion/deletion move were all 0.249. The probability of selecting a volume change move was 0.02. Simulations for computing equilibrium concentrations were performed with 444 water molecules, 56 MEA molecules and the appropriate number of $CO_2$ molecules depending on the loading. Simulations for computing absorption isotherms were performed with 444 water molecules, 56 MEA molecules and a gas phase of $CO_2$ molecules. The size of the simulation box varied around 27 Å. By switching off electrostatics and intermolecular van der Waals interactions, the effect of electrostatics and intermolecular interactions on the reaction equilibrium was studied. At the start of the simulation, fractional molecules were assigned for all reacting species for both reactants and products in the Reactions R1-R4. The net charge of the fractional molecules (both the reactants and products) of all the Reactions R1-R4 is not zero. It is important to note that if we sum Reactions R1, R2, R3, and R4, the total net charge of the reactants equals -1. Similarly, the total net charge of products of the summed reactions also equals -1. To keep the simulation box charge neutral independent of the value of $\lambda$ for each reaction, two $H_3O^+$ fractional molecules, one as a reactant and the other as a product in Reaction R2, were added to the simulation box. This ensures that during the reaction the simulation box is always charge neutral. For the RxMC/CFC and CFCMC in the osmotic ensemble, the Lennard-Jones parameters as well as the partial charges are scaled with pseudo coupling factors which are changed during the reaction move and the insertion/deletion move respectively. The CPU time required to compute the equilibrium concentrations ranged from 3-4 weeks in total for the equilibration and production runs using state-of-the-art computation facilities.

Table 4.2: Equilibrium constants for the different ideal gas reactions at 293 K and 353 K as obtained from the computed partition functions.

| Reactions | $K_{\text{idealgas}}$ (293 K) | $K_{\text{idealgas}}$ (353 K) |
|---|---|---|
| R1 | $2.8302 \cdot 10^{-06}$ | $1.6498 \cdot 10^{-06}$ |
| R2 | $6.6368 \cdot 10^{-01}$ | $6.2920 \cdot 10^{-01}$ |
| R3 | $7.8802 \cdot 10^{-01}$ | $8.1627 \cdot 10^{-01}$ |
| R4 | $1.3229 \cdot 10^{-02}$ | $1.6179 \cdot 10^{-02}$ |
| R5 | $2.9504 \cdot 10^{-08}$ | $2.1787 \cdot 10^{-08}$ |

## 4.4 Results and Discussion



### 4.4.1. Effect of Electrostatics and Intermolecular van der Waals Interactions

When there are no intermolecular interactions between molecules, the system behaves as an ideal gas. For an ideal gas system, the equilibrium constant can be written directly in terms of the molecular partition functions of the individual species [184] which can be calculated from quantum simulations. To observe the effect of intermolecular interactions, the intermolecular van der Waals interactions and the electrostatics were "switched off" *i.e.*, all the intermolecular Lennard-Jones parameters and electrostatics were set to zero. From the simulations, it was observed that forward reactions did not take place when including (1) reactions R1-R4, and (2) only reaction R5. Equilibrium constants for these ideal gas reactions calculated from quantum simulations are specified in Table 4.2. The equilibrium constants for the forward reaction are extremely low. Equilibrium concentrations of the species for the ideal gas system can be obtained by solving the non-linear expressions for the equilibrium constants. The analytical solutions yield extremely low concentrations of carbamates and protonated amines. This is consistent with the results obtained from simulations performed when the intermolecular van der Waals interactions and the electrostatic are set to zero. It can be observed from the results of the simulations and analytical solutions that intermolecular interactions are necessary to compute the equilibrium concentrations of the species. Equilibrium speciations cannot be obtained by only performing quantum simulations as the system cannot be treated as an ideal gas. As expected, the solvation of ions in the solution is essential for the different reactions to take place. Classical simulations take into account the intermolecular interactions between the species and this is necessary to compute the equilibrium concentrations of the species. If the reaction occurs in the ideal gas phase, the ions are not solvated and energetically this is very unfavorable.

### 4.4.2. Chemical Equilibrium of $CO_2$ in Aqueous MEA Solution

The equilibrium mole fractions of the different species were obtained at different temperatures (293 K, 333 K, 353 K) and at a hydrostatic pressure of 1 bar for different loadings of $CO_2$ (mole $CO_2$/mole MEA) by performing Monte Carlo simulations in the Reaction Ensemble using the Continuous Fractional Compo-

nent method. In Figs. 4.1, 4.2 and 4.3, the equilibrium mole fractions of the species MEA, $MEAH^+$, $MEACOO^-$, $CO_2$ and $HCO_3^-$ are compared to experimental data [160, 167]. Poplsteinova *et al.* [167] and Böttinger *et al.* [160] measured the equilibrium speciation of $CO_2$-MEA-$H_2O$ system using NMR spectroscopy. Böttinger *et al.* [160] report the sum of equilibrium concentrations of MEA and $MEAH^+$, since it was impossible to distinguish between the protonated and the unprotonated MEA experimentally. In order to obtain the individual equilibrium concentrations of MEA and $MEAH^+$, these authors have used a thermodynamic model.

Fig. 4.1a shows the speciation of the $CO_2$+MEA solution for different loadings of $CO_2$ (mole $CO_2$/mole MEA) at 293 K and 1 bar when the reactions R1-R4 are used. The equilibrium concentration of the different species of $CO_2$+MEA solution exhibits the typical behavior of the primary amines. At low loadings until 0.5 mole $CO_2$/mole MEA, all $CO_2$ molecules react with the MEA molecules forming the carbamate and the protonated amine products. The concentrations of the carbamate and the protonated MEA increase as the loading of $CO_2$ increases until 0.5 mole $CO_2$/mole MEA, while the concentration of MEA decreases. At the loading of $CO_2$ of 0.5 mole $CO_2$/mole MEA, all the MEA has now reacted with the $CO_2$. Beyond loadings of $CO_2$ of 0.5 mole $CO_2$/mole MEA, the concentrations of the carbamate start to decrease and the concentrations of the protonated MEA increase. Beyond the loadings of $CO_2$ of 0.5 mole/mole MEA, bicarbonate ions were observed. The simulation results are in excellent agreement with the experimental results of Böttinger *et al.* [160].

Fig. 4.1b shows the equilibrium concentrations of MEA, $MEAH^+$, $MEACOO^-$ and $CO_2$ for different loadings of $CO_2$ (mole $CO_2$/mole MEA) at 293 K and 1 bar when only the reaction R5 is considered. The results of equilibrium speciations obtained from simulating only reaction R5 follow the same trends for the concentrations of MEA, protonated MEA and the carbamate when we include all reactions R1-R4. Until loadings of 0.5 mole $CO_2$/mole MEA, the concentrations of the carbamate and the protonated MEA increase and the concentration of free MEA decreases. Beyond loadings of 0.5 mole $CO_2$/mole MEA, typically all the MEA has reacted with the $CO_2$. The concentrations of MEA, protonated MEA and $MEACOO^-$ remain constant, while concentration of unreacted $CO_2$ increases for loadings higher than 0.5 mole $CO_2$/mole MEA.

Böttinger *et al.* [160] also used a thermodynamic model to study the $CO_2$-MEA-$H_2O$ system and obtained the individual equilibrium concentrations of the different species: MEA, $MEAH^+$, $MEACOO^-$, $CO_2$, $HCO_3^-$. These authors have developed the model by simultaneously taking into account the chemical reactions and the vapor-liquid equilibria of the $CO_2$-MEA-$H_2O$ mixture into consideration. Fig. 4.2 compares our simulation results of the individual equilibrium concentrations including MEA and $MEA^+$ with the results from the thermodynamic model of Böttinger *et al.* We find an excellent agreement with the model. It is important to note that we obtain individual concentrations of all the species in the mixture directly from simulations and we need not use any iterative modeling technique which requires binary interaction parameters, activity coefficients of molecular and ionic species, equilibrium coefficients, etc. as input.

Figs. 4.3 and 4.4 show the results of the speciations for different temperatures 333 K and 353 K at 1 bar. It can be observed that an increase in temperature does not significantly affect the equilibrium concentrations of the species. For Fig. 4.4, there is no experimental data beyond loadings of 0.5 mole $CO_2$/mole MEA. This is again in excellent agreement with the experimental results of Böttinger *et al.* [160] who also observe that the speciations of the $CO_2$+MEA solution are only very weakly temperature dependent.

(a)

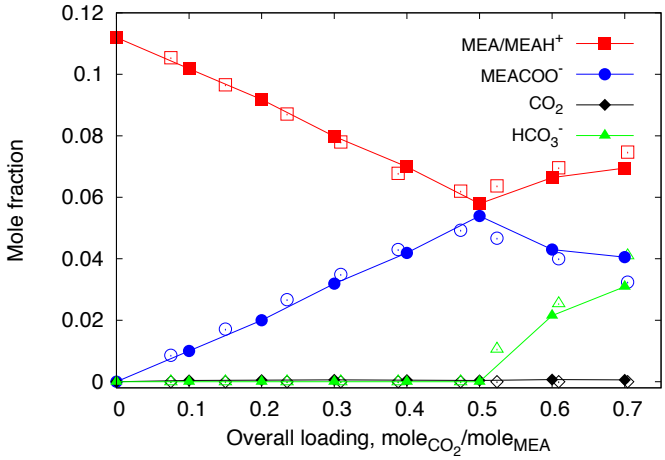


(b)

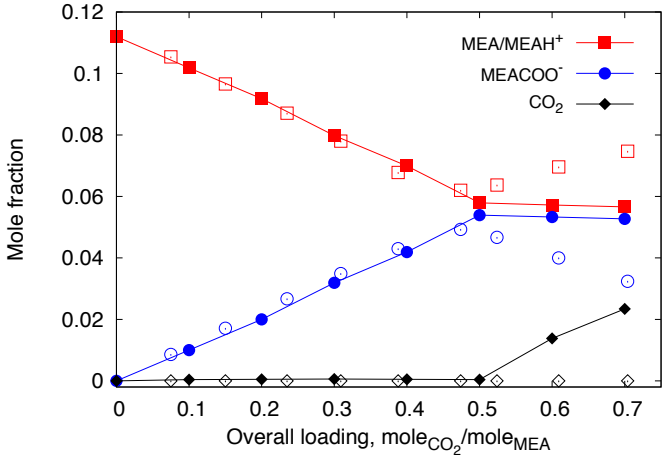


Figure 4.1: The mole fractions of the different species MEA/MEAH$^+$ (squares), MEACOO$^-$ (circles), $CO_2$ (diamonds) and $HCO_3^-$ (triangles) for 30 wt. % aqueous MEA solutions at $T = 293$ K. The open symbols are results from experiments [160]. The closed symbols are the results obtained from the RxMC/CFC simulations (a) including reactions R1-R4 (b) including only reaction R5. The lines are a guide to the eye.

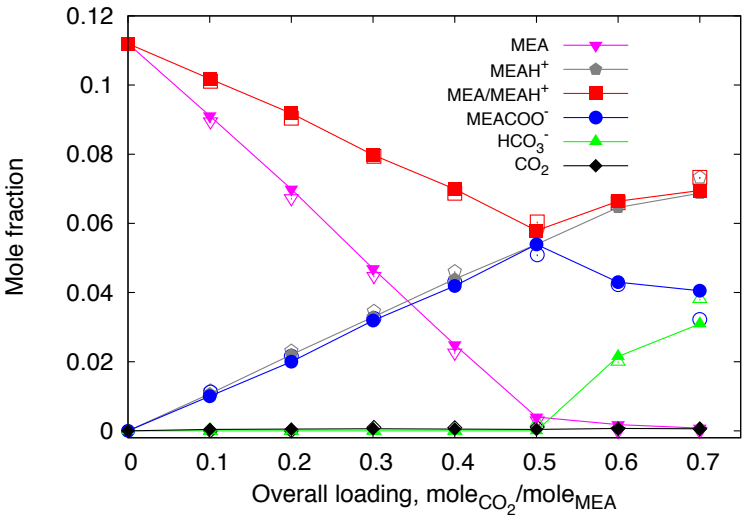


Figure 4.2: The mole fractions of the different species MEA (inverted triangles), $MEAH^+$ (pentagons), $MEA/MEAH^+$ (squares), $MEACOO^-$ (circles), $CO_2$ (diamonds), $HCO_3^-$ (triangles) for 30 wt. % aqueous MEA solutions at $T = 293$ K. The open symbols are results from the thermodynamic model combined with experimental data [160]. The closed symbols are results obtained from the RxMC/CFC simulations including reactions R1-R4. The lines are a guide to the eye.

(a)

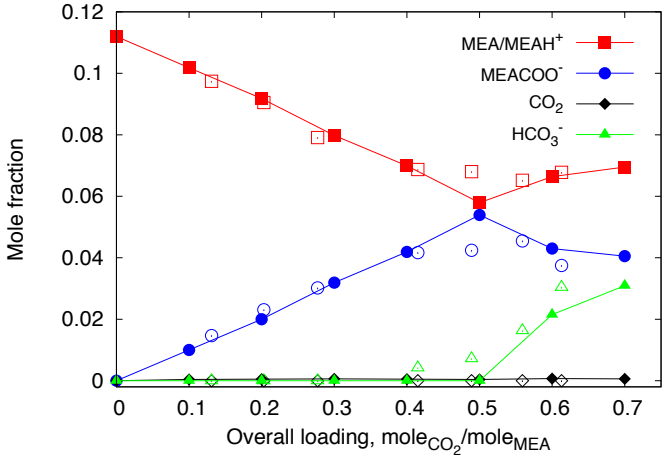


(b)

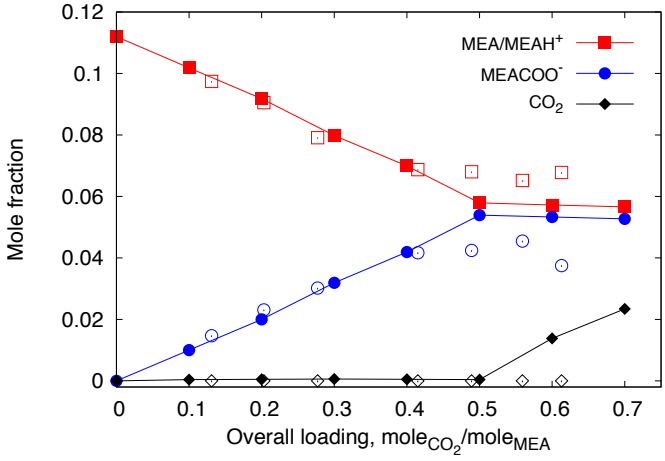


Figure 4.3: The mole fractions of the different species MEA/MEAH$^+$ (squares), MEACOO$^-$ (circles), $CO_2$ (diamonds) and $HCO_3^-$ (triangles) for 30 wt. % aqueous MEA solutions at $T = 333$ K. The open symbols are results from experiments [160]. The closed symbols are the results obtained from the RxMC/CFC simulations (a) including reactions R1-R4 (b) including only reaction R5. The lines are a guide to the eye.

(a)

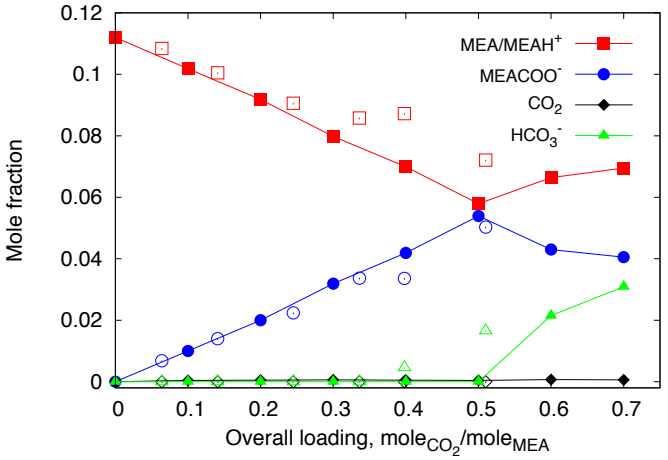


(b)

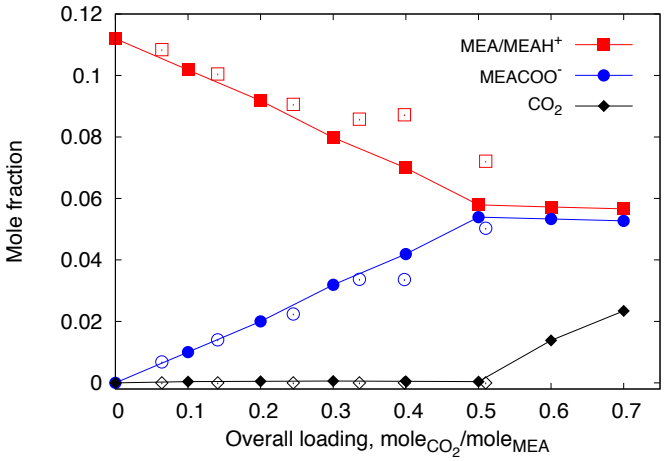


Figure 4.4: The mole fractions of the different species $MEA/MEAH^+$ (squares), $MEACOO^-$ (circles), $CO_2$ (diamonds) and $HCO_3^-$ (triangles) for 30 wt. % aqueous MEA solutions at $T = 353$ K. The open symbols are results from experiments [160]. The closed symbols are the results obtained from the RxMC/CFC simulations (a) including reactions R1-R4 (b) including only reaction R5. The lines are a guide to the eye.

### 4.4.3. Solubility of $CO_2$ in Aqueous MEA Solutions

Reactions R1-R4 are used to compute the solubility of $CO_2$ in aqueous MEA solutions by combining the RxMC/CFC method with the osmotic ensemble. Fig. 4.5 shows a schematic representation of how the chemisorption process is modeled in our simulations. The liquid phase consists of a MEA-$H_2O$ solution. $CO_2$ is present in the gas phase. The $CO_2$ is absorbed/desorbed in the MEA-$H_2O$ system which is modeled using the CFCMC method in the osmotic ensemble. The chemical reaction of the $CO_2$ molecules with the MEA and $H_2O$ molecules in the liquid phase is modeled using the RxMC/CFC algorithm. Both the absorption/desorption and the reaction take place simultaneously. Fig. 4.6 shows the absorption isotherms of $CO_2$ in aqueous MEA solutions at temperatures $T = 313$ K and 333 K. The simulation results agree excellently with the experimental results from Jou *et al.* [31] for the same system. The loading of $CO_2$ in aqueous MEA solvent increases as the partial pressure of $CO_2$ increases. The absorption/desorption as well as the reaction of $CO_2$ with MEA and $H_2O$ molecules take place simultaneously. As the $CO_2$ is absorbed from the gas phase, reactions of these absorbed molecules take place thereby paving way for more $CO_2$ to be absorbed in the liquid phase. The absorption isotherms of $CO_2$ in pure water at 313 K calculated from experiments by Wiebe *et al.* [185] are also plotted in Fig. 4.6. It can be observed that the physical solubility of $CO_2$ in pure water is very low and the chemisorption of $CO_2$ in aqueous MEA solution is high. This confirms that the reaction of $CO_2$ molecules with MEA and $H_2O$ molecules contributes largely to the increased solubilities and that reactions are necessary to achieve high solubilities.

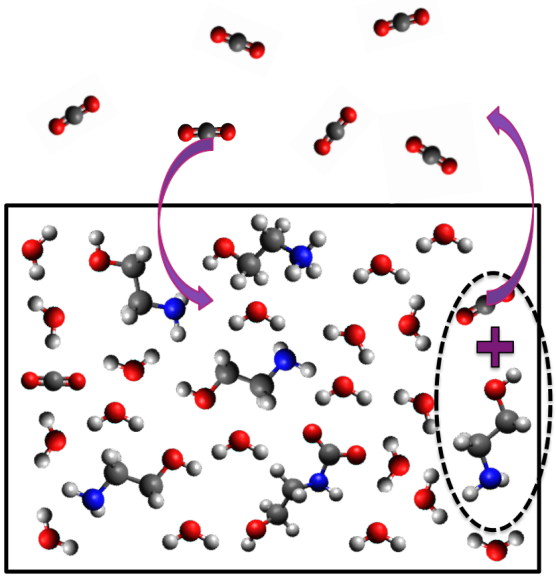

Figure 4.5: Schematic representation of the chemisorption of $CO_2$ molecules in a MEA-$H_2O$ system. Absorption/desorption of the $CO_2$ molecules in the gas phase into the liquid phase is simulated using the CFCMC method in the osmotic ensemble while the reaction of the $CO_2$ molecules with MEA and $H_2O$ in the liquid phase is simulated using the RxMC/CFC method. Both these processes are simulated simultaneously.

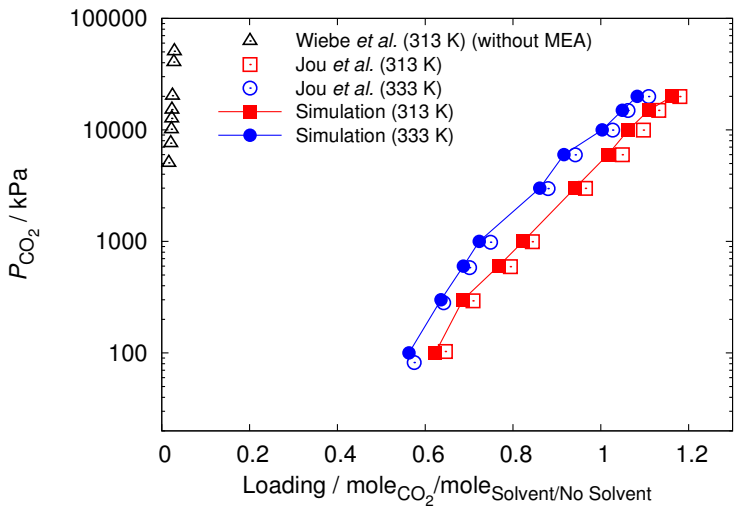


Figure 4.6: The solubility of $CO_2$ in aqueous MEA solutions at $T$ = 313 K and 333 K. The results from simulation are denoted by closed squares and circles and the results from experiments [31] are denoted by open squares and circles. The open triangles represent the results of solubility of $CO_2$ in $H_2O$ at $T$ = 313 K without MEA [185]. The lines are a guide to the eye.

## 4.5 Conclusions

Monte Carlo simulations in the Reaction Ensemble using a Continuous Fractional Component method provide an excellent description of the equilibrium concentrations of all relevant species in the chemisorption of $CO_2$ in MEA water solutions. Monte Carlo simulations using the Continuous Fractional Component method in the osmotic ensemble computes the absorption isotherms of $CO_2$ in the aqueous MEA solutions. The simulations were performed at different temperatures and the results from simulation are in excellent agreement with the experimental results. Equilibrium concentrations of MEA, $MEAH^+$, $MEACOO^-$, $CO_2$ from Reactions R1-R4 and R5 are identical for loadings up to 0.5 mole $CO_2$/mole MEA and beyond that, they are different. To obtain the accurate results for loadings in excess of 0.5 mole $CO_2$/mole MEA, reactions R1-R4 must be included in the simulation. This RxMC/CFC methodology opens up possibilities to investigate the effect of the solvents in the reactions by only considering the thermodynamics and ignoring transition states or reaction pathways. Solubility of $CO_2$ in aqueous MEA solution is also computed by combining the CFCMC method in the osmotic ensemble (which models the absorption/desorption) and the RxMC/CFC method (which models the reaction). The solubilities of $CO_2$ in aqueous MEA solvent computed from simulations agree excellently with those calculated from experiments. A comparison with the physisorption of $CO_2$ in pure water shows that the chemisorption of $CO_2$ in aqueous MEA solvent is much higher than physisorption, thereby confirming the theory that reactions are necessary to achieve high solubilities. This method may also be used to investigate the effect of the chemistry of the amines, for example by adding different functional groups [164, 165].

# 5

# Validation of the $CO_2/N_2O$ Analogy

This chapter is based on the publication: Q. Chen, S.P. Balaji, M. Ramdin, J.J. Gutierrez-Sevillano, A. Bardow, E. Goetheer, T.J.H. Vlugt, *Validation of the $CO_2/N_2O$ Analogy Using Molecular Simulation*, Ind. Eng. Chem. Res. **2014**, 53, 18081-18090 [71]

## 5.1 Introduction

As a byproduct of burning fossil fuel, carbon dioxide ($CO_2$) accounts for a large portion of the greenhouse gas emissions [155, 156]. $CO_2$ capture and storage (CCS) could play a significant role in reducing $CO_2$ emissions from the power plants [25, 157, 186]. The removal of $CO_2$ from natural gas or in the post-combustion process is typically achieved in an absorber using an amine solution [8, 159, 187]. For example, an aqueous solution containing 30% monoethanolamine (MEA) is a frequently used solvent for $CO_2$ capture [159]. For a proper design of a gas absorption unit, it is very important to understand the mass-transfer process of $CO_2$. This requires knowledge of the solubility and diffusivity of $CO_2$ in aqueous amine solutions. Due to reactions between $CO_2$ and amines, the solubility of $CO_2$ measured in experiments is the total solubility, which combines both physical and chemical absorption. However, the physical solubility is needed to obtain the rate of the $CO_2$ absorption [188]. When the $CO_2$ molecules absorb into an amine solvent, diffusion and reaction will take place simultaneously. As there is almost no unreacted $CO_2$, it is practically impossible to obtain the solubility and diffusivity of $CO_2$ in amine solutions directly from experiments [39, 82]. In practice, this problem is usually overcome by substituting $CO_2$ with a similar but inert gas. Nitrous oxide ($N_2O$) can be considered as an ideal candidate since both gases have a similar molecular weight, volume and structure. Substituting $CO_2$ for $N_2O$ to obtain physical properties of $CO_2$ is known as "the $CO_2/N_2O$ analogy". According to the $CO_2/N_2O$ analogy, the solubility and diffusivity of both gases are related by [33]:



$$\left[\frac{H_{CO_2}}{H_{N_2O}}\right]_{\text{in water}} = \left[\frac{H_{CO_2}}{H_{N_2O}}\right]_{\text{in amine solution}} \tag{5.1}$$

$$\left[\frac{D_{CO_2}}{D_{N_2O}}\right]_{\text{in water}} = \left[\frac{D_{CO_2}}{D_{N_2O}}\right]_{\text{in amine solution}} \tag{5.2}$$

where $H$ is the Henry coefficient and $D$ is the self-diffusivity.

The idea of the $CO_2/N_2O$ analogy was first conceived by Clarke [32] who studied the absorption kinetics of $CO_2$ in aqueous MEA solutions at short contact times using the laminar liquid jet technique. In this study, it was suggested that the solubility and diffusivity of $CO_2$ in MEA solutions are comparable to those of $N_2O$ due to the similarity in their mass and molecular interactions. Joosten and Danckwerts [189] presented experimental data on the solubility and diffusivity of $N_2O$ in equimolar potassium-potassium bicarbonate solutions of various ionic strengths. These authors indicated that the corresponding properties of $CO_2$ can be reliably predicted by these $N_2O$ data. Joosten and Danckwerts showed that the diffusivities of $CO_2$ and $N_2O$ in a pure liquid and an electrolyte solution are correlated by [189]:

$$\left[\frac{D_{\text{soln}}}{D_{\text{o}}}\right]_{CO_2} = \left[\frac{D_{\text{soln}}}{D_{\text{o}}}\right]_{N_2O} \tag{5.3}$$

where $D_{\text{o}}$ and $D_{\text{soln}}$ are the diffusivity of $CO_2$ or $N_2O$ in a pure solvent and an electrolyte solution, respectively. This method was later used by Sada *et al.* [190, 191], who applied it to a variety of aqueous amine solutions. Sada *et al.* also showed

that the solubilities of $CO_2$ and $N_2O$ in water and an amine solution are correlated by:

$$\log\left[\frac{H}{H_w}\right]_{CO_2} = \log\left[\frac{H}{H_w}\right]_{N_2O} \tag{5.4}$$

where $H_w$ and $H$ are the Henry coefficient of $CO_2$ or $N_2O$ in water and an amine solution, respectively. Laddha and co-workers [192] improved the analogy in a more quantitative way. These authors showed that the ratio of the solubility of $CO_2$ to that of $N_2O$ in pure water between 288 K and 303 K is 1.37 (within 2% error). Laddha *et al.* [192] examined several solutions of alcohols (glycol, 1-propanol, glycerol, 1,5-pentanediol and diethylene glycol) which have a similar structure as MEA or diethanolamine (DEA), but do not react with the solutes. The results suggested that the analogy of Eq. (5.1) may be valid for alkanolamine solutions. Haimour and Sandall [39] measured the $CO_2$ absorption rate in aqueous methyldiethanolamine (MDEA) in a laminar liquid jet apparatus. For very short absorption times ($< 0.012$ s) of the absorption experiments, it was assumed that any reaction between $CO_2$ and MDEA has little effect on the absorption rate. From the experimental results, they confirmed that the analogy holds for aqueous MDEA solutions. With the aid of the $CO_2/N_2O$ analogy, Versteeg and van Swaaij [82] conducted a systematic study on both the solubility and diffusivity of $CO_2$ and $N_2O$ in several aqueous alkanolamine solutions over a wide range of temperatures. The study also provided a general correlation of both the diffusivity and solubility of $CO_2$ and $N_2O$ in water as a function of temperature. The $CO_2/N_2O$ analogy has been extensively applied to estimate the properties of $CO_2$ in aqueous amine solutions [33, 38, 40–43, 82, 193]. For example, the $CO_2/N_2O$ analogy was used to estimate the solubility and diffusivity of $CO_2$ in the aqueous solutions of MEA [193], DEA [82, 193], MDEA [40, 82, 193], Diisopropanolamine (DIPA) [82], Dimethylmonoethanolamine (DMMEA) [82], 2-Amino-2-methyl-1-propanol (AMP) [42, 43], and Piperazine (PZ) [41]. The analogy was also applied to aqueous solutions of amine mixtures (*e.g.* MEA+MDEA [33], DEA+MDEA [38]).

Although the $CO_2/N_2O$ analogy is often used, it still has an empirical nature. Experiments are unable to verify this analogy due to reactions between $CO_2$ and the amine [33, 43, 82, 193]. As a result, a different approach is required to test the validity of the analogy. Molecular simulation is a powerful tool to predict the properties of substances and materials using the interactions between atoms and molecules [53]. The advantage of molecular simulations, unlike in experiments, is that the reactions between $CO_2$ and amine can be "switched off". This essentially means that in simulations a direct measurement of the physical solubility and diffusivity of $CO_2$ in an aqueous amine solvent is possible. To the best of our knowledge, molecular simulation is the only way to really make sure that $CO_2$ does not react with the amine molecules. Consequently, this analogy could be validated with the simulation results of the solubility and diffusivity for both gases in water and amine solutions. Nevertheless, simulation data on the solubility and diffusivity of $CO_2$ and $N_2O$ is limited in the open literature. The Henry coefficients of $CO_2$ and $N_2O$ can be obtained from molecular simulations using an ensemble in which the number

of molecules fluctuates [70]. This can be realized by adding/removing molecules to/from a so-called open system. A system where the number of molecules fluctuates is called an open system. The conventional Monte Carlo schemes are inefficient since they suffer from the low insertion/deletion acceptance probabilities at high densities [77, 194]. Therefore, methods that can handle open systems at high densities are required to efficiently compute the Henry coefficients. Lísal *et al.* [195] obtained the Henry coefficients for $CO_2$ in water via the Widom test-particle insertion method and the staged free-energy perturbation method. These authors also compared different interaction models of water and $CO_2$. Cichowski *et al.* [196] determined the Henry coefficient of $CO_2$ in ethanol by transition matrix Monte Carlo simulations coupled with the expanded ensemble technique. A similar study on the $CO_2$ solubility in ethanol was carried out by Zhang and Siepmann [197], who used Gibbs ensemble Monte Carlo simulations to directly calculate the Henry coefficient. The Continuous Fractional Component Monte Carlo (CFCMC) method was recently developed by Shi and Maginn [78, 79, 194, 198]. This method overcomes the difficulties encountered in conventional MC methods by utilizing gradual insertions/deletions of molecules using a continuous coupling parameter and an adaptive bias potential. The CFCMC method in the osmotic ensemble was applied to obtain the Henry coefficients of $CO_2$ in ethanol and the results are in agreement with previous studies [78].



Self-diffusivities of the absorbed $CO_2$ and $N_2O$ can be computed by equilibrium Molecular Dynamics (MD) simulations [92]. This approach requires interaction potential models capable of accurately describing the intermolecular and intramolecular interactions of the molecules. Some efforts were made to investigate the influence of different force fields on the diffusion coefficient. In het Panhuis *et al.* [199] used the SPC/E model for water and adjusted the Lennard-Jones size parameters and quadruple moments (partial charges) of the Gromos $CO_2$ potential. This work concluded that whereas the Lennard-Jones interaction of the $CO_2$ potential has a large impact on the $CO_2$ diffusion behavior, the diffusivity of $CO_2$ is almost independent of the Coulombic interaction of the $CO_2$ potential. Vlcek *et al.* [200] proposed and applied a coupling parameter scheme to optimize the Lennard-Jones cross interactions for the SPC/E-EPM2 models. This successfully improved the accuracy of the predicted mutual diffusion coefficients of $CO_2$ and water in simulations. Zeebe [201] presented studies on the diffusivity of dissolved $CO_2$ in water over a temperature range from 273 to 373 K and provided a general power-law equation to predict the diffusivity of $CO_2$ as a function of temperature. Recently, Moultos *et al.* [202] compared different combinations of $CO_2$ and water models to investigate the diffusivity of $CO_2$ over a broad range of temperatures and pressures. These authors found that at normal pressure the TIP4P/2005-EPM2 combination was best to calculate the diffusivity of $CO_2$ at lower temperatures ($< 323.15$ K), while the SPC/E-TraPPE combination performs best at higher temperatures. Overall, the simulation data on the solubility and diffusivity of $CO_2$ in amine solutions are lacking. To the best of our knowledge, very limited research has been conducted on the absorption rates and transport properties of $N_2O$ in solvents.

Here, we compute the Henry coefficient and self-diffusivity of $CO_2$ and $N_2O$ in a variety of solvents using molecular simulation. The investigated solvents include water, ethanol, *n*-heptane, and a 30% MEA solution. The reason for choosing ethanol and heptane is to investigate how solvents with different polarities influence the solubility and diffusivity for $CO_2$ and $N_2O$. The focus of the chapter is to validate the $CO_2/N_2O$ analogy using molecular simulation. Section 5.2 outlines the simulation details including the different force fields for $CO_2$ and $H_2O$ and the simulation methods (CFCMC and MD). In section 5.3, the simulation results on the Henry coefficients and self-diffusivities of $CO_2$ and $N_2O$ are presented and discussed. Our findings are summarized in section 5.4.

## 5.2 Simulation Details

For computing the Henry coefficient, the Continuous Fractional Component Monte Carlo (CFCMC) method in the osmotic ensemble was used. All MC simulations were performed using the molecular simulation package RASPA [117]. In the osmotic ensemble, the total hydrostatic pressure ($P$), the temperature ($T$), the fugacity of the gas phase ($f$), and the number of (nonvolatile) solvent molecules ($N$) are kept constant. The volume of the simulation box and the number of solute molecules in the liquid phase will change due to the imposed hydrostatic pressure. The fugacity of the gases directly corresponds to the pressure of the gas phase which is identical to the hydrostatic pressure in the liquid. The Peng-Robinson (PR) equation of state (EoS) was used to calculate the fugacity of the gas phase as a function of the pressure [203]. Details on the CFCMC method can be found in section 3.2.2. The CFCMC simulations were performed at a temperature of 303 K and a series of pressures was selected to compute the Henry coefficient of the solute. The reason for choosing 303 K is the availability of experimental data at this temperature for 30% MEA (w/w) solutions, which makes a straightforward comparison with the simulation results possible [33]. Ensembles of 500 water molecules, 250 ethanol molecules, 250 heptane molecules, and 56 MEA with 444 water molecules were used respectively in the simulations for the different systems. For water, the three-site rigid model SPC/E [204], the four-site rigid model TIP4P [59], and the five-site rigid model TIP5P [60] were used. These models were also used by other researchers [195] so that a direct comparison of the $CO_2$ solubility can be made. The TraPPE model developed by Siepmann's group was adopted for ethanol [61] and *n*-heptane [62]. The OPLS all-atom force field [58] was used for MEA. The force field for $CO_2$ was taken from the TraPPE [181] and EPM2 [205] models; the $N_2O$ model was developed by Lachet *et al.* [206]. The Lennard-Jones parameters for the cross interactions were obtained from the Lorentz-Berthelot combining rules [207]. The Ewald summation [208] with a relative precision of $10^{-5}$ was used to calculate the long range electrostatic interactions. The LJ interactions were truncated and shifted at 12 Å and no tail corrections were applied. All CFCMC simulations were initiated with an equilibration run of 50000 MC cycles, followed by a production run of at least 200000 MC cycles, where the number of MC steps in a cycle equals the total number of molecules in the simulation box. The average number of solute molecules was sampled to calculate the Henry coefficient. The reported data were

obtained from the block averages [70], and the standard deviation was used to calculate the uncertainty.

The self-diffusivity was computed by Molecular Dynamics (MD) simulation. The simulations were executed with the MD package GROMACS version 4.6.5 [209]. The initial configuration of the molecules was generated by the Avogadro software package [210]. Due to the low solubility of the solute, only one $CO_2$ or $N_2O$ molecule was placed in the simulation box. The system sizes were chosen from three different simulation boxes consisting of 500 water molecules, 1000 water molecules, and 2000 water molecules, respectively. The force fields used in the MD simulations were the same as those used in the MC simulations. The Lorentz-Berthelot mixing rules were adopted for the LJ interactions [207]. After generating initial atomic positions, the energy of each system was minimized using the steepest descent algorithm. The system was then equilibrated in the NPT ensemble at a pressure of 1 bar and 303 K by the Parrinello-Rahman barostat and the Nosé-Hoover thermostat, respectively. When the system properties showed no variation in time, the average density was computed. Production runs were started using the average density of the NPT simulations. The production runs were carried out in the NVT ensemble at a temperature of 303 K for at least 20 ns and at least 50 simulations were executed in parallel to reduce the error bar of the computed self-diffusivities. We verified that our simulations were sufficiently large. The leap-frog algorithm was used to integrate the equations of motion. Electrostatic interactions were handled by the Particle-Mesh Ewald algorithm [208]. An integration time step of 2 fs was used. Three-dimensional periodic boundary conditions were applied to the cubic simulation boxes to obtain the properties of a bulk system.



It is important to note that the above mentioned simulations do not take into account a reaction between $CO_2$ and the amine. However, we would like to understand whether or not the reaction of $CO_2$ with amine will have an impact on the physical solubility and diffusivity of $CO_2$. For this purpose, a fully reacted system was set up in which all the MEA molecules have already reacted with $CO_2$. $CO_2$ reacts with a primary amine (*e.g.* MEA) by a zwitterion mechanism [211] to form carbamates:

$$CO_2 + 2RNH_2 \rightleftharpoons RNHCOO^- + RNH_3^+ \qquad \text{(R1)}$$

In case of monoethanolamine (MEA), R = $CH_2CH_2OH$. In a fully reacted system, amine molecules are present either as a carbamate ion ($HOCH_2CH_2NHCOO^-$) or as an amine ion ($HOCH_2CH_2NH_3^+$). The force fields for these two reaction product ions were derived from the OPLS all-atom parameters [144]. However, the OPLS force field cannot adequately describe the electronic partial charges of the individual atoms of these two ions $HOCH_2CH_2NHCOO^-$ and $HOCH_2CH_2NH_3^+$, as the charges of the ions do not sum up to $-1$ and $+1$ respectively. To accurately describe the physical solubilities and diffusivities of $CO_2$ and $N_2O$ in a fully reacted system, the partial charges for $HOCH_2CH_2NHCOO^-$ and $HOCH_2CH_2NH_3^+$ were derived by performing DFT quantum chemical simulations. The GAUSSIAN 09 quantum chemical simulation program was used [177]. MP2 optimization was used and the basis set used for deriving the Mulliken charges was 6-311+G(2d,2p). After the

structures were initialized to their lowest energy conformers, the Mulliken partial charges were calculated. The values of the partial charges can be found in the Supplementary Information of Ref. [71]. The validity of the partial charges has been verified by calculating the density of a fully reacted MEA solution (*i.e.* a solution where all the MEA has reacted with $CO_2$ to form the two reaction ions). The densities obtained from the simulations using the partial charges computed from DFT quantum chemical simulations are in good agreement with the densities calculated from experiments [212] suggesting that the used partial charges are reasonable. The $CO_2$ physical solubility and diffusivity in both non-reacted and fully reacted amine systems is considered next. The CPU time required to compute the solubilities and diffusivities ranged from 3-4 weeks in total for the equilibration and production runs using state-of-the-art computation facilities.

## 5.3 Results and Discussion

### 5.3.1. Solubility



By definition, the Henry coefficient of a given gas of type $i$ can be obtained from the following equation [197, 213]:

$$H_i = \lim_{x_i \to 0} \frac{f_i^{\text{gas}}}{x_i^{\text{liq}}} \tag{5.5}$$

where $f_i^{\text{gas}}$ denotes the fugacity of the solute $i$ in the gas phase and $x_i^{\text{liq}}$ represents the mole fraction of the solute $i$ in the liquid phase. Fugacities and Henry coefficients are reported in units of MPa [214]. A total number of 500 water molecules were used in the simulation box and the average density has been tested for SPC/E model. The average density of SPC/E water computed from simulations in the NPT ensemble at 303 K and 1 bar is $0.9947 \pm 0.0015$ g/cm$^3$, which is in good agreement with the experimental data 0.9957 g/cm$^3$ [215]. Consequently, 500 water molecules were used as the solvent in all ensembles. Different models for water and $CO_2$ were compared. We have used three models (SPC/E, TIP4P and TIP5P) for water and two models (EPM2 and TraPPE) for $CO_2$, which yields a total of six combinations. In Fig. 5.1, the fugacity of $CO_2$ in the gas phase is plotted as a function of the solute mole fraction of the solvent.

The uncertainty in the mole fraction is calculated from the block averages and is typically below 0.002. The Henry coefficients for the six $CO_2$-$H_2O$ systems using the different models are reported in Table 5.1. Almost all the models except TIP5P-TraPPE overpredict the experimental data. The combination of TIP5P-TraPPE can be considered as the best one to predict the $CO_2$ solubility in water. A comparison of the different water models shows that the TIP5P model performs better than the TIP4P and SPC/E model. The computed Henry coefficients of $CO_2$ in TIP5P water are much closer to the experimental data. This finding is consistent with the simulation work conducted by Lísal *et al.* [195]. For $CO_2$, the TraPPE model performs much better than the EPM2 model when combined with the three water models. This indicates the importance of force field parameters for computing solubilities. The same MC simulations were performed for $N_2O$ in water using one

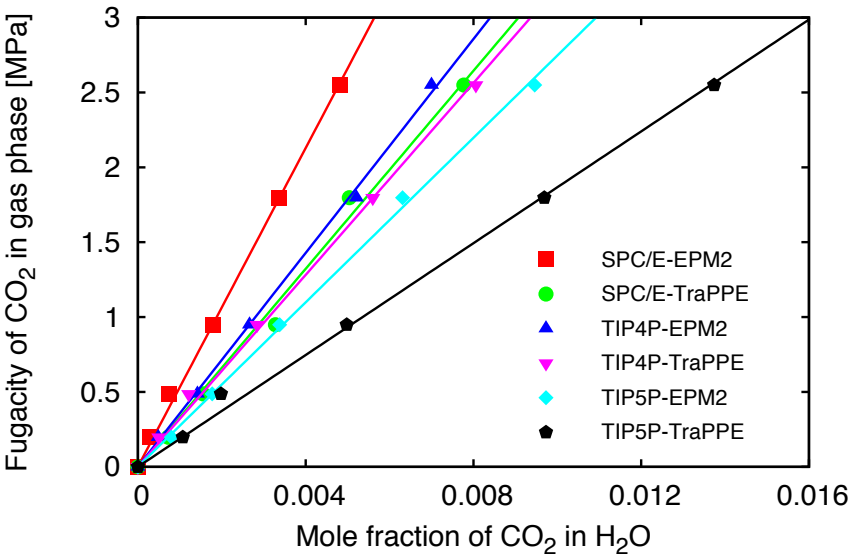


Figure 5.1: Fugacity of $CO_2$ in the gas phase plotted as a function of mole fraction of $CO_2$ in water at 303 K. The SPC/E, TIP4P and TIP5P models were used for water; the EPM2 and TraPPE models were used for $CO_2$. Six different combinations were investigated.

model for $N_2O$ (developed by Lachet *et al.* [206]) and different models for water (*i.e.* SPC/E, TIP4P and TIP5P).

The Henry coefficients for the $N_2O$-$H_2O$ systems are also listed in Table 5.1. A similar conclusion can be drawn for the performance of the water models, as the solubility of $N_2O$ in TIP5P water is the closest to the experimental value [33, 82]. When only the $CO_2$ TraPPE model is taken into consideration, the Henry coefficient for $CO_2$ in the same water model is always lower than that for $N_2O$, which is consistent with the experiments. The differences between simulations and experiments for $CO_2$(TraPPE)-$H_2O$(TIP5P) and $N_2O$-$H_2O$(TIP5P) systems are rather small (2.7% and 3.8%, respectively), which shows that these two model combinations can accurately predict the Henry coefficients of $CO_2$ and $N_2O$ at 303 K.

Additional simulations were performed to compute the Henry coefficient of $CO_2$ and $N_2O$ in the solvents ethanol and *n*-heptane. In these simulations for the $CO_2$ and $N_2O$ solubility, ensembles of 250 ethanol molecules, and 250 *n*-heptane molecules were used. In Fig. 5.2, the fugacity of $CO_2$ and $N_2O$ in the gas phase is plotted as a function of the solute mole fraction in solution.

By extrapolating to low pressures, the Henry coefficient can be obtained. As shown in Table 5.1, all the simulation results for the Henry coefficients of $CO_2$ and $N_2O$ in ethanol and *n*-heptane underestimate the experimental values. To the best of our knowledge, experimental data for the Henry coefficients of $CO_2$ and $N_2O$ in ethanol have been reported only at 293 K as 16.28 MPa and 13.72 MPa,

Table 5.1: Computed Henry coefficients of $CO_2$ and $N_2O$ in water, ethanol, $n$-heptane, and a 30% MEA solution at 303 K are compared to the experimental data. Different models for $H_2O$ (SPC/E, TIP4P and TIP5P) and $CO_2$ (EPM2 and TraPPE) were used. No available data on Henry coefficient for $CO_2/N_2O$ in ethanol at 303 K have been reported. The Henry coefficient of $CO_2$ in ethanol was only reported at other temperatures (*e.g.* 293 K [40]).

| Solute | Solvent | $H_{\mathbf{sim}}$ [MPa] | $H_{\mathbf{exp}}$ [MPa] | Difference |
|---|---|---|---|---|
| $CO_2$ (EPM2) | $H_2O$ (SPC/E) | 520.6 ± 15.8 | 187.9 [33] | +177% |
| $CO_2$ (TraPPE) | $H_2O$ (SPC/E) | 336.6 ± 17.0 | 187.9 [33] | +79% |
| $N_2O$ | $H_2O$ (SPC/E) | 471.9 ± 31.1 | 244.8 [33] | +93% |
| $CO_2$ (EPM2) | $H_2O$ (TIP4P) | 357.6 ± 8.0 | 187.9 [33] | +90% |
| $CO_2$ (TraPPE) | $H_2O$ (TIP4P) | 311.6 ± 7.0 | 187.9 [33] | +66% |
| $N_2O$ | $H_2O$ (TIP4P) | 438.3 ± 5.6 | 244.8 [33] | +79% |
| $CO_2$ (EPM2) | $H_2O$ (TIP5P) | 273.7 ± 5.2 | 187.9 [33] | +46% |
| $CO_2$ (TraPPE) | $H_2O$ (TIP5P) | 182.8 ± 4.2 | 187.9 [33] | −2.7% |
| $N_2O$ | $H_2O$ (TIP5P) | 235.5 ± 2.3 | 244.8 [33] | −3.8% |
| $CO_2$ (EPM2) | ethanol | 13.10 ± 0.20 | n/a | n/a |
| $CO_2$ (TraPPE) | ethanol | 12.43 ± 0.28 | n/a | n/a |
| $N_2O$ | ethanol | 11.24 ± 0.40 | n/a | n/a |
| $CO_2$ (EPM2) | heptane | 4.545 ± 0.053 | 8.859 [216] | −49% |
| $CO_2$ (TraPPE) | heptane | 4.616 ± 0.074 | 8.859 [216] | −48% |
| $N_2O$ | heptane | 4.402 ± 0.039 | 6.026 [217] | −27% |
| $CO_2$ (TraPPE) | MEA solution (TIP4P) | 155.6 ± 2.1 | n/a | n/a |
| $N_2O$ | MEA solution (TIP4P) | 190.2 ± 3.7 | 141.6 [33] | +34% |
| $CO_2$ (TraPPE) | MEA solution (TIP5P) | 92.29 ± 1.88 | n/a | n/a |
| $N_2O$ | MEA solution (TIP5P) | 110.7 ± 4.5 | 141.6 [33] | −22% |



respectively [40]. The two models of $CO_2$ (EPM2 and TraPPE) in ethanol and heptane, unlike in water, result in Henry coefficients that are very similar. The Henry coefficient of $N_2O$ is always lower than that of $CO_2$ in both ethanol and heptane. Note that the solubility is higher when the Henry coefficient is lower. This trend for ethanol was also observed in the work by Kierzkowska-Pawlak *et al.* [40], although their experiments were conducted at 293 K. Finally, we performed simulations for the $CO_2$ and $N_2O$ solubility in a 30% (w/w) MEA solution. Note that at this stage the reactions between $CO_2$ and MEA have been "switched-off" in the MC simulations. In a subsequent section a case will be presented where the reactions between $CO_2$ and MEA have been taken into consideration. Based on our results of $CO_2$ solubility in water, we only used the TIP4P and TIP5P models for water and the TraPPE model for $CO_2$. The results are shown in Fig. 5.3 and Table 5.1.

Although a certain deviation from the experiment can be observed, the simulation data show that 30% MEA solution is capable of physically absorbing more $CO_2$ molecules than $N_2O$. The difference between simulations and experiments can be attributed to the used force field, but the simulation results are acceptable considering that all force field parameters were taken directly from existing literature. Moreover, the MC simulations correctly predict the experimental solubility trend. A comparison of the Henry coefficient for $CO_2$ or $N_2O$ in various solvents shows that the solubility obeys the following order: heptane > ethanol > 30% MEA aque-

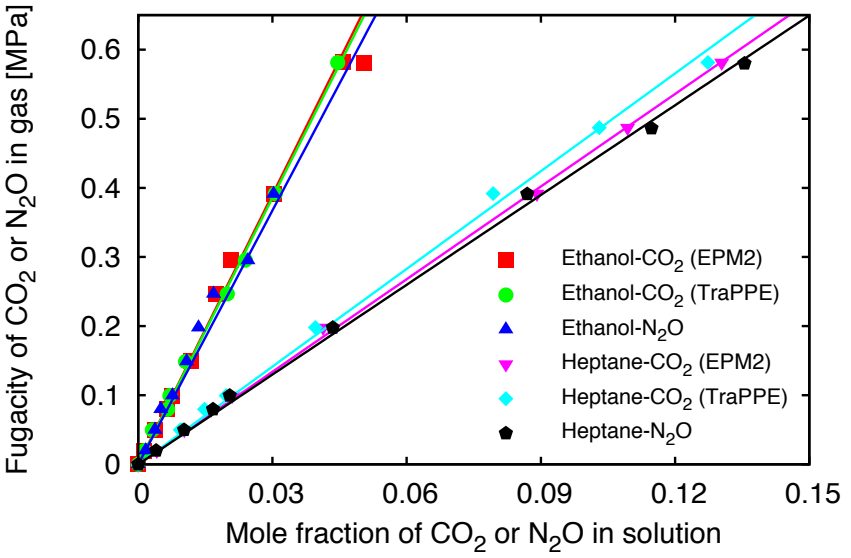


Figure 5.2: The fugacity of $CO_2$ in the gas phase plotted as a function of mole fraction of $CO_2/N_2O$ in ethanol and $n$-heptane at 303 K. The EPM2 and TraPPE models were used for $CO_2$.

ous solution > water. To validate the $CO_2/N_2O$ analogy, the ratios of the Henry coefficients of $CO_2$ and $N_2O$ in all investigated solvents were obtained. As listed in Table 5.2, the $CO_2/N_2O$ ratios for water and MEA solution are all below unity while the $CO_2/N_2O$ ratios for ethanol and heptane are both above unity.

The differences between simulations and experiments for the $CO_2/N_2O$ Henry coefficient are below 10% for the TIP4P and TIP5P water models, but for heptane the difference is nearly 30%. The explanation could be that the experimental ratio for heptane is in fact calculated from data of two different studies [216, 217]. For solvents with larger dipole moments (*e.g.* water), more $CO_2$ molecules are likely to be absorbed. Solvents with smaller dipole moments (*e.g.* heptane) tend to absorb more $N_2O$ molecules. The validity of Eq. (5.1) can be verified by comparing the $CO_2/N_2O$ ratio for the Henry coefficient in water, and 30% MEA solution. Li and Lai [33] reported the ratio $H_{CO_2}/H_{N_2O}$ in water to be 0.77 at a temperature of 303 K and applied this ratio for calculating the Henry coefficient of $CO_2$ in amine solutions. We found that this ratio is in agreement with our simulation results, since all the data points for water and MEA solution fall within 10% of the value of 0.77. The $CO_2/N_2O$ analogy for Henry coefficient is therefore supported at a temperature of 303 K.

So far, all the MC simulations assume that $CO_2$ does not react with the MEA molecules; hence the solubility of $CO_2$ in the MEA solution was purely due to physisorption. In reality, $CO_2$ will react with MEA and it is therefore very im-

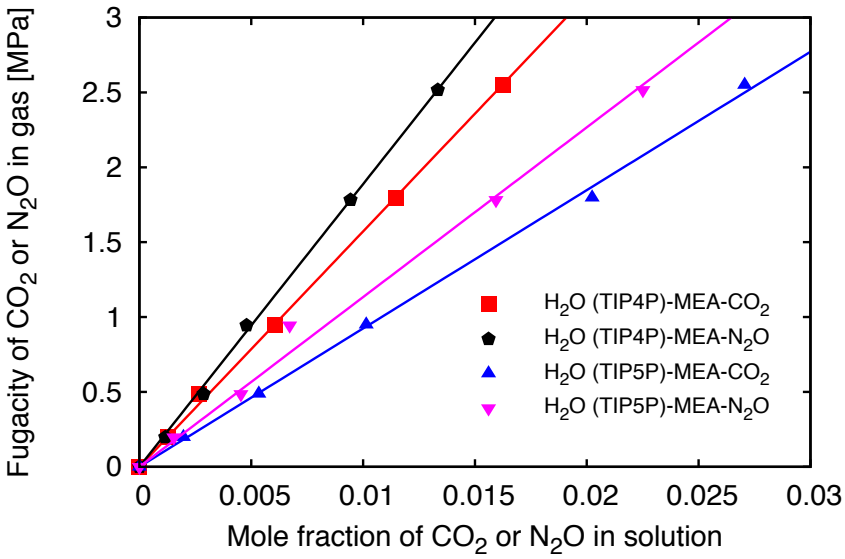


Figure 5.3: The fugacity of $CO_2$ or $N_2O$ in the gas phase plotted as a function of mole fraction of $CO_2/N_2O$ in 30% MEA solution at 303 K. The TraPPE model was used for $CO_2$. The TIP4P and TIP5P models were used for $H_2O$.

portant to understand how reactions or reaction products affect the Henry coefficients of $CO_2$ and $N_2O$. Assuming that all MEA molecules have been reacted with $CO_2$, a simulation of a fully-reacted system with 28 $HOCH_2CH_2NHCOO^-$ ions, 28 $HOCH_2CH_2NH_2^+$ ions and 444 water molecules was performed. In experiments, $CO_2$ can fully react with MEA molecules even at low temperatures (*e.g.* 293 K) [160]. At 303 K, the MC simulations were performed to compute the Henry coefficient of $CO_2$. The best performing combination for $CO_2$-$H_2O$ (TraPPE-TIP5P) was used. The Henry coefficient of free $CO_2$ in this fully reacted MEA solution is calculated to be 107.2 ± 5.6 MPa, while the Henry coefficient in the non-reacted MEA solution is 92.3 ± 1.9 MPa. This indicates that the Henry coefficient of the MEA solution increases when the reaction products are formed. In other words, the Henry coefficient of $CO_2$ is higher in an unreacted MEA solution than in a solution containing their reaction products. However, there is no huge impact of reaction products on the physical solubility of $CO_2$. As a result, the $CO_2/N_2O$ analogy for the physical solubility may also hold during the whole chemical reaction process.

Table 5.2: The ratio of Henry coefficients of $CO_2$ to $N_2O$ in water, ethanol, $n$-heptane, and a 30% MEA solution at a temperature of 303 K. Simulation results are compared with the experimental data reported with the difference presented. We only used the TraPPE model for $CO_2$ and the TIP4P/TIP5P model for $H_2O$ for comparison.

| Solvent | $[H_{CO_2}/H_{N_2O}]_{sim}$ | $[H_{CO_2}/H_{N_2O}]_{exp}$ | Difference |
|---|---|---|---|
| water (TIP4P) | 0.71 ± 0.02 | 0.77 [33] | −7.8% |
| water (TIP5P) | 0.78 ± 0.02 | 0.77 [33] | +1.3% |
| ethanol | 1.11 ± 0.05 | n/a | n/a |
| $n$-heptane | 1.05 ± 0.02 | 1.47 [216, 217] | −29% |
| 30% MEA (TIP4P) | 0.82 ± 0.02 | n/a | n/a |
| 30% MEA (TIP5P) | 0.84 ± 0.04 | n/a | n/a |

### 5.3.2. Diffusivity

The self-diffusivity of molecule $i$ was calculated from the Einstein's equation in three dimensions:

$$D_i = \frac{1}{6N_i} \lim_{m\to\infty} \frac{1}{m\Delta t} \sum_{l=1}^{N_i} \langle [r_{l,i}(t + m\Delta t) - r_{l,i}(t)]^2 \rangle \tag{5.6}$$

where $N_i$ is the total number of molecules of component $i$, $m$ is the number of time steps and $\Delta t$ is the time step used in MD simulations. $r_{l,i}$(t) is the position of the $l$-th molecule of type $i$ at time $t$ [88–92]. Moultos *et al.* [202] showed that the error bar of the $CO_2$ diffusivity in water is considerably large (> 10%). This accuracy is not suitable for the purpose of this study, because the diffusivity ratio of $CO_2$ and $N_2O$ will then have an even larger error bar and it will not be possible to obtain a value statistically different from unity. In this work, we carried out at least 50 parallel simulations, from which the statistical uncertainty was determined. An order-$n$ algorithm [218] was used to compute the Mean Squared Displacement (MSD). The average MSDs of $CO_2$ as a function of time for each simulation were plotted. In a log-log plot, the different distinct regimes can be observed. Before molecules collide with each other, they undergo ballistic diffusion, which occurs in a very short time (< 1 ps). After 10 ps, the regime on the log-log plot can be identified as Fickian diffusion. Since the solubility of $CO_2$ is relatively small in water, we first tested three different system sizes in which 1 $CO_2$ (EPM2) molecule was solvated in 500, 1000, and 2000 $H_2O$ (SPC/E) molecules, respectively. The self-diffusivities of $CO_2$ in 500, 1000 and 2000 water molecules were calculated as $(2.73 \pm 0.07) \times 10^{-9}$, $(2.75 \pm 0.08) \times 10^{-9}$ and $(2.78 \pm 0.07) \times 10^{-9}$ $m^2/s$, respectively. The results clearly indicate that the difference is less than 2%; namely, there is no significant difference in self-diffusivities for the three system sizes. The effect of the system size on the diffusivity of $CO_2$ in the other solvents was also investigated and again no notable differences could be observed for the different system sizes (results not shown). As for the solubility, a comparison of the performance for the different models for $H_2O$ with respect to the diffusivity is provided. Three water models (*i.e.* SPC/E, TIP4P and TIP5P) were tested using the EPM2 $CO_2$ model. From the diffusivity regime up to 20 ns, the diffusivity of $CO_2$ in the SPC/E, TIP4P, and TIP5P water was obtained as (2.73 ±

Table 5.3: The self-diffusivities of $CO_2$ in water, ethanol, $n$-heptane, and 30% MEA solution at 303 K. Simulation results are compared with the experimental data. The different models for $CO_2$ and water is also indicated.

| Solute | Solvent | $D_{\text{sim}}$ [$10^{-9}$m$^2$/s] | $D_{\text{exp}}$ [$10^{-9}$m$^2$/s] | Difference |
|---|---|---|---|---|
| $CO_2$ (EPM2) | water (SPC/E) | 2.73 ± 0.07 | 2.12 [33] | +29% |
| $CO_2$ (TraPPE) | water (SPC/E) | 2.76 ± 0.08 | 2.12 [33] | +30% |
| $N_2O$ | water (SPC/E) | 2.40 ± 0.04 | 2.01 [33] | +20% |
| $CO_2$ (EPM2) | water (TIP4P) | 2.43 ± 0.08 | 2.12 [33] | +14% |
| $CO_2$ (TraPPE) | water (TIP4P) | 2.31 ± 0.06 | 2.12 [33] | +9.1% |
| $N_2O$ | water (TIP4P) | 2.26 ± 0.04 | 2.01 [33] | +12% |
| $CO_2$ (EPM2) | ethanol | 3.76 ± 0.07 | 4.39 [219] | −14% |
| $CO_2$ (TraPPE) | ethanol | 3.73 ± 0.06 | 4.39 [219] | −15% |
| $N_2O$ | ethanol | 4.30 ± 0.04 | 4.57 [219] | −5.8% |
| $CO_2$ (EPM2) | $n$-heptane | 6.00 ± 0.07 | n/a | n/a |
| $CO_2$ (TraPPE) | $n$-heptane | 6.05 ± 0.07 | n/a | n/a |
| $N_2O$ | $n$-heptane | 6.46 ± 0.05 | n/a | n/a |
| $CO_2$ (EPM2) | 30% MEA (SPC/E) | 1.85 ± 0.05 | n/a | n/a |
| $CO_2$ (TraPPE) | 30% MEA (SPC/E) | 1.73 ± 0.07 | n/a | n/a |
| $N_2O$ | 30% MEA (SPC/E) | 1.69 ± 0.05 | 1.56 [33] | +8.6% |
| $CO_2$ (EPM2) | 30% MEA (TIP4P) | 2.00 ± 0.03 | n/a | n/a |
| $CO_2$ (TraPPE) | 30% MEA (TIP4P) | 1.97 ± 0.09 | n/a | n/a |
| $N_2O$ | 30% MEA (TIP4P) | 1.87 ± 0.07 | 1.56 [33] | +20% |



0.07) × $10^{-9}$, (2.43 ± 0.08) × $10^{-9}$ and (3.50 ± 0.08) × $10^{-9}$ m$^2$/s, respectively, compared to the experimental value of 2.12 × $10^{-9}$m$^2$/s reported by Li and Lai [33]. It is obvious that the combination EPM2-TIP5P performs poorly, and therefore we used the SPC/E and TIP4P models for further research. Simulations were then performed in an ensemble containing 1 $CO_2$ solvated in 500 water molecules, 500 ethanol molecules, 500 heptane molecules, and a 30% MEA solution (56 MEA plus 444 $H_2O$) respectively at 303 K. Similar simulations were performed with 1 $N_2O$ molecule in the aforementioned solvents as well. Two models for $H_2O$ (SPC/E and TIP4P) and two models for $CO_2$ (EPM2 and TraPPE) lead to four combinations. Table 5.3 shows the results for all simulations at 303 K and a comparison with the corresponding experimental values from the literature [33, 219]. The simulation results for $CO_2$ and $N_2O$ diffusivities in water and 30% MEA solutions all overpredict the experimental data, while the diffusivities for $CO_2$ in ethanol underestimate the experimental values. The reported difference can be due to the used force fields, which were in fact not optimized for describing transport properties. However, the simulation results are acceptable since the correct magnitude and qualitative trends for the self-diffusivities are predicted. At 303 K, $CO_2$ diffuses faster than $N_2O$ in pure water and 30% MEA solution, whereas in ethanol and heptane $CO_2$ diffuses slower. Our simulation results are in agreement with the experimental data. The diffusion of $CO_2$ is the fastest in heptane and the slowest in a 30% MEA solution and obeys the following order: 30% MEA solution < water < ethanol < heptane. A similar order of diffusivities can be observed for $N_2O$. This confirms that our models and methods are consistent. Considering the error bars, the EPM2 and TraPPE models exhibit no major difference in deviations from experiments. However, the TIP4P model

Table 5.4: The self-diffusivity ratios of $CO_2$ and $N_2O$ in water, ethanol, $n$-heptane, and a 30% MEA solution at a temperature of 303 K. Simulation results are compared to the experimental data. The different models for $CO_2$ and water is indicated.

| Solvent | $[D_{CO_2}/D_{N_2O}]_{\text{sim}}$ | | $[D_{\text{CO}_2}/D_{\text{N}_2\text{O}}]_{\text{exp}}$ | Difference | |
|---|---|---|---|---|---|
| | EPM2 | TraPPE | | EPM2 | TraPPE |
| water (SPC/E) | 1.14 ± 0.07 | 1.15 ± 0.04 | 1.06 [33] | +7.5% | +8.5% |
| water (TIP4P) | 1.07 ± 0.04 | 1.02 ± 0.03 | 1.06 [33] | +0.9% | −3.8% |
| ethanol | 0.87 ± 0.02 | 0.87 ± 0.02 | 0.96 [219] | −9.4% | −9.4% |
| ***n*-heptane** | 0.93 ± 0.01 | 0.94 ± 0.01 | n/a | n/a | n/a |
| 30% MEA (SPC/E) | 1.10 ± 0.04 | 1.02 ± 0.05 | n/a | n/a | n/a |
| 30% MEA (TIP4P) | 1.07 ± 0.05 | 1.05 ± 0.06 | n/a | n/a | n/a |

combined with $CO_2$ seems to perform better, while the SPC/E model combined with MEA and $CO_2$ seems to yield results in better agreement with experiments.

To validate the $CO_2/N_2O$ analogy for the diffusivity as stated in Eq. (5.2), the diffusivity ratios of $CO_2$ to $N_2O$ in the various solvents have been calculated at 303 K and are listed in Table 5.4. The ratios are very close to the experimental value and the differences are almost within 10%. A comparison of the diffusivity in the pure solvents shows that the $CO_2/N_2O$ ratios in water are all above unity while the $CO_2/N_2O$ ratios in ethanol and heptane are all below unity. The ratios are assumed to be sensitive to the solvent dipole moments. In pure solvents with a larger dipole moment (*e.g.* water), $CO_2$ diffuses faster than $N_2O$ while in solvents with a smaller dipole moment (*e.g.* heptane), $CO_2$ diffuses slower. When we compare water to a 30% aqueous MEA solution, it is clear that the $CO_2/N_2O$ diffusion ratios are comparable. All the $CO_2/N_2O$ ratios are approximately 1.1 (within 10% error). This indicates that the $CO_2/N_2O$ analogy for diffusivity as stated in Eq (5.2) is valid for the investigated conditions.

In the following, we elucidate the $CO_2/N_2O$ analogy and its possible extension. The well-known Wilke-Chang's equation [220, 221] is invoked, which provides a general correlation of the diffusion for a binary mixture of solute A in a solvent B. This correlation for the diffusion coefficient in an infinitely diluted solution equals:

$$D_{\text{AB}} = \frac{7.4 \cdot 10^{-8} (\phi M_{\text{B}})^{1/2} T}{\eta_{\text{B}} V_{\text{A}}^{0.6}} \tag{5.7}$$

where $D_{AB}$ ($\text{cm}^2/\text{s}$) is the self-diffusion coefficient of A in B, $\phi$ (dimensionless) refers to association factor of the solvent B, $M_{\text{B}}$ (g/mol) is the molecular weight of solvent B, T (K) is the temperature, $\eta_{\text{B}}$ (cP) is the viscosity of the solvent B, and $V_{\text{A}}$ ($\text{cm}^2/\text{mol}$) represents the molar volume of the solute A at its normal boiling temperature. Wilke and Chang [220] claimed that this equation could achieve 90% accuracy. Applying this equation to predict the diffusivity ratio results in: $D_{\text{CO}_2}/D_{\text{N}_2\text{O}} = [V_{\text{N}_2\text{O}}/V_{\text{CO}_2}]^{0.6}$. This formula indicates that the diffusivity ratio of gases at infinite dilution is directly linked to the molar volume of the solutes. In the case of $D_{\text{CO}_2}/D_{\text{N}_2\text{O}}$ in water, a constant ratio of 1.04 is obtained from experiments ($V_{\text{CO}_2} = 34.0$ $\text{cm}^2/\text{mol}$, $V_{\text{N}_2\text{O}} = 36.4$ $\text{cm}^2/\text{mol}$) [220]. This prediction agrees quite well with our simulation which shows that the $D_{\text{CO}_2}/D_{\text{N}_2\text{O}}$ ratio in water is

approximately 1.1 (±10%). Moreover, Wilke-Chang's equation is more general and indicates that the ratio could be temperature independent. Therefore, it is reasonable to believe that the $CO_2/N_2O$ analogy for the diffusivity (Eq (5.2)), once validated at 303 K (in our case), can be extended to other temperatures as well.

To find out whether or not the reactions of $CO_2$ with amine will have an influence on the diffusion behavior of $CO_2$, the same fully reacted system was set up (as discussed in the previous subsection). 1 $CO_2$ molecule was solvated in a system consisting of 28 carbamate ion ($HOCH_2CH_2NHCOO^-$) particles, 28 amine ion ($HOCH_2CH_2NH_3^+$) particles and 444 water molecules. The SPC/E model was used for water and the EPM2 was used for $CO_2$. The self-diffusivities are computed as $(1.85 \pm 0.05) \times 10^{-9}$ $m^2/s$ for the non-reacted system and $(1.70 \pm 0.06) \times 10^{-9} m^2/s$ for the fully reacted system. The diffusion rate of $CO_2$ is slower in the solution containing the reaction products of the reaction between $CO_2$ and MEA than in the unreacted MEA solution. However, the difference in $CO_2$ diffusivity is less than 10% between the reacted system and the non-reacted system. This result indicates that the $CO_2/N_2O$ analogy for the diffusivity is probably also applicable during the reaction stage of the process.



## 5.4 Conclusions

This chapter aims to validate "the $CO_2/N_2O$ analogy" using molecular simulation. Due to the molecular similarity, $N_2O$ is often substituted for $CO_2$ to establish physical properties (*e.g.* solubility and diffusivity) of $CO_2$, which are otherwise inaccessible due to the presence of a chemical reaction (*e.g.* $CO_2$+amine). This apparent transferability between the physical properties of $CO_2$ and $N_2O$ is known as the $CO_2/N_2O$ analogy. The Continuous Fractional Component Monte Carlo (CFCMC) method in the osmotic ensemble was used to predict the Henry coefficients of $CO_2$ and $N_2O$ in water, ethanol, *n*-heptane, and 30% MEA solution at a temperature of 303 K. Molecular Dynamics simulations were performed to compute the diffusivity of $CO_2$ and $N_2O$ in the aforementioned solvents at 303 K. Different models for $CO_2$ and $H_2O$ were compared when conducting these simulations. For the gas solubility, the TIP5P is found to be a better solvent model than the SPC/E and TIP4P models, while for the gas diffusivity the SPC/E and TIP4P models perform better than the TIP5P model. No significant difference can be observed between the EPM2 and TraPPE models for $CO_2$, but the Henry coefficient of $CO_2$ (TraPPE) in water is in closer agreement with experimental data. The Monte Carlo simulations correctly predict the $CO_2/N_2O$ solubilities in the investigated solvents, which exhibit the following solubility order: heptane > ethanol > 30% MEA > water. Molecular Dynamics simulations also correctly predict the observed $CO_2/N_2O$ diffusivities in the solvents, which obeys the following order: heptane > ethanol > water > 30% MEA. The simulation results indicate that the $CO_2/N_2O$ analogy is valid for water and 30% MEA solution at 303 K. The ratio of the Henry coefficients $CO_2/N_2O$ is approximately 0.77 (±10%) and the ratio of the self-diffusivities $CO_2/N_2O$ is around 1.1 (±10%). Additional simulations were performed to investigate the effect of a chemical reaction between $CO_2$ and MEA on the physical solubility and self-diffusivity of $CO_2$. The simulation results indicate that both the physical solubility

and the self-diffusivity of $CO_2$ are lower in the system containing reaction products of $CO_2$ and MEA, which is a result of the reaction between $CO_2$ and MEA.

# 6

# Solubility of Pre-combustion Gases in Ionic Liquids

This chapter is based on the following publication: M. Ramdin, S.P. Balaji, J.M. Vicent-Luna, J.J. Gutierrez-Sevillano, S. Calero, T.W. de Loos, T.J.H. Vlugt, *Solubility of the Precombustion Gases $CO_2$, $CH_4$, CO, $H_2$, $N_2$, and $H_2S$ in the Ionic Liquid [bmim][$Tf_2N$] from Monte Carlo Simulations*, J. Phys. Chem. C **2014**, 118, 23599-23604 [49]

## 6.1 Introduction

Carbon dioxide ($CO_2$) capture using chemical solvents like monoethanolamine (MEA) is a mature technology used for decades in natural gas sweetening and the hydrogen purification process [159]. Application of the amine process for $CO_2$ capture from flue gas at post-combustion (*i.e.* low pressure) conditions is mainly hindered by the high energy consumption and the immense scale of the problem [15, 222]. To give an impression of the scale of flue gas production relative to the scale of natural gas processing, consider the following example. The global $CO_2$ emission and the global natural gas production in 2012 was 34.5 billion tonnes (∼17580 billion cubic meters (bcm)) and 3364 bcm, respectively [223, 224]. Assuming that the flue gas and the raw natural gas contained 10 % $CO_2$, one can calculate the actual volume of flue gas or natural gas that had to be processed at the power plant (175800 bcm) or at the well (3738 bcm), respectively. This simple example shows that the global scale of flue gas production is ∼50 times larger than the global scale of natural gas production. Moreover, the estimated energy penalty of a coal-fired power plant using MEA for $CO_2$ capture is in the range of 25 to 45 % [25]. A huge amount of steam/energy is required in the desorber for solvent regeneration and concurrent liberation of the chemically complexed $CO_2$ [8]. Post-combustion $CO_2$ capture inevitably requires a chemical solvent, because the low partial pressure of $CO_2$ (0.1 - 0.15 bar) in the flue gas eliminates the use of physical solvents [15, 25]. In contrast to post-combustion capture, pre-combustion $CO_2$ capture in integrated gasification combined cycle (IGCC) plants allows the use of physical solvents, since the partial pressure of $CO_2$ in the syngas is 100 - 1000 times higher than that of post-combustion conditions [225]. The pre-combustion process involves a reaction of the fuel with air/oxygen and steam to produce syngas, which is a mixture of carbon monoxide (CO) and hydrogen ($H_2$). In the case of natural gas as fuel, the syngas is produced via the steam-reforming reaction [226]:



$$CH_4 + H_2O \rightleftharpoons CO + 3H_2 \tag{R1}$$

In a next step, the CO is converted according to the water-gas-shift (WGS) reaction to $CO_2$ and more $H_2$:

$$CO + H_2O \rightleftharpoons CO_2 + H_2 \tag{R2}$$

After separating the $CO_2$ from $H_2$, the hydrogen-rich fuel can be used in many applications like gas turbines for electricity production, engines, fuel cells, and chemical synthesis such as ammonia, methanol and Fischer-Tropsch fuels [227]. The advantage of pre-combustion $CO_2$ capture is the relatively high partial pressure of $CO_2$ after the WGS reaction allowing for less expensive separation methods including physical absorption/adsorption and membranes [17, 228]. Several existing solvents (*e.g.* amines, Selexol and Rectisol) and new materials (*e.g.* zeolites and metal-organic frameworks (MOFs)) have been considered for pre-combustion $CO_2$ capture [7, 229–231]. The reader is referred to the recent work of Liu *et al.* [227] for an excellent state-of-the-art review of technologies used for hydrogen/syngas production and purification.

The focus of this chapter is to investigate the separation of $CO_2$ from syngas, either before or after the water gas shift reaction, using the ionic liquid (IL) 1-butyl-3-methylimidazolium bis(trifluoromethylsulfonyl)imide [bmim][$Tf_2N$]. The equilibrium reactions R1 and R2 yield a mixture of reactants and products, which will require a separation step downstream of the process. The relevant separation selectivities are $CO_2/CH_4$, $CO_2/CO$, $CO_2/H_2$, $CO_2/N_2$ if air instead of pure oxygen is used, and $CO_2/H_2S$ if the syngas is not desulfurized prior to $CO_2$ removal. The selectivity of one gas over the other can be calculated from solubility data of the corresponding gases in the IL. Unfortunately, solubility data of sparingly soluble gases (*e.g.* $H_2$, $N_2$ and $CH_4$) or toxic gases (*e.g.* CO and $H_2S$) are scarcely reported in the literature. An alternative tool for these difficult to conduct experiments is provided by means of molecular simulations. Here, Monte Carlo simulations using a classical force field have been used to predict the solubility of the gases $CO_2$, $CH_4$, CO, $H_2$, $N_2$ and $H_2S$ in the IL [bmim][$Tf_2N$] and whenever possible a comparison with experimental data is provided.

This chapter is organized as follows. In section 6.2, the simulation details (*i.e.* force fields and simulation methodology) are outlined. Subsequently, the results on gas solubilities and selectivities are presented and discussed thoroughly in section 6.3. Our findings are summarized in section 6.4

## 6.2 Simulation Details



The recently developed Continuous Fractional Component Monte Carlo (CFCMC) method in the osmotic ensemble has been used to compute absorption isotherms of the pre-combustion gases $CH_4$, $CO_2$, CO, $H_2$, $N_2$, and $H_2S$ in the IL [bmim][$Tf_2N$] [70, 77, 78, 194]. This method has been discussed in detail in chapter 3.

A classical force field including bond-stretching, bond-bending, torsion, Lennard-Jones (LJ) and electrostatic interactions was used for the IL molecules in our simulations. The force field parameters for the IL [bmim][$Tf_2N$] have been taken from Liu and Maginn [198]. The molecular models used for the gases contain one or more LJ interaction sites with or without partial charges and/or dipoles. All the gases have been treated as rigid in the simulations. The standard TraPPE model was used for the gases $CH_4$, $CO_2$ and $N_2$ [181]. The CO model, which includes a dipole moment, has been adopted from Martín-Calvo *et al.* [232]. For $H_2$, the two-center LJ model of Cracknell has been applied [233]. For $H_2S$, three different models have been used; the three-site (3S) model of Kamath *et al.* [234], the four-site (4S) model of Kristóf and Lizi, [235] and the five-site (5S) model of Gutiérrez-Sevillano *et al.* [236]. The Lorentz-Berthelot mixing rules were adopted for the LJ interactions between unlike atoms [51]. The Ewald method with a relative precision of $10^{-5}$ was applied to account for the long range electrostatic interactions. The LJ interactions were truncated and shifted at 12 Å and no tail corrections were applied. All simulations were performed in the osmotic ensemble, which implies that the fugacity of the gas ($f$), the number of (nonvolatile) IL molecules ($N$), the total hydrostatic pressure ($P$) and the temperature ($T$) were all fixed. The volume of the system and the number of gas molecules in the liquid-phase will change as a consequence of the imposed pressure and fugacity in order to satisfy the equilibrium condition $f_i^V = f_i^L$. Note

that the Gibbs phase rule is not violated by disallowing IL molecules in the gas phase, because the number of equilibrium conditions and the number of intensive variables are both reduced by one [237]. Furthermore, the assumption that only solutes without IL molecules are present in the gas phase is reasonable, since ILs have a negligible vapor pressure [238]. The fugacity of the gases was obtained from the Peng-Robinson (PR) equation of state (EoS) [203]. The $\lambda$ moves were biased using the Wang-Landau sampling scheme, which enforces the system to visit all the possible $\lambda$ states and to achieve a flat histogram for $\lambda$ [144]. The Configurational-Bias Monte Carlo (CBMC) scheme was used to sample the internal degrees of freedom of the IL molecules [53, 115, 119, 124].

The CFCMC simulations were executed at a temperature of 333.15 K using an ensemble of 50 IL molecules. All the MC simulations were performed using the molecular simulation tool RASPA [117]. In order to reduce the simulation time, however, the IL structure was first equilibrated using Molecular Dynamics (MD) simulations in GROMACS [239]. After an energy minimization step, an ensemble of 50 IL molecules were simulated for 2 ns in the NPT ensemble. In a subsequent step, the atomic positions and velocities of the equilibrated ensemble were transferred to RASPA to perform the actual CFCMC simulations. The CFCMC simulations were started with an equilibration run of 50000 MC cycles, where the number of MC steps in a cycle equals the total number of molecules in the simulation box. In this equilibration run, the weights of the various MC moves are adjusted to obtain 50 % acceptance rates. The production runs consisted of 0.5 to 1 million cycles, where the exact number was dictated by the convergence characteristics of the system. The reported data were obtained from block averages, and the standard deviation was used to calculate the uncertainty. The CPU time required to compute the solubilities ranged from 3-4 weeks in total for the equilibration and production runs using state-of-the-art computation facilities.



## 6.3 Results and Discussion

### 6.3.1. Solubility

The solubility of $CO_2$, $CH_4$, CO, $H_2$, $N_2$ and $H_2S$ in the IL [bmim][$Tf_2N$] was obtained from MC simulations in the osmotic ensemble at a temperature of 333.15 K and pressures up to 15 MPa. In Fig. 6.1 and Tables 6.1, 6.2, 6.3, 6.4, the solubility of $CO_2$, $CH_4$, CO and $H_2$ obtained from the MC simulations is, respectively, compared with the experimental data of Raeissi *et al.* [240–243]

The experimental uncertainty is typically 0.003 in the mole fractions, whereas the uncertainty in the simulations is typically lower than 0.002 in the mole fractions. The uncertainty of the simulations will only be reported if this is higher than the experimental uncertainty. The MC simulations slightly underpredict the solubility of CO and $H_2$, but the agreement is excellent for the gases $CO_2$ and $CH_4$ even at higher pressures. The simulation results for $N_2$ solubility in [bmim][$Tf_2N$] are reported in Table 6.5 and depicted in Fig. 6.1.

For this system no experimental data has been reported, but the predicted solubilities are in between that of $H_2$ and CO, which is consistent with the trend observed

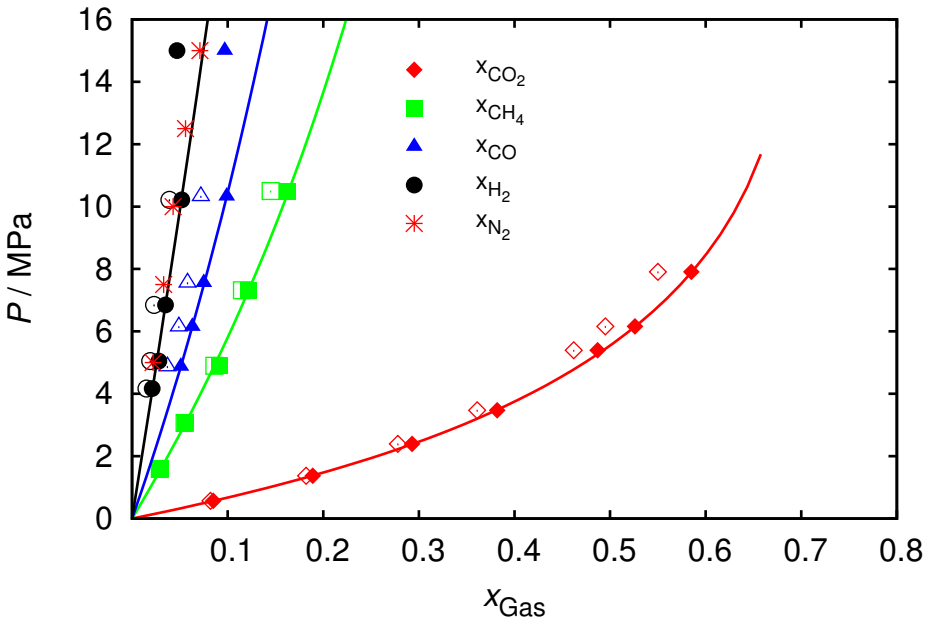


Figure 6.1: Solubility of $CO_2$, $CH_4$, CO, $H_2$ and $N_2$ in [bmim][$Tf_2N$] from MC simulations (open symbols) and experiments (filled symbols) at a temperature of 333.15 K. $CO_2$ experiments (filled diamonds) and MC data (open diamonds); $CH_4$ experiments (filled squares) and MC data (open squares); CO experiments (filled triangles) and MC data (open triangles); $H_2$ experiments (filled circles) and MC data (open circles), and MC data of $N_2$ (stars). Lines are Peng-Robinson equation of state modeling results [47, 203].



in other ILs [8, 244–246]. The $H_2S$ solubilities obtained from MC simulations using the three different $H_2S$ models are compared with the experimental data of Jalili *et al.* [247] in Fig. 6.2 and Table 6.6.

The MC simulations highly overpredict the $H_2S$ solubility, regardless of the used $H_2S$ model, compared to the experimental data of Jalili *et al.* The 3S model of Kamath *et al.* and the 4S model of Kristóf and Lizi are slightly in better agreement with the experimental data than the 5S model of Gutiérrez-Sevillano *et al.* Differences can be attributed to the used force field, but the simulation results are acceptable considering that none of the interaction parameters used in this study were fitted to the experimental solubility data of [bmim][$Tf_2N$]. Moreover, the MC simulations correctly predict the experimental solubility trend, which obeys the following order: $H_2S > CO_2 > CH_4 > CO > N_2 > H_2$. These results show that molecular simulation is a promising tool for predicting gas solubilities in complex systems like ionic liquids.

Table 6.1: Solubility of $CO_2$ (1) in the IL [bmim][$Tf_2N$] (2) at a temperature of 333.15 K and different pressures.

| $p$/MPa | $x_1^{\text{exp.}}$ | $x_1^{\text{sim.}}$ | difference/% |
|---|---|---|---|
| 0.569 | 0.085 | 0.082 | 3.3 |
| 1.373 | 0.189 | 0.182 | 3.7 |
| 2.392 | 0.293 | 0.278 | 4.8 |
| 3.469 | 0.382 | 0.361 | 5.3 |
| 5.396 | 0.487 | 0.462 | 5.0 |
| 6.159 | 0.526 | 0.495 | 5.8 |
| 7.908 | 0.585 | 0.550 | 6.1 |

Table 6.2: Solubility of $CH_4$ (1) in the IL [bmim][$Tf_2N$] (2) at a temperature of 333.15 K and different pressures.

| $p$/MPa | $x_1^{\text{exp.}}$ | $x_1^{\text{sim.}}$ | difference/% |
|---|---|---|---|
| 1.591 | 0.030 | 0.029 | 3.8 |
| 3.063 | 0.056 | 0.055 | 1.5 |
| 4.900 | 0.091 | 0.086 | 5.6 |
| 7.320 | 0.122 | 0.115 | 5.9 |
| 10.497 | 0.163 | 0.145 | 10.7 |



Table 6.3: Solubility of CO (1) in the IL [bmim][$Tf_2N$] (2) at a temperature of 333.15 K and different pressures.

| $p$/MPa | $x_1^{\text{exp.}}$ | $x_1^{\text{sim.}}$ | difference/% |
|---|---|---|---|
| 4.871 | 0.051 | 0.037 | 27.1 |
| 6.153 | 0.063 | 0.049 | 21.8 |
| 7.558 | 0.075 | 0.058 | 22.4 |
| 10.326 | 0.099 | 0.072 | 27.1 |
| 15.000 | - | 0.097 | - |

Table 6.4: Solubility of $H_2$ (1) in the IL [bmim][$Tf_2N$] (2) at a temperature of 333.15 K and different pressures.

| $p$/MPa | $x_1^{\text{exp.}}$ | $x_1^{\text{sim.}}$ | difference/% |
|---|---|---|---|
| 4.167 | 0.0212 | 0.015 | 30.3 |
| 5.047 | 0.0283 | 0.019 | 31.3 |
| 6.849 | 0.035 | 0.023 | 33.0 |
| 10.216 | 0.0516 | 0.039 | 23.7 |
| 15.000 | - | 0.047 | - |

Table 6.5: Solubility of $N_2$ (1) in the IL [bmim][$Tf_2N$] (2) at a temperature of 333.15 K and different pressures.

| $p$/MPa | $x_1^{\text{sim.}}$ |
|---|---|
| 5.00 | 0.022 |
| 7.50 | 0.033 |
| 10.00 | 0.043 |
| 12.50 | 0.056 |
| 15.00 | 0.071 |

Table 6.6: Solubility of $H_2S$ (1) in the IL [bmim][$Tf_2N$] (2) at a temperature of 333.15 K and different pressures.

| $H_2S$ model | $p$/MPa | $x_1^{\text{exp.}}$ | $x_1^{\text{sim.}}$ | difference/% |
|---|---|---|---|---|
| $H_2S^a$ | 0.133 | 0.055 | 0.115 | 109.2 |
| | 0.345 | 0.148 | 0.230 | 55.1 |
| | 0.494 | 0.206 | 0.306 | 48.3 |
| | 0.682 | 0.272 | 0.398 | 46.2 |
| | 0.835 | 0.322 | 0.451 | 39.9 |
| $H_2S^b$ | 0.133 | 0.055 | 0.114 | 107.7 |
| | 0.345 | 0.148 | 0.244 | 64.6 |
| | 0.494 | 0.206 | 0.316 | 53.4 |
| | 0.682 | 0.272 | 0.405 | 48.8 |
| | 0.835 | 0.322 | 0.479 | 48.8 |
| $H_2S^c$ | 0.133 | 0.055 | 0.112 | 103.5 |
| | 0.345 | 0.148 | 0.251 | 69.8 |
| | 0.494 | 0.206 | 0.342 | 66.1 |
| | 0.682 | 0.272 | 0.412 | 51.4 |
| | 0.835 | 0.322 | 0.500 | 55.3 |

[a] Three-site model of Kamath *et al.* [234]
[b] Four-site model of Kristóf and Lizi [235].
[c] Five-site model of Gutiérrez-Sevillano *et al.* [236].

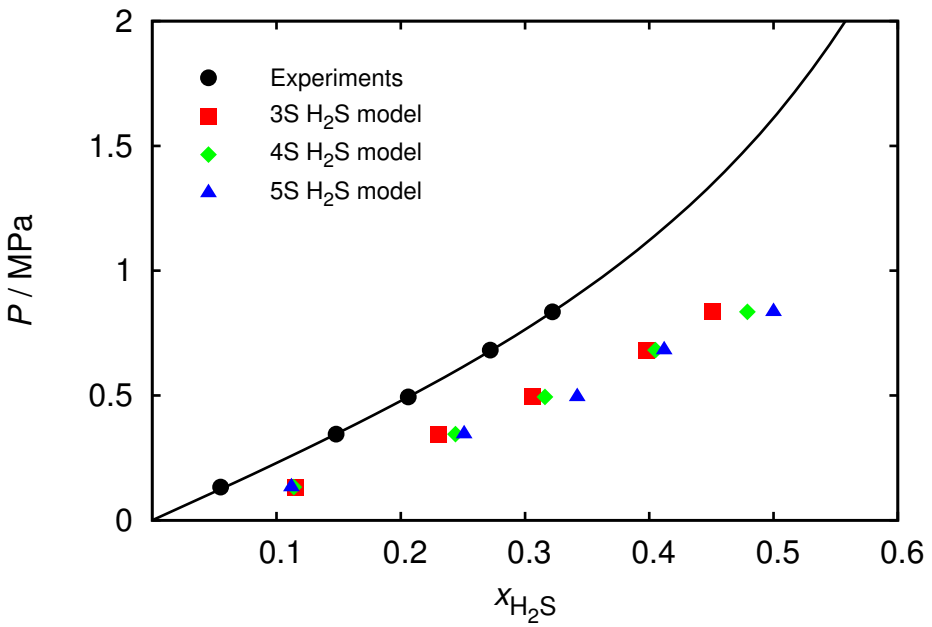


Figure 6.2: Solubility of $H_2S$ in [bmim][$Tf_2N$] at a temperature of 333.15 K. Experiments (filled circles) and MC data: 3S $H_2S$ model (filled squares), 4S $H_2S$ model (filled diamonds) and 5S $H_2S$ model (filled triangles). The solid line represents the results from the modeling using the Peng-Robinson equation of state [47, 203].

Table 6.7: Henry constants of $CO_2$, $CH_4$, CO, $H_2$, $N_2$, and $H_2S$ in Selexol and the IL [bmim][$Tf_2N$] at a temperature of 333.15 K.

| Solute | $H^{\text{exp.}}_{\text{Selexol}}$/MPa | $H^{\text{exp.}}_{\text{IL}}$/MPa | $H^{\text{sim.}}_{\text{IL}}$/MPa | difference/% |
|---|---|---|---|---|
| $CO_2$ | 6.81[a] | 6.56 | 7.10 | 8.2 |
| $CH_4$ | 40.13[a] | 52.4 | 53.7 | 2.5 |
| CO | - | 95 | 125.9 | 33.0 |
| $H_2$ | 193[b] | 199 | 271.7 | 36.3 |
| $N_2$ | 151[b] | - | 225.7 | - |
| $H_2S$ (3S) | 1.01[c] | 2.17 | 1.15 | 47.0 |
| $H_2S$ (4S) | 1.01 | 2.17 | 1.16 | 46.5 |
| $H_2S$ (5S) | 1.01 | 2.17 | 1.17 | 46.1 |

[a] Taken from Rayer *et al.* [248, 249]
[b] Calculated from Gainar *et al.* [250]
[c] Taken from Xu *et al.* [251]

### 6.3.2. Selectivity

The separation performance of a real process is not governed by the solubility, but the key parameter is the selectivity of a target component with respect to the other components in the mixture [47, 48]. This means that a good solvent for $CO_2$ capture at pre-combustion conditions should have a high $CO_2$ solubility, but at the same time a low capacity for the other gases (*e.g.* $CH_4$). The ideal selectivity can be calculated in many different ways from the pure gas solubility data [48]. Here, the ratio of the Henry constants is used to quantify the ideal selectivity ($S^{\text{I}}_{i/j}$), where $i$ is the target component and $j$ the undesired component [48]:

$$S^{\text{I}}_{i/j} = \left(\frac{H_j}{H_i}\right)_T \tag{6.1}$$

The Henry constants of the solutes $i$ in the solvent $j$, [bmim][$Tf_2N$], are calculated from Eq. (5.5). The Henry constants derived from the MC data are compared with the experimental data in Table 6.7. The agreement between the MC data and the experiments is excellent for the gases $CO_2$ and $CH_4$. For the other gases the absolute deviation between the predicted and experimental Henry constants can be as high as 40 %. However, the sparingly soluble gases (CO, $H_2$ and $N_2$) are generally difficult to measure and consequently the uncertainty in the experimental Henry constant is often large (*e.g.* in some cases up to 50 %) [8]. The relevant selectivities for the pre-combustion process were calculated using Eq. (6.1) and compared with experimental data in Table 6.8.

The absolute deviation between the predicted and experimental selectivities are of the same order as for the Henry constants. It is important to note that the high $CO_2/CH_4$, $CO_2/CO$, $CO_2/N_2$ and $CO_2/H_2$ selectivities indicate a great potential of [bmim][$Tf_2N$] for $CO_2$ removal from the pre-combustion process. However, the syngas should be desulfurized before the $CO_2$ removal step, because $CO_2$ cannot be removed selectively in the presence of $H_2S$. A comparison of the Henry constants and the selectivities of the gases in [bmim][$Tf_2N$] and the widely used solvent Selexol is

Table 6.8: Selectivity of $CO_2$, $CH_4$, CO, $H_2$, $N_2$, and $H_2S$ in Selexol and the IL [bmim][$Tf_2N$] at a temperature of 333.15 K.

| Separation | $S^{\text{exp.}}_{\text{Selexol}}$ | $S^{\text{exp.}}_{\text{IL}}$ | $S^{\text{sim.}}_{\text{IL}}$ | difference/% |
|---|---|---|---|---|
| $CO_2/CH_4$ | 5.9[a] | 8.0 | 7.6 | 5.3 |
| $CO_2/CO$ | - | 14.4 | 17.7 | 23.0 |
| $CO_2/H_2$ | 25[b] | 30.4 | 38.3 | 26.0 |
| $CO_2/N_2$ | 20[b] | - | 31.8 | - |
| $CO_2/H_2S$ | 0.15[c] | 0.33 | 0.16 | 51.0 |
| $CO_2/H_2S$ | 0.15 | 0.33 | 0.16 | 50.6 |
| $CO_2/H_2S$ | 0.15 | 0.33 | 0.16 | 50.2 |

[a] Calculated from Rayer *et al.* [248, 249]
[b] Calculated from Gainar *et al.* [250]
[c] Calculated from Xu *et al.* [251]

provided in Tables 6.7 and 6.8, respectively. Clearly, the Henry constants and the selectivities in both solvents are very similar, hence considering the price/performance ratio the Selexol solvent outperforms the costly IL [bmim][$Tf_2N$].

## 6.4 Conclusions



Monte Carlo simulations were used to predict the solubility of the single gases $CO_2$, $CH_4$, CO, $H_2$, $N_2$ and $H_2S$ in the ionic liquid (IL) 1-butyl-3-methylimidazolium bis(trifluoromethylsulfonyl)imide [bmim][$Tf_2N$]. Simulations in the osmotic ensemble were performed to compute absorption isotherms at a temperature of 333.15 K using the versatile Continuous Fractional Component Monte Carlo (CFCMC) method. The predicted gas solubilities and Henry constants are in good agreement with the experimental data. The MC simulations correctly predict the observed solubility trend, which obeys the following order: $H_2S > CO_2 > CH_4 > CO > N_2 > H_2$. The $CO_2/CH_4$, $CO_2/CO$, $CO_2/N_2$, $CO_2/H_2$ and $CO_2/H_2S$ selectivities relevant for the pre-combustion $CO_2$ capture process were calculated from the ratio of pure gas Henry constants. The results indicate that [bmim][$Tf_2N$] can effectively capture $CO_2$ at pre-combustion conditions, but the syngas should be desulfurized prior to $CO_2$ removal, because $H_2S$ is three times more soluble than $CO_2$. Moreover, we have shown that molecular simulations can be used to predict gas solubilities in complex systems like ionic liquids.

# Bibliography


[1] Intergovernmental Panel on Climate Change (IPCC), Climate Change 2013: The Physical Science Basis, Contribution of Working Group I to the Fifth Assessment Report of the Intergovernmental Panel on Climate Change, Cambridge, UK (2013), http://www.ipcc.ch/publications_and_data/publications_and_data_reports.shtml (accessed April 15, 2015).

[2] IEA, Key World Energy Stastics (2013), http://www.iea.org/publications/freepublications/publication/key-world-energy-statistics-2013.html (accessed April 15, 2015).

[3] IEA, $CO_2$ Emissions From Fuel Combustion Highlights (2014), http://www.iea.org/publications/freepublications/publication/co2-emissions-from-fuel-combustion-highlights-2014.html (accessed April 15, 2015).

[4] GCCSI, $CO_2$ Capture Technologies (2012), http://www.globalccsinstitute.com/publications/co2-capture-technologies (accessed April 15, 2015).

[5] Carbon Capture and Storage Research, http://energy.gov/fe/science-innovation/carbon-capture-and-storage-research (accessed April 15, 2015).

[6] McKinsey & Company, Carbon Capture and Storage: Assessing the Economics (2008), http://www.mckinsey.com/clientservice/ccsi/pdf/CCS-Assessing-the-Economics.pdf (accessed April 15, 2015).

[7] B. Smit, J. A. Reimer, C. M. Oldenburg, and I. C. Bourg, *Introduction to Carbon Capture and Sequestration* (Imperial College Press, London, UK, 2014).

[8] M. Ramdin, T. W. de Loos, and T. J. H. Vlugt, State-of-the-Art of $CO_2$ Capture with Ionic Liquids, Ind. Eng. Chem. Res. **51**, 8149 (2012).

[9] H. P. Mangalapally and H. Hasse, Pilot Plant Experiments for Post-combustion Carbon Dioxide Capture by Reactive Absorption with Novel Solvents, Energy Procedia **4**, 1 (2011).

[10] R. R. Bottoms, Process for Separating Acidic Gases (1930), http://www.google.com/patents/US1783901 (accessed April 15, 2015).

[11] M. R. M. Abu-Zahra, L. H. J. Schneiders, J. P. M. Niederer, P. H. M. Feron, and G. F. Versteeg, $CO_2$ Capture from Power Plants Part I. A Parametric Study of the Technical Performance based on Monoethanolamine, Int. J. Green. Gas Cont. **1**, 37 (2007).

[12] M. R. M. Abu-Zahra, J. P. M. Niederer, P. H. M. Feron, and G. F. Versteeg, $CO_2$ Capture from Power Plants Part II. A Parametric Study of the Economical Performance based on Monoethanolamine, Int. J. Green. Gas Cont. **1**, 135 (2007).

[13] B. J. P. Buhre, L. K. Elliott, C. D. Sheng, R. P. Gupta, and T. F. Wall, Oxy-Fuel Combustion Technology for Coal-Fired Power Generation, Prog. Energy Combust. Sci. **31**, 283 (2005).

[14] T. F. Wall, Y. Liu, C. Spero, L. Elliott, S. Khare, R. Rathnam, F. Zeenathal, B. Moghtaderi, B. Buhre, C. Sheng, R. Gupta, T. Yamada, K. Makino, and J. Yua, An Overview on Oxyfuel Coal Combustion - State of the Art Research and Technology Development, Chem. Eng. Res. Des. **87**, 1003 (2009).

[15] J. D. Figueroa, T. Fout, S. Plasynski, H. McIlvried, and R. D. Srivastava, Advances in $CO_2$ capture technology-The U.S. Department of Energy's Carbon Sequestration Program, Int. J. Greenhouse Gas Control **2**, 9 (2008).

[16] M. Kanniche, R. Gros-Bonnivard, P. Jaud, J. Valle-Marcos, J.-M. Amann, and C. Bouallou, Pre-combustion, Post-combustion and Oxy-Combustion in Thermal Power Plant for $CO_2$ Capture, Appl. Therm. Eng. **30**, 53–62 (2010).

[17] C. A. Scholes, K. H. Smith, S. E. Kentish, and G. W. Stevens, $CO_2$ Capture from Pre-combustion Processes-Strategies for Membrane Gas Separation, Int. J. Greenhouse Gas Control **4**, 739 (2010).

[18] P. V. Danckwerts, The Reaction of $CO_2$ with Ethanolamines, Chem. Eng. Sci. **34**, 443 (1979).

[19] A. L. Kohl and R. Nielsen, *Gas Purification* (Gulf Professional Publishing, Houston, 5th Edition, 1997).

[20] Intergovernmental Panel on Climate Change (IPCC), Special Report on Carbon Dioxide Capture and Storage, Cambridge, UK (2005), `http://www.ipcc.ch/publications_and_data/_reports_carbon_dioxide.htm` (accessed April 15, 2015).

[21] E. Favre, Membrane Processes and Post-combustion Carbon Dioxide Capture: Challenges and Prospects, Chem. Eng. J. **171**, 782 (2011).

[22] C. H. Yu, C. H. Huang, and C. S. Tan, A Review of $CO_2$ Capture by Absorption and Adsorption, Aerosol and Air Quality Research **12**, 745 (2012).

[23] R. Banerjee, A. Phan, B. Wang, C. Knobler, H. Furukawa, M. O'Keeffe, and O. M. Yaghi, High-Throughput Synthesis of Zeolitic Imidazolate Frameworks and Application to $CO_2$ Capture, Science **319**, 939–43 (2008).

[24] Z. Zhang, Y. Zhao, Q. Gong, Z. Li, and J. Li, MOFs for $CO_2$ Capture and Separation from Flue Gas Mixtures: The Effect of Multifunctional Sites on Their Adsorption Capacity and Selectivity, Chem. Commun. **49**, 653–661 (2013).

[25] D. M. D'Alessandro, B. Smit, and J. R. Long, Carbon Dioxide Capture: Prospects for New Materials, Angew. Chem. Int. Ed. **49**, 6058 (2010).

[26] M. Ishida and H. Jin, A New Advanced Power-Generation System using Chemical-Looping Combustion, Energy **19**, 415–422 (1994).

[27] R. N. Maddox, G. J. Mains, and M. Rahman, Reactions of Carbon Dioxide and Hydrogen Sulfide with Some Alkanolamines, Ind. Eng. Chem. Res. **26**, 27 (1987).

[28] E. T. Hessen, T. Haug-Warberg, and H. F. Svendsen, The Refined e-NRTL Model Applied to $CO_2$–$H_2O$–Alkanolamine Systems, Chem. Eng. Sci. **65**, 3638 (2010).

[29] R. Hiwale, S. Hwang, and R. Smith, Model Building Methodology for Multiphase Reaction Systems-Modeling of $CO_2$ Absorption in Monoethanolamine for Laminar Jet Absorbers and Packing Beds, Ind. Eng. Chem. Res. **51**, 4328 (2012).

[30] B. P. Mandal, M. Kundu, and S. S. Bandyopadhyay, Physical Solubility and Diffusivity of $N_2O$ and $CO_2$ into Aqueous Solutions of (2-Amino-2-methyl-1-propanol + Monoethanolamine) and (N-Methyldiethanolamine + Monoethanolamine), J. Chem. Eng. Data **50**, 352 (2005).

[31] F. Jou, A. E. Mather, and F. D. Otto, The Solubility of $CO_2$ in a 30 Mass percent Monoethanolamine Solution, Can. J. Chem. Eng. **73**, 140 (1995).

[32] J. K. A. Clarke, Kinetics of Absorption of Cardon Dioxide in Monoethanolamine Solutions at Short Contact Times, Ind. Eng. Chem. Fund. **3**, 239 (1964).

[33] M. Li and M. Lai, Solubility and Diffusivity of $N_2O$ and $CO_2$ in (Monoethanolamine+ N-Methyldiethanolamine+ Water) and in (Monoethanolamine+ 2-Amino-2-methyl-1-propanol+ Water), J. Chem. Eng. Data **40**, 486 (1995).

[34] W. T. Batt, R. N. Maddox, G. J. Mains, M. Rahman, and R. N. Vaz, Chemical and Engineering Fundamentals of Ethanolamine Sweetening, 1980 Gas Conditioning Conference (1980).

[35] G. Sartori and G. W. Savage, Sterically Hindered Amines for $CO_2$ Removal from Gases, Ind. Eng. Chem. Res. **22**, 239 (1983).

[36] B. R. Strazisar, R. R. Anderson, and C. M. White, Degradation Pathways for Monoethanolamine in a $CO_2$ Capture Facility, Energy Fuels **17**, 1034 (2003).

[37] L. D. Polderman, C. P. Dillon, and A. B. Steele, Degradation of Monoethanolamine in Natural Gas Treating Service, Oil Gas J. **53**, 180 (1955).

[38] M. Li and W. Lee, Solubility and Diffusivity of $N_2O$ and $CO_2$ in (Diethanolamine+ N-Methyldiethanolamine+ Water) and in (Diethanolamine+ 2-Amino-2-methyl-1-propanol+ Water), J. Chem. Eng. Data **41**, 551 (1996).

[39] N. M. Haimour and O. C. Sandall, Absorption of Carbon Dioxide into Aqueous Methyldiethanolamine, Chem. Eng. Sci. **39**, 1791 (1984).

[40] H. Kierzkowska-Pawlak and R. Zarzycki, Solubility of Carbon Dioxide and Nitrous Oxide in Water+ Methyldiethanolamine and Ethanol+ Methyldiethanolamine Solutions, J. Chem. Eng. Data **47**, 1506 (2002).

[41] A. Samanta, S. Roy, and S. S. Bandyopadhyay, Physical Solubility and Diffusivity of $N_2O$ and $CO_2$ in Aqueous Solutions of Piperazine and (N-Methyldiethanolamine+ Piperazine), J. Chem. Eng. Data **52**, 1381 (2007).

[42] A. K. Saha, S. S. Bandyopadhyay, and A. K. Biswas, Solubility and Diffusivity of $N_2O$ and $CO_2$ in Aqueous Solutions of 2-Amino-2-methyl-1-propanol, J. Chem. Eng. Data **38**, 78 (1993).

[43] S. Xu, F. D. Otto, and A. E. Mather, Physical Properties of Aqueous AMP Solutions, J. Chem. Eng. Data **36**, 71 (1991).

[44] M. Afkhamipour and M. Mofarahi, Comparison of Rate-based and Equilibrium-stage Models of a Packed Column for Post-combustion $CO_2$ Capture using 2-Amino-2-methyl-1-propanol (AMP) Solution, Int. J. Green. Gas. Cont. **15**, 186 (2013).

[45] G. T. Rochelle, E. Chen, S. Freeman, D. V. Wagener, Q. Xu, and A. Voice, Aqueous Piperazine as the New Standard for $CO_2$ Capture Technology, Chem. Eng. J. **171**, 725–733 (2011).

[46] H. Y. Dang and G. T. Rochelle, $CO_2$ Absorption Rate and Solubility in Monoethanolamine/Piperazine/Water, Sep. Sci. Technol. **38**, 337 (2003).

[47] M. Ramdin, A. Amplianitis, T. W. de Loos, and T. J. H. Vlugt, Solubility of $CO_2/CH_4$ Gas Mixtures in Ionic Liquids, Fluid Phase Equilib. **375**, 134 (2014).

[48] M. Ramdin, A. Amplianitis, S. Bazhenov, A. Volkov, V. Volkov, T. J. H. Vlugt, and T. W. de Loos, Solubility of $CO_2$ and $CH_4$ in Ionic Liquids: Ideal $CO_2/CH_4$ Selectivity, Ind. Eng. Chem. Res. **53**, 15427 (2014).

[49] M. Ramdin, S. P. Balaji, J. M. Vicent-Luna, J. J. Gutierrez-Sevillano, S. Calero, T. W. de Loos, and T. J. H. Vlugt, Solubility of the Precombustion Gases $CO_2$, $CH_4$, CO, $H_2$, $N_2$, and $H_2S$ in the Ionic Liquid [bmim][$Tf_2N$] from Monte Carlo Simulations, J. Phys. Chem. C **118**, 23599 (2014).

[50] L.-C. Lin, A. H. Berger, R. L. Martin, J. Kim, J. A. Swisher, K. Jariwala, C. H. Rycroft, A. S. B. andM. W. Deem, M. Haranczyk, and B. Smit, In Silico Screening of Carbon-Capture Materials, Nat. Mater. **11**, 633–641 (2012).

[51] M. P. Allen and D. J. Tildesley, *Computer Simulation of Liquids* (Oxford University Press, USA, 1989).

[52] D. A. McQuarrie, *Statistical Mechanics* (University Science Books, Sausalito, CA, USA; 1st edition, 2000).

[53] D. Frenkel and B. Smit, *Understanding Molecular Simulation, From Algorithms to Applications*, 2nd ed. (Academic Press, London, U.K., 2002).

[54] M. E. Tuckermann, *Statistical Mechanics: Theory and Molecular Simulation* (Oxford University Press; 1st edition, 2010).

[55] E. Kalnay, *Atmospheric Modeling, Data Assimilation and Predictability* (Cambridge University Press, 2003).

[56] T. J. H. Vlugt, J. P. J. M. van der Eerden, M. Dijkstra, B. Smit, and D. Frenkel, *Introduction to Molecular Simulation and Statistical Thermodynamics* (2009) available from: `http://homepage.tudelft.nl/v9k6y/imsst/`.

[57] R. C. Rizzo and W. L. Jorgensen, OPLS All-Atom Model for Amines: Resolution of the Amine Hydration Problem, J. Am. Chem. Soc. **121**, 4827 (1999).

[58] W. L. Jorgensen, D. S. Maxwell, and J. Tirado-Rives, Development and Testing of the OPLS All-Atom Force Field on Conformational Energetics and Properties of Organic Liquids, J. Am. Chem. Soc. **118**, 11225 (1996).

[59] W. L. Jorgensen, J. Chandrasekhar, J. D. Madura, R. W. Impey, and M. L. Klein, Comparison of Simple Potential Functions for Simulating Liquid Water, J. Chem. Phys. **79**, 926 (1983).

[60] M. W. Mahoney and W. L. Jorgensen, A Five-Site Model for Liquid Water and the Reproduction of the Density Anomaly by Rigid, Nonpolarizable Potential Functions, J. Chem. Phys. **112**, 8910 (2000).

[61] B. Chen, J. J. Potoff, and J. I. Siepmann, Monte Carlo Calculations for Alcohols and their Mixtures with Alkanes. Transferable Potentials for Phase Equilibria. 5. United-Atom Description of Primary, Secondary, and Tertiary Alcohols, J. Phys. Chem. B **105**, 3093 (2001).

[62] M. G. Martin and J. I. Siepmann, Transferable Potentials for Phase Equilibria. 1. United-Atom Description of n-Alkanes, J. Phys. Chem. B **102**, 2569 (1998).

[63] M. G. Martin and J. I. Siepmann, Novel Configurational-Bias Monte Carlo Method for Branched Molecules. Transferable Potentials for Phase Equilibria. 2. United-Atom Description of Branched Alkanes, J. Phys. Chem. B **103**, 4508 (1999).

[64] B. Chen and J. I. Siepmann, Transferable Potentials for Phase Equilibria. 3. Explicit-Hydrogen Description of Normal Alkanes, J. Phys. Chem. B **103**, 5370 (1999).

[65] N. Metropolis, A. W. Rosenbluth, M. N. Rosenbluth, A. H. Teller, and E. Teller, Equation of State Calculations by Fast Computing Machines, J. Chem. Phys. **21**, 1087 (1953).

[66] J. K. Johnson, A. Z. Panagiotopoulos, and K. E. Gubbins, Reactive Canonical Monte Carlo - A New Simulation Technique for Reacting or Associating Fluids, Mol. Phys. **81**, 717 (1994).

[67] N. Hansen, S. Jakobtorweihen, and F. J. Keil, Reactive Monte Carlo and Grand-Canonical Monte Carlo Simulations of the Propene Metathesis Reaction System, J. Chem. Phys. **122**, 1 (2005).

[68] S. Jakobtorweihen, N. Hansen, and F. J. Keil, Combining Reactive and Configurational-Bias Monte Carlo: Confinement Influence on the Propene Metathesis Reaction System in Various Zeolites, J. Chem. Phys. **125**, 1 (2006).

[69] S. P. Balaji, S. Gangarapu, M. Ramdin, A. Torres-Knoop, H. Zuilhof, E. L. V. Goetheer, D. Dubbeldam, and T. J. H. Vlugt, Simulating the Reactions of $CO_2$ in Aqueous Monoethanolamine Solution by Reaction Ensemble Monte Carlo using the Continuous Fractional Component method, J. Chem. Theory Comput. **11**, 2661 (2015).

[70] A. Torres-Knoop, S. P. Balaji, T. J. H. Vlugt, and D. Dubbeldam, A Comparison of Advanced Monte Carlo Methods for Open Systems: CFCMC vs CBMC, J. Chem. Theory Comput. **10**, 942 (2014).

[71] Q. Chen, S. P. Balaji, M. Ramdin, J. J. Gutierrez-Sevillano, A. Bardow, E. L. V. Goetheer, and T. J. H. Vlugt, Validation of the $CO_2/N_2O$ Analogy Using Molecular Simulation, Ind. Eng. Chem. Res. **53**, 18081 (2014).

[72] R. Krishna and J. A. Wesselingh, The Maxwell-Stefan Approach to Mass Transfer, Chem. Eng. Sci. **52**, 861 (1997).

[73] R. Taylor and R. Krishna, *Multicomponent Mass Transfer* (Wiley: New York, 1993).

[74] G. A. Fernández, J. Vrabec, and H. Hasse, Self-Diffusion and Binary Maxwell-Stefan Diffusion Coefficients of Quadrupolar Real Fluids from Molecular Simulation, Int. J. Thermophys. **26**, 1389 (2005).

[75] I. M. J. J. van de Ven-Lucassen, T. J. H. Vlugt, A. J. J. van der Zanden, and P. J. A. M. Kerkhof, Using Molecular Dynamics to Obtain Maxwell-Stefan Diffusion Coefficients in Liquid Systems, Mol. Phys. **94**, 495 (1998).

[76] R. Krishna and J. M. van Baten, The Darken Relation for Multicomponent Diffusion in Liquid Mixtures of Linear Alkanes. An Investigation using Molecular Dynamics (MD) simulations., Ind. Eng. Chem. Res. **44**, 6939 (2005).

[77] D. Dubbeldam, A. Torres-Knoop, and K. S. Walton, On the Inner Workings of Monte Carlo Codes, Mol. Sim. **39**, 1253 (2013).

[78] W. Shi and E. J. Maginn, Continuous Fractional Component Monte Carlo: An Adaptive Biasing Method for Open System Atomistic Simulations, J. Chem. Theory Comput. **3**, 1451 (2007).

[79] W. Shi and E. J. Maginn, Improvement in Molecule Exchange Efficiency in Gibbs Ensemble Monte Carlo: Development and Implementation of the Continuous Fractional Component Move, J. Comput. Chem. **29**, 2520 (2008).

[80] M. Lisal, I. Nezbeda, and W. R. Smith, The Reaction Ensemble Method for the Computer Simulation of Chemical and Phase Equilibria. II. The $Br_2$+$Cl_2$+BrCl System, J. Chem. Phys. **110**, 8597 (1999).

[81] T. W. Rosch and E. J. Maginn, Reaction Ensemble Monte Carlo Simulation of Complex Molecular Systems, J. Chem. Theory Comput. **7**, 269 (2011).

[82] G. F. Versteeg and W. P. M. van SwaaiJ, Solubility and Diffusivity of Acid Gases ($CO_2$, $N_2O$) in Aqueous Alkanolamine Solutions, J. Chem. Eng. Data **33**, 29 (1988).

[83] S. P. Balaji, S. K. Schnell, E. S. McGarrity, and T. J. H. Vlugt, A Direct Method for Calculating Thermodynamic Factors for Liquid Mixtures using the Permuted Widom Test Particle Insertion Method, Mol. Phys. **111**, 285 (2013).

[84] S. P. Balaji, S. K. Schnell, and T. J. H. Vlugt, Calculating Thermodynamic Factors of Ternary and Multicomponent Mixtures using the Permuted Widom Test Particle Insertion Method, Theor. Chem. Acc. **132**, 1 (2013).

[85] S. K. Schnell, P. Englebienne, J. M. Simon, P. Kruger, S. P. Balaji, S. Kjelstrup, D. Bedeaux, A. Bardow, and T. J. H. Vlugt, How to Apply the Kirkwood-Buff Theory to Individual Species in Salt Solutions, Chem. Phys. Lett. **582**, 154 (2013).

[86] R. E. Treybal, *Mass Transfer Operations* (McGraw-Hill Book Company, New York; 3rd edition, 1980).

[87] R. Krishna and G. L. Standart, Mass and Energy Transfer in Multicomponent Systems, Chem. Eng. Commun. **3**, 201 (1979).

[88] X. Liu, S. K. Schnell, J.-M. Simon, D. Bedeaux, S. Kjelstrup, A. Bardow, and T. J. H. Vlugt, Fick Diffusion Coefficients of Liquid Mixtures Directly Obtained From Equilibrium Molecular Dynamics, J. Phys. Chem. B **115**, 12921 (2011).

[89] X. Liu, T. J. H. Vlugt, and A. Bardow, Predictive Darken Equation for Maxwell-Stefan Diffusivities in Multicomponent Mixtures, Ind. Eng. Chem. Res. **50**, 10350 (2011).

[90] X. Liu, T. J. H. Vlugt, and A. Bardow, Maxwell-Stefan Diffusivities in Binary Mixtures of Ionic Liquids with Dimethyl Sulfoxide (DMSO) and $H_2O$, J. Phys. Chem. B **115**, 8506 (2011).

[91] X. Liu, A. Martin-Calvo, E. McGarrity, S. K. Schnell, S. Calero, J.-M. Simon, D. Bedeaux, S. Kjelstrup, A. Bardow, and T. J. H. Vlugt, Fick Diffusion Coefficients in Ternary Liquid Systems from Equilibrium Molecular Dynamics Simulations, Ind. Eng. Chem. Res. **51**, 10247 (2012).

[92] X. Liu, S. K. Schnell, J. M. Simon, P. Krüger, D. Bedeaux, S. Kjelstrup, A. Bardow, and T. J. H. Vlugt, Diffusion Coefficients from Molecular Dynamics Simulations in Binary and Ternary Mixtures, Int. J. Thermophys. **34**, 1169 (2013).

[93] R. Taylor and H. A. Kooijman, Composition Derivatives of Activity Coefficient Models (For the Estimation of Thermodynamic Factors in Diffusion), Chem. Eng. Commun. **102**, 87 (1991).

[94] X. Liu, T. J. H. Vlugt, and A. Bardow, Maxwell-Stefan Diffusivities in Liquid Mixtures: Using Molecular Dynamics for Testing Model Predictions, Fluid Phase Equilib. **301**, 110 (2011).

[95] D. J. Keffer and P. Adhangale, The Composition Dependence of Self and Transport Diffusivities from Molecular Dynamics Simulations, Chem. Eng. J. **100**, 51 (2004).

[96] D. J. Keffer, B. J. Edwards, and P. Adhangale, Determination of Statistically Reliable Transport Diffusivities from Molecular Dynamics Simulation, J. Non-Newtonian Fluid Mech. **120**, 41 (2004).

[97] D. R. Wheeler and J. Newman, Molecular Dynamics Simulations of Multicomponent Diffusion. 1. Equilibrium Method, J. Phys. Chem. B **108**, 18353 (2004).

[98] D. R. Wheeler and J. Newman, Molecular Dynamics Simulations of Multicomponent Diffusion. 2. Nonequilibrium Method, J. Phys. Chem. B **108**, 18362 (2004).

[99] A. Bardow, E. Kriesten, M. A. Voda, F. Casanova, B. Blümich, and W. Marquardt, Prediction of Multicomponent Mutual Diffusion in Liquids: Model Discrimination using NMR Data, Fluid Phase Equilib. **278**, 27 (2009).

[100] O. O. Medvedev and A. A. Shapiro, Modeling Diffusion Coefficients in Binary Mixtures, Fluid Phase Equilib. **225**, 13 (2004).

[101] S. K. Schnell, T. J. H. Vlugt, J.-M. Simon, D. Bedeaux, and S. Kjelstrup, Thermodynamics of Small Systems Embedded in a Reservoir: A Detailed Analysis of Finite Size Effects, Mol. Phys. **110**, 1069 (2011).

[102] S. K. Schnell, X. Liu, J.-M. Simon, A. Bardow, D. Bedeaux, T. J. H. Vlugt, and S. Kjelstrup, Calculating Thermodynamic Properties from Fluctuations at Small Scales, J. Phys. Chem. B **115**, 10911 (2011).

[103] S. K. Schnell, T. J. H. Vlugt, J.-M. Simon, D. Bedeaux, and S. Kjelstrup, Thermodynamics of A Small System in a $\mu$T Reservoir, Chem. Phys. Lett. **504**, 199 (2011).

[104] P. Kruger, S. K. Schnell, D. Bedeaux, S. Kjelstrup, T. J. H. Vlugt, and J. M. Simon, Kirkwood-Buff Integrals for Finite Systems, J. Phys. Chem. Lett. **4**, 235–238 (2013).

[105] R. Wedberg, J. P. O'Connell, G. H. Peters, and J. Abildskov, Accurate Kirkwood-Buff Integrals from Molecular Simulations, Mol. Sim. **36**, 1243 (2010).

[106] R. Wedberg, J. P. O'Connell, G. H. Peters, and J. Abildskov, Total and Direct Correlation Function Integrals from Molecular Simulation of Binary Systems, Fluid Phase Equilib. **302**, 32 (2011).

[107] S. Christensen, G. H. Peters, F. Y. Hansen, J. P. O'Connell, and J. Abildskov, State Conditions Transferability of Vapor-Liquid Equilibria via Fluctuation Solution Theory with Correlation Function Integrals from Molecular Dynamics Simulation, Fluid Phase Equilib. **260**, 169 (2007).

[108] S. Christensen, G. H. Peters, F. Y. Hansen, J. P. O'Connell, and J. Abildskov, Generation of Thermodynamics Data for Organic Liquid Mixtures From Molecular Simulations, Mol. Sim. **33**, 449 (2007).

[109] S. Hempel, J. Fischer, D. Paschek, and G. Sadowski, Activity Coefficients of Complex Molecules by Molecular Simulation and Gibbs-Duhem Integration, Soft Materials **10**, 26 (2012).

[110] A. Ben-Naim, *Molecular Theory of Solutions* (Oxford University Press, New York; 1st edition, 2006).

[111] P. G. Kusalik and G. N. Patey, The Thermodynamic Properties of Electrolyte Solutions: Some Formal Results, J. Chem. Phys. **86**, 5110 (1987).

[112] E. Ruckenstein and I. Shulgin, Entrainer effect in supercritical mixtures, Fluid Phase Equilib. **180**, 345 (2001).

[113] S. K. Lele, Compact Finite Difference Schemes with Spectral-like Resolution, J. Comput. Phys. **103**, 16 (1992).

[114] J. D. Weeks, D. Chandler, and H. C. Andersen, Role of repulsive forces in determining the equilibrium structure of simple liquids, J. Chem. Phys. **54**, 5237 (1971).

[115] J. I. Siepmann and D. Frenkel, Configurational Bias Monte-Carlo - A New Sampling Scheme for Flexible Chains, Mol. Phys. **75**, 59 (1992).

[116] M. N. Rosenbluth and A. W. Rosenbluth, Monte Carlo Simulations of the Average Extension of Molecular Chains, J. Chem. Phys. **23**, 356 (1955).

[117] D. Dubbeldam, S. Calero, D. E. Ellis, and R. Q. Snurr, RASPA 1.0: Molecular Simulation Software for Adsorption and Diffusion in Flexible Nanoporous Materials, Mol. Sim. (2015), 10.1080/0892702.2015.1010082, in press.

[118] J. Harris and S. A. Rice, A Lattice Model of a Supported Monolayer of Amphiphile Molecules: Monte Carlo Simulations, J. Chem. Phys. **88**, 1298 (1988).

[119] J. I. Siepmann, A Method for the Direct Calculation of Chemical-Potentials for Dense Chain Systems, Mol. Phys. **70**, 1145 (1990).

[120] D. Frenkel, G. C. A. M. Mooij, and B. Smit, Novel Scheme to Study Structural and Thermal-Properties of Continuously Deformable Molecules, J. Phys.: Condens. Matter **4**, 3053 (1992).

[121] J. J. de Pablo, M. Suter, and U. W. Suter, Simulation of Polyethylene Above and Below the Melting Point, J. Chem. Phys. **96**, 2395 (1992).

[122] M. Laso, J. J. de Pablo, and U. W. Suter, Simulation of Phase-Equilibria for Chain Molecules, J. Phys.: Condens. Matter **97**, 2817 (1992).

[123] J. I. Siepmann and I. R. McDonald, Monte Carlo Simulation of Mixed Monolayers, Mol. Phys. **75**, 255 (1992).

[124] T. J. H. Vlugt, R. Krishna, and B. Smit, Molecular Simulations of Adsorption Isotherms for Linear and Branched Alkanes and their Mixtures in Silicalite, J. Phys. Chem. B **103**, 1102 (1999).

[125] D. Dubbeldam, S. Calero, T. J. H. Vlugt, R. Krishna, T. L. M. Maesen, and B. Smit, United Atom Force Field for Alkanes in Nanoporous Materials, J. Phys. Chem. B **108**, 12301–12313 (2004).

[126] A. Z. Panagiotopoulos, Exact Calculations of Fluid-Phase Equilibria by Monte Carlo Simulation in a New Statistical Ensemble, Int. J. Thermophys. **10**, 447 (1989).

[127] J. J. de Pablo and J. M. Prausnitz, Phase Equilbria for Fluid Mixtures from Monte-Carlo Simulation, Fluid Phase Equilib. **53**, 177 (1989).

[128] A. Z. Panagiotopoulos, Gibbs ensemble techniques, in *Observation, Prediction and Simulation of Phase Transitions in Complex Fluids*, Vol. NATO ASI Series C,460, edited by L. R. M. Baus and J. Ryckaert (Kluwer Academic, Netherlands, 1995) pp. 463–501.

[129] M. G. Martin and J. I. Siepmann, Predicting Multicomponent Phase Equilibria and Free Energies of Transfer for Alkanes by Molecular Simulation, J. Am. Chem. Soc. **119**, 8921 (1997).

[130] M. D. Macedonia and E. J. Maginn, A Biased Grand Canonical Monte Carlo Method for Simulating Adsorption using All-Atom and Branched United Atom Models, Mol. Phys. **96**, 1375 (1999).

[131] T. J. H. Vlugt, M. G. Martin, B. Smit, J. I. Siepmann, and R. Krishna, Improving the Efficiency of the Configurational-Bias Monte Carlo Algorithm, Mol. Phys. **94**, 727 (1998).

[132] T. J. H. Vlugt, Efficiency of Parallel CBMC Simulations, Mol. Simulat. **23**, 63 (1999).

[133] S. Consta, T. J. H. Vlugt, J. Wichers-Hoeth, B. Smit, and D. Frenkel, Recoil Growth Algorithm for Chain Molecules with Continuous Interactions, Mol. Phys. **97**, 1243 (1999).

[134] M. W. Deem and J. S. Bader, A Configurational Bias Monte Carlo Method for Linear and Cyclic Peptides, Mol. Phys. **87**, 1245–1260 (1996).

[135] C. D. Wick and J. I. Siepmann, Self-Adapting Fixed-End-Point Configurational-Bias Monte Carlo Method for the Regrowth of Interior Segments of Chain Molecules with Strong Intramolecular Interactions, Macromolecules **33**, 7207 (2000).

[136] A. Uhlherr, Monte Carlo Conformational Sampling of the Internal Degrees of Freedom of Chain Molecules, Macromolecules **33**, 1351–1360 (2000).

[137] J. K. Shah and E. J. Maginn, A General and Efficient Monte Carlo Method for Sampling Intramolecular Degrees of Freedom of Branched ad Cyclic Molecules, J. Chem. Phys. **135**, 1 (2011).

[138] S. Jakobtorweihen, C. P. Lowe, F. J. Keil, and B. Smit, A Novel Algorithm to Model the Influence of Host Lattice Flexibility in Molecular Dynamics Simulations: Loading Dependence of Self-Diffusion in Carbon Nanotubes, J. Chem. Phys. **124**, 154706 (2006).

[139] M. G. Martin and A. L. Frischknecht, Using Arbitrary Trial Distributions to Improve Intramolecular Sampling in Configurational-Bias Monte Carlo, Mol. Phys. **104**, 2439 (2006).

[140] A. P. Lyubartsev, A. A. Martsinovski, S. V. Shevkunov, and P. N. Vorontsov-Velyaminov, New approach to Monte Carlo Calculation of the Free Energy: Method of Expanded Ensembles, J. Chem. Phys. **96**, 1776 (1992).

[141] F. A. Escobedo and J. J. de Pablo, Expanded Grand Canonical and Gibbs Ensemble Monte Carlo Simulation of Polymers, J. Chem. Phys. **105**, 4391 (1996).

[142] S. Duane, A. D. Kennedy, B. J. Pendleton, and D. Roweth, Hybrid Monte Carlo, Phys. Lett. B **195**, 216 (1987).

[143] S. Chempath, L. A. Clark, and R. Q. Snurr, Two General Methods for Grand Canonical Ensemble Simulation of Molecules with Internal Flexibility, J. Chem. Phys. **118**, 7635 (2003).

[144] F. Wang and D. P. Landau, Efficient, Multiple-Range Random Walk Algorithm to Calculate the Density of States, Phys. Rev. Lett. **86**, 2050 (2001).

[145] F. Wang and D. P. Landau, Determining the Density of States for Classical Statistical Models: A Random Walk Algorithm to Produce a Flat Histogram, Phys. Rev. E **64**, 056101 (2001).

[146] L. F. Rull, G. Jackson, and B. Smit, The Condition of Microscopic Reversibility in Gibbs Ensemble Monte Carlo Simulations of Phase Equilibria, Mol. Phys. **85**, 435 (1995).

[147] T. L. M. Maesen, E. Beerdsen, S. Calero, D. Dubbeldam, and B. Smit, Understanding Cage Effects in the n-Alkane Conversion on Zeolites, J. Catal. **237**, 278 (2006).

[148] B. Smit and T. L. M. Maesen, Commensurate Freezing of Alkanes in the Channels of a Zeolite, Nature **374**, 42 (1995).

[149] D. Dubbeldam, R. Krishna, S. Calero, and A. O. Yazaydin, Computer-Assisted Screening of Ordered Crystalline Nanoporous Adsorbents for Separation of Alkane Isomers, Angew. Chem. Int. Ed. **51**, 11867 –11871 (2012).

[150] Z. R. Herm, B. M. Wiers, J. A. Mason, J. M. van Baten, M. R. Hudson, P. Zajdel, C. M. Brown, N. Masciocchi, R. Krishna, and J. R. Long, Separation of Hexane Isomers in a Metal-Organic Framework with Triangular Channels, Science **340**, 960 (2013).

[151] S. L. Mayo, B. D. Olafson, and W. A. Goddard, DREIDING: A Generic Force Field for Molecular Simulations, J. Phys. Chem. **94**, 8897 (1990).

[152] A. K. Rappé, C. J. Casewit, K. S. Colwell, W. A. Goddard, and W. M. J. Skiff, UFF, a Full Periodic Table Force Field for Molecular Mechanics and Molecular Dynamics Simulations, J. Am. Chem. Soc. **114**, 10024 (1992).

[153] H. A. Lorentz, Ueber die Anwendung des Satzes vom Virial in der kinetischen Theorie der Gase, Ann. Phys. **12**, 127 (1881).

[154] D. Berthelot, Sur le Melange des Gaz., C. R. Hebd. Sceances Acad. Sci. **126**, 1703 (1898).

[155] M. Meinshausen, N. Meinshausen, W. Hare, S. C. B. Raper, K. Frieler, R. Knutti, D. J. Frame, and M. R. Allen, Greenhouse-Gas Emission Targets for Limiting Global Warming to 2° C, Nature **458**, 1156 (2009).

[156] S. Solomon, Irreversible Climate Change due to Carbon Dioxide Emissions, Proc. Natl. Acad. Sci. **106**, 1704 (2009).

[157] B. Metz, O. Davidson, H. de Coninck, M. Loos, and L. Meyer, *Carbon Dioxide Capture and Storage: Special Report of the Intergovernmental Panel on Climate Change* (Cambridge University Press: Cambridge, 2005).

[158] G. Puxty, R. Rowland, A. Allport, Q. Yang, M. Bown, R. Burns, M. Maeder, and M. Attalla, Carbon Dioxide Post-combustion Capture: A Novel Screening Study of the Carbon Dioxide Absorption Performance of 76 Amines, Environ. Sci. Technol. **43**, 6427 (2009).

[159] G. T. Rochelle, Amine Scrubbing for $CO_2$ Capture, Science **325**, 1652 (2009).

[160] W. Böttinger, M. Maiwald, and H. Hasse, Online NMR Spectroscopic Study of Species Distribution in MEA-$H_2O$-$CO_2$ and DEA-$H_2O$-$CO_2$, Fluid Phase Equilib. **263**, 131 (2008).

[161] P. Khakharia, L. Brachert, J. Mertens, A. Huizinga, B. Schallert, K. Schaber, T. J. H. Vlugt, and E. L. V. Goetheer, Investigation of Aerosol Based Emission of MEA Due to Sulphuric Acid Aerosol and Soot in a Post-combustion $CO_2$ Capture Process, Int. J. Greenhouse Gas Control **19**, 138 (2013).

[162] P. Khakharia, H. M. Kvamsdal, E. F. da Silva, T. J. H. Vlugt, and E. L. V. Goetheer, Field Study of a Brownian Demister Unit to Reduce Aerosol Based Emission From a Post-combustion $CO_2$ Capture Plant, Int. J. Greenhouse Gas Control **28**, 57 (2014).

[163] P. Khakharia, A. Huizinga, C. J. Lopez, C. S. Sanchez, F. de Miguel Mercader, T. J. H. Vlugt, and E. L. V. Goetheer, Acid Wash Scrubbing as a Countermeasure for Ammonia Emissions from a Post-combustion $CO_2$ Capture Plant, Ind. Eng. Chem. Res. **53**, 13195 (2014).

[164] S. Gangarapu, A. T. M. Marcelis, and H. Zuilhof, Improving the Capture of $CO_2$ by Substituted Monoethanolamines: Electronic Effects of Fluorine and Methyl Substituents, ChemPhysChem **13**, 3973 (2012).

[165] S. Gangarapu, A. T. M. Marcelis, and H. Zuilhof, Carbamate Stabilities of Sterically Hindered Amines from Quantum Chemical Methods: Relevance for $CO_2$ Capture, ChemPhysChem **14**, 3936 (2013).

[166] G. Manzolini, E. S. Fernandez, S. Rezvani, E. Macchi, E. L. V. Goetheer, and T. J. H. Vlugt, Economic Assessment of Amine Based $CO_2$ Capture Technologies in Power Plants Based on European Benchmarking Task Force Methodology, Appl. Energy **138**, 546 (2014).

[167] J. P. Jakobsen, J. Krane, and H. F. Svendsen, Liquid-Phase Composition Determination in $CO_2$-$H_2O$-Alkanolamine Systems: An NMR Study, Ind. Eng. Chem. Res. **44**, 9894 (2005).

[168] R. Car and M. Parinello, Unified Approach for Molecular Dynamics and Density-Functional Theory, Phys. Rev. Lett. **55**, 2471 (1985).

[169] A. C. van Duin, S. Dasgupta, F. Lorant, and W. A. Goddard, ReaxFF: A Reactive Force Field for Hydrocarbons, J. Phys. Chem. A **105**, 9396 (2001).

[170] W. R. Smith and B. Triska, The Reaction Ensemble Method for the Computer Simulation of Chemical and Phase Equilibria. 1. Theory and Basic Examples, J. Chem. Phys. **100**, 3019 (1994).

[171] C. H. Turner, J. K. Johnson, and K. E. Gubbins, Effect of Confinement on Chemical Reaction Equilibria: The Reactions $2NO \rightarrow N_2O_2$ and $N_2+3H_2 \rightarrow 2NH_3$ in Carbon Micropores, J. Chem. Phys. **114**, 1851 (2001).

[172] J. Carrero-Mantilla and M. Llano-Restrepo, Vapor-phase Chemical Equilibrium for the Hydrogenation of Benzene to Cyclohexane from Reaction-Ensemble Molecular Simulation, Fluid Phase Equilib. **219**, 181 (2004).

[173] M. Lisal, J. K. Brennan, and W. R. Smith, Chemical Reaction Equilibrium in Nanoporous Materials: NO Dimerization Reaction in Carbon Slit Nanopores, J. Chem. Phys. **124**, 064712 (2006).

[174] M. Lisal, W. R. Smith, and I. Nezbeda, Molecular Simulation of Multicomponent Reaction and Phase Equilibria in MTBE Ternary System, AIChE J. **46**, 866 (2000).

[175] M. Lisal, W. R. Smith, and I. Nezbeda, Accurate Computer Simulation of Phase Equilibrium for Complex Fluid Mixtures. Application to Binaries Involving Isobutene, Methanol, Methyl tert-Butyl Ether, and n-Butane, J. Phys. Chem. B **103**, 10496 (1999).

[176] S. I. Sandler, *Chemical, Biochemical, and Engineering Thermodynamics* (Wiley, 2006).

[177] M. J. Frisch, G. W. Trucks, H. B. Schlegel, G. E. Scuseria, M. A. Robb, J. R. Cheeseman, G. Scalmani, V. Barone, B. Mennucci, G. A. Petersson, H. Nakatsuji, M. Caricato, X. Li, H. P. Hratchian, A. F. Izmaylov, J. Bloino, G. Zheng, J. L. Sonnenberg, M. Hada, M. Ehara, K. Toyota, R. Fukuda, J. Hasegawa, M. Ishida, T. Nakajima, Y. Honda, O. Kitao, H. Nakai, T. Vreven, J. A. M. Jr., J. E. Peralta, F. Ogliaro, M. Bearpark, J. J. Heyd, E. Brothers, K. N. Kudin, V. N. Staroverov, R. Kobayashi, J. Normand, K. Raghavachari, A. Rendell, J. C. Burant, S. S. Iyengar, J. Tomasi, M. Cossi, N. Rega, J. M. Millam, M. Klene, J. E. Knox, J. B. Cross, V. Bakken, C. Adamo, J. Jaramillo, R. Gomperts, R. E. Stratmann, O. Yazyev, A. J. Austin, R. Cammi, C. Pomelli, J. W. Ochterski, R. L. Martin, K. Morokuma, V. G. Zakrzewski, G. A. Voth, P. Salvador, J. J. Dannenberg, S. Dapprich, A. D. Daniels, O. Farkas, J. B. Foresman, J. V. Ortiz, J. Cioslowski, and D. J. Fox, GAUSSIAN 09 Revision D.01 (2009), Gaussian Inc. Wallingford CT.

[178] J. W. Ochterski, Thermochemistry in Gaussian, http://www.gaussian.com/g_whitepap/thermo/thermo.pdf (accessed January 3, 2015).

[179] C. H. Turner, J. K. Brennan, M. Lisal, W. R. Smith, J. K. Johnson, and K. E. Gubbins, Simulation of Chemical Reaction Equilibria by the Reaction Ensemble Monte Carlo Method: A Review, Mol. Sim. **34**, 119 (2008).

[180] J. E. Mayer and M. G. Mayer, *Statistical Mechanics* (Wiley, New York, 1963).

[181] J. J. Potoff and J. I. Siepmann, Vapor-Liquid Equilibria of Mixtures Containing Alkanes, Carbon Dioxide, and Nitrogen, AIChE J. **47**, 1676 (2001).

[182] R. Vacha, V. Buch, A. Milet, J. P. Devlind, and P. Jungwirth, Autoionization at the Surface of Neat Water: Is the Top Layer pH Neutral, Basic, or Acidic?, Phys. Chem. Chem. Phys. **9**, 4736 (2007).

[183] P. P. Ewald, Die Berechnung Optischer und Elektrostatischer Gitterpotentiale, Ann. Phys **64**, 253 (1921).

[184] T. L. Hill, *An Introduction to Statistical Thermodynamics* (Dover: New York (Reprint), 1987).

[185] R. Wiebe and V. L. Gaddy, The Solubility of Carbon Dioxide in Water at Various Temperatures from 12 to $40^o$ and at Pressures to 500 Atmospheres. Critical Phenomena, J. Am. Chem. Soc. **65**, 815–817 (1940).

[186] R. S. Haszeldine, Carbon Capture and Storage: How Green Can Black Be?, Science **325**, 1647 (2009).

[187] L. M. Romeo, I. Bolea, and J. M. Escosa, Integration of Power Plant and Amine Scrubbing to Reduce $CO_2$ Capture Costs, Appl. Ther. Eng. **28**, 1039 (2008).

[188] N. M. Haimour, Solubility of Nitrous Oxide in Aqueous Solutions of Diethanolamine at Different Temperatures, J. Chem. Eng. Data **35**, 177 (1990).

[189] G. E. H. Joosten and P. V. Danckwerts, Solubility and Diffusivity of Nitrous Oxide in Equimolar Potassium Carbonate-Potassium Bicarbonate Solutions at 25°C and 1 atm, J. Chem. Eng. Data **17**, 452 (1972).

[190] E. Sada, H. Kumazawa, and M. A. Butt, Solubilities of Gases in Aqueous Solutions of Amine, J. Chem. Eng. Data **22**, 277 (1977).

[191] E. Sada, H. Kumazawa, and M. A. Butt, Solubility and Diffusivity of Gases in Aqueous Solutions of Amines, J. Chem. Eng. Data **23**, 161 (1978).

[192] S. S. Laddha, J. M. Diaz, and P. V. Danckwerts, The $N_2O$ Analogy: The Solubilities of $CO_2$ and $N_2O$ in Aqueous Solutions of Organic Compounds, Chem. Eng. Sci. **36**, 228 (1981).

[193] G. J. Browning and R. H. Weiland, Physical Solubility of Carbon Dioxide in Aqueous Alkanolamines via Nitrous Oxide Analogy, J. Chem. Eng. Data **39**, 817 (1994).

[194] W. Shi and E. J. Maginn, Atomistic Simulation of the Absorption of Carbon Dioxide and Water in the Ionic Liquid 1-n-Hexyl-3-methylimidazolium Bis(trifluoromethylsulfonyl)imide ([hmim][Tf2N]), J. Phys. Chem. B **112**, 2045 (2008).

[195] M. Lisal, W. R. Smith, and K. Aim, Analysis of Henry's Constant for Carbon Dioxide in Water via Monte Carlo Simulation, Fluid Phase Equilib. **226**, 161 (2004).

[196] E. C. Cichowski, T. R. Schmidt, and J. R. Errington, Determination of Henry's law Constants through Transition Matrix Monte Carlo Simulation, Fluid Phase Equilib. **236**, 58 (2005).

[197] L. Zhang and J. I. Siepmann, Direct Calculation of Henry's Law Constants from Gibbs Ensemble Monte Carlo Simulations: Nitrogen, Oxygen, Carbon Dioxide and Methane in Ethanol, Theor. Chem. Acc. **115**, 391 (2006).

[198] H. Liu and E. J. Maginn, A Molecular Dynamics Investigation of the Structural and Dynamic Properties of the Ionic Liquid 1-n-Butyl-3-methylimidazolium Bis(trifluoromethanesulfonyl)imide, J. Chem. Phys. **135**, 124507 (2011).

[199] M. in het Panhuis, C. H. Patterson, and R. M. Lynden-Bell, A Molecular Dynamics Study of Carbon Dioxide in Water: Diffusion, Structure and Thermodynamics, Mol. Phys. **94**, 963 (1998).

[200] L. Vlcek, A. A. Chialvo, and D. R. Cole, Optimized Unlike-pair Interactions for Water-Carbon Dioxide Mixtures Described by the SPC/E and EPM2 Models, J. Phys. Chem. B **115**, 8775 (2011).

[201] R. E. Zeebe, On the Molecular Diffusion Coefficients of Dissolved $CO_2$, $HCO_3^-$, and $CO_3^{2-}$ and their Dependence on Isotopic Mass, Geochim. et Cosmochim. Acta **75**, 2483 (2011).

[202] O. A. Moultos, I. N. Tsimpanogiannis, A. Z. Panagiotopoulos, and I. G. Economou, Atomistic Molecular Dynamics Simulations of $CO_2$ Diffusivity in $H_2O$ for a Wide Range of Temperatures and Pressures, J. Phys. Chem. B **118**, 5532 (2014).

[203] D. Peng and D. B. Robinson, A New Two-Constant Equation of State, Ind. Eng. Chem. Fundam. **15**, 59 (1976).

[204] H. J. C. Berendsen, J. R. Grigera, and T. P. Straatsma, The Missing Term in Effective Pair Potentials, J. Phys. Chem. **91**, 6269 (1987).

[205] J. G. Harris and K. H. Yung, Carbon Dioxide's Liquid-Vapor Coexistence Curve And Critical Properties as Predicted by a Simple Molecular Model, J. Phys. Chem. **99**, 12021 (1995).

[206] V. Lachet, B. Creton, T. de Bruin, E. Bourasseau, N. Desbiens, O. Wilhelmsen, and M. Hammer, Equilibrium and Transport Properties of $CO_2$+$N_2O$ and $CO_2$+NO Mixtures: Molecular Simulation and Equation of State Modelling Study, Fluid Phase Equilib. **322-323**, 66 (2012).

[207] J. O. Hirschfelder, C. F. Curtiss, and R. B. Bird, *The Molecular Theory of Gases and Liquids* (John Wiley and Sons: New York, 1st edition, 1954).

[208] T. Darden, D. York, and L. Pedersen, Particle mesh Ewald: An N · log(N) Method for Ewald Sums in Large Systems, J. Chem. Phys. **98**, 10089 (1993).

[209] E. Apol, R. Apostolov, H. J. C. Berendsen, A. van Buuren, P. Bjelkmar, R. van Drunen, A. Feenstra, G. Groenhof, P. Kasson, P. Larsson, P. Meulenhoff, T. Murtola, S. Pall, S. Pronk, R. Schulz, M. Shirts, A. Sijbers, P. Tieleman, B. Hess, D. van der Spoel, and E. Lindahl, Gromacs User Manual version 4.5.4 (2010), `http://wwww.gromacs.org` (accessed on February 1, 2012).

[210] M. D. Hanwell, D. E. Curtis, D. C. Lonie, T. van der Meersch, E. Zurek, and G. R. Hutchison, Avogadro: An Advanced Semantic Chemical Editor, Visualization, and Analysis Platform, J. Cheminformatics **4**, 17 (2012).

[211] P. D. Vaidya and E. Y. Kenig, $CO_2$-Alkanolamine Reaction Kinetics: A Review of Recent Studies, Chem. Eng. Technol. **30**, 1467 (2007).

[212] T. G. Amundsen, L. E. Øi, and D. A. Eimer, Density and Viscosity of Monoethanolamine + Water + Carbon Dioxide from (25 to 80) °C, J. Chem. Eng. Data **54**, 3096–3100 (2009).

[213] J. J. Carroll, J. D. Slupsky, and A. E. Mather, The Solubility of Carbon Dioxide in Water at Low Pressure, J. Phys. Chem. Ref. Data **20**, 1201 (1991).

[214] B. G. D. Roizard, F. Lapicque, E. Favre, R. Cadours, P. Boucot, and P. L. Carrette, $CO_2$ Capture in Flue Gas: Semiempirical Approach to Select a Potential Physical Solvent, Ind. Eng. Chem. Res. **45**, 5044 (2006).

[215] W. Wagner and A. Pruss, The IAPWS Formulation 1995 for the Thermodynamic Properties of Ordinary Water Substance for General and Scientific Use, J. Phys. Chem. Ref. Data **31**, 387 (2002).

[216] M. B. King and H. Al-Najjar, The Solubilities of Carbon Dioxide, Hydrogen Sulphide and Propane in some normal Alkane Solvents - I: Experimental Determinations in the Range $15 - 70°$ C and Comparison with Ideal Solution Values, Chem. Eng. Sci. **32**, 1241 (1977).

[217] L. C. Yen and J. J. McKetta Jr., Solubility of Nitrous Oxide in Some Nonpolar Solvents, J. Chem. Eng. Data **7**, 288 (1962).

[218] D. Dubbeldam, D. C. Ford, D. E. Ellis, and R. Q. Snurr, A New Perspective on the Order-n Algorithm for Computing Correlation Functions, Mol. Sim. **35**, 1084 (2009).

[219] E. D. Snijder, M. J. M. te Riele, G. F. Versteeg, and W. P. M. van Swaaij, Diffusion Coefficients of CO, $CO_2$, $N_2O$, and $N_2$ in Ethanol and Toluene, J. Chem. Eng. Data **40**, 37 (1995).

[220] C. R. Wilke and P. Chang, Correlation of Diffusion Coefficients in Dilute Solutions, AIChE J. **1**, 264 (1955).

[221] B. E. Poling, J. M. Prausnitz, and J. P. O'Connell, *The Properties of Gases and Liquids Vol. 5* (McGraw-Hill: New York, 2001).

[222] C. W. Jones, $CO_2$ Capture from Dilute Gases as a Component of Modern Global Carbon Management, Annu. Rev. Chem. Biomol. Eng. **2**, 31 (2011).

[223] J. G. J. Olivier, G. Janssens-Maenhout, and J. A. H. W. Peters, *Trends in global $CO_2$ emissions; 2012 Report* (PBL Netherlands Environmental Assessment Agency, The Hague, The Netherlands, 2012).

[224] BP, *BP Energy Outlook 2035* (BP, London, United Kingdom, 2014) `http://www.bp.com/en/global/corporate/about-bp/energy-economics/energy-outlook.html` (accessed on April 15, 2015).

[225] R. Davidson, *Pre-combustion capture of $CO_2$ in IGCC plants* (IEA Clean Coal Centre, London, 2011).

[226] J. A. Moulijn, M. Makkee, and A. van Diepen, *Chemical Process Technology* (Wiley, Chichester, 2001).

[227] K. Liu, C. Song, and V. Subramani, *Hydrogen and Syngas Production and Purification Technologies* (Wiley, Hoboken, 2010).

[228] P. Nugent, Y. Belmabkhout, S. D. Burd, A. J. Cairns, R. Luebke, K. Forrest, T. Pham, S. Ma, B. Space, L. Wojtas, and *et al.*, Porous Materials with Optimal Adsorption Thermodynamics and Kinetics for $CO_2$ Separation, Nature **495**, 80 (2013).

[229] S. Vora, L. Brickett, P. Indrikanti, R. Munson, J. Murphy, T. Rife, J. Strock, and C. Zaremsky, *DOE/NETL Advanced Carbon Dioxide Capture R&D Program: Technology Update*, Tech. Rep. (U.S. Department of Energy/National Energy Technology Laboratory, Pittsburgh, PA, 2013).

[230] K. Sumida, D. L. Rogow, J. A. Mason, T. M. McDonald, E. D. Bloch, Z. R. Herm, T. Bae, and J. R. Long, Carbon Dioxide Capture in Metal-Organic Frameworks, Chem. Rev. **112**, 724 (2012).

[231] Z. R. Herm, J. A. Swisher, B. Smit, R. Krishna, and J. R. Long, Metal-Organic Frameworks as Adsorbents for Hydrogen Purification and Precombustion Carbon Dioxide Capture, J. Am. Chem. Soc. **133**, 5664 (2011).

[232] A. Martín-Calvo, F. D. Lahoz-Martín, and S. Calero, Understanding Carbon Monoxide Capture Using Metal-Organic Frameworks, J. Phys. Chem. C **116**, 6655 (2012).

[233] R. F. Cracknell, Molecular Simulation of Hydrogen Adsorption in Graphitic Nanofibres, Phys. Chem. Chem. Phys. **3**, 2091 (2001).

[234] G. Kamath, N. Lubna, and J. J. Potoff, Effect of Partial Charge Parametrization on the Fluid Phase Behavior of Hydrogen Sulfide, J. Chem. Phys. **123**, 124505 (2005).

[235] T. Kristof and J. Liszi, Effective Intermolecular Potential for Fluid Hyderogen Sulfide, J. Phys. Chem. B **101**, 5480 (1997).

[236] J. J. Gutiérrez-Sevillano, A. Martín-Calvo, D. Dubbeldam, S. Calero, and S. Hamad, Adsorption of Hydrogen Sulphide on Metal-Organic Frameworks, RSC Adv. **3**, 14737 (2013).

[237] I. Urukova, J. Vorholz, and G. Maurer, Solubility of $CO_2$, CO, and $H_2$ in the Ionic Liquid [bmim][$PF_6$] from Monte Carlo Simulations, J. Phys. Chem. B **109**, 12154 (2005).

[238] M. J. Earle, J. M. S. S. Esperanca, M. A. Gilea, J. N. Canongia Lopes, L. P. N. Rebelo, J. W. Magee, K. R. Seddon, and J. A. Widegren, The Distillation and Volatility of Ionic Liquids, Nature **439**, 831 (2006).

[239] S. Pronk, S. Páll, R. Schulz, P. Larsson, P. Bjelkmar, R. Apostolov, M. R. Shirts, J. C. Smith, P. M. Kasson, D. van der Spoel, B. Hess, and E. Lindahl, GROMACS 4.5: A High-Throughput and Highly Parallel Open Source Molecular Simulation Toolkit, Bioinformatics **29**, 845 (2013).

[240] S. Raeissi and C. J. Peters, Carbon Dioxide Solubility in the Homologous 1-Alkyl-3-methylimidazolium Bis(trifluoromethylsulfonyl)imide Family, J. Chem. Eng. Data **54**, 382 (2009).

[241] S. Raeissi and C. J. Peters, High Pressure Phase Behaviour of Methane in 1-Butyl-3-methylimidazolium Bis(trifluoromethylsulfonyl)imide, Fluid Phase Equilib. **294**, 67 (2010).

[242] S. Raeissi and C. J. Peters, Understanding Temperature Dependency of Hydrogen Solubility in Ionic Liquids, Including Experimental Data in [bmim][$Tf_2N$], AIChE J. **58**, 3553 (2012).

[243] S. Raeissi, L. J. Florusse, and C. J. Peters, Purification of Flue Gas by Ionic Liquids: Carbon Monoxide Capture in [bmim][$Tf_2N$], AIChE J. **59**, 3886 (2013).

[244] A. Finotello, J. E. Bara, D. Camper, and R. D. Noble, Room-Temperature Ionic Liquids: Temperature Dependence of Gas Solubility Selectivity, Ind. Eng. Chem. Res. **47**, 3453 (2008).

[245] J. Jacquemin, M. F. Costa Gomes, P. Husson, and V. Majer, Solubility of Carbon Dioxide, Ethane, Methane, Oxygen, Nitrogen, Hydrogen, Argon, and Carbon Monoxide in 1-Butyl-3-methylimidazolium tetrafluoroborate between Temperatures 283 K and 343 K and at Pressures Close to Atmospheric, J. Chem. Thermodyn. **38**, 490 (2006).

[246] J. Jacquemin, P. Husson, V. Majer, and M. F. Costa Gomes, Low-Pressure Solubilities and Thermodynamics of Solvation of Eight Gases in 1-Butyl-3-methylimidazolium Hexafluorophosphate, Fluid Phase Equilib. **240**, 87 (2006).

[247] A. H. Jalili, M. Rahmati-Rostami, C. Ghotbi, M. Hosseini-Jenab, and A. N. Ahmadi, Solubility of $H_2S$ in Ionic Liquids [bmim][$PF_6$], [bmim][$BF_4$], and [bmim][$Tf_2N$], J. Chem. Eng. Data **54**, 1844 (2009).

[248] A. V. Rayer, A. Henni, and P. Tontiwachwuthikul, High Pressure Physical Solubility of Carbon Dioxide ($CO_2$) in Mixed Polyethylene Glycol Dimethyl Ethers (Genosorb 1753), Can. J. Chem. Eng. **90**, 576 (2012).

[249] A. V. Rayer, A. Henni, and P. Tontiwachwuthikul, High-Pressure Solubility of Methane ($CH_4$) and Ethane ($C_2H_6$) in Mixed Polyethylene Glycol Dimethyl Ethers (Genosorb 1753) and Its Selectivity in Natural Gas Sweetening Operations, J. Chem. Eng. Data **57**, 764 (2012).

[250] I. Gainar and G. Anitescu, The Solubility of $CO_2$, $N_2$ and $H_2$ in a Mixture of Dimethylether Polyethylene Glycols at High Pressures, Fluid Phase Equilib. **109**, 281 (1995).

[251] Y. Xu, R. P. Schutte, and L. G. Hepler, Solubilities of Carbon Dioxide, Hydrogen Sulfide and Sulfur Dioxide in Physical Solvents, Can. J. Chem. Eng. **70**, 569 (1992).

# Summary

The increase in concentrations of greenhouse gases is responsible for global warming over the past few years. A major portion of the emitted greenhouse gases contains carbon dioxide ($CO_2$). The capture of carbon dioxide from the effluent sources, its transport, and storage has been identified as the most promising method to mitigate global warming by reducing the carbon footprint in the atmosphere. Carbon dioxide is mainly discharged as flue gas into the atmosphere from power plants which operate on coal, oil, and natural gas. Post-combustion $CO_2$ capture processes mainly use chemical solvents like monoethanolamine (MEA) to capture $CO_2$ from flue gas streams. The regeneration of $CO_2$ from the rich solvents is an energy intensive process which decreases the overall efficiency. Other issues like solvent volatility/corrosiveness, toxicity, and solvent costs are critical for choosing the best solvent for post-combustion capture. Chemical solvents like monoethanolamine have been used in the industry since early 1960's and are widely used today. There is a need for designing new solvents which are less energy intensive, less toxic and corrosive than the ones existing in the industry. Solvent design is extremely challenging, since there are potentially millions of molecules that can be used as a solvent for post-combustion $CO_2$ capture and to find the best solvent is extremely difficult from an experimental point of view. In this thesis, we develop advanced techniques and methods that can potentially be used to screen large number of solvent molecules and to potentially select the most promising ones. Existing molecular methods are insufficient to efficiently describe the chemisorption and diffusion of $CO_2$ in liquid solvents. We have developed new methods to study the different thermodynamic processes taking place between the $CO_2$ and solvent molecules.

To describe the interaction of $CO_2$ in different solvents, it is imperative to understand the various thermodynamic processes *i.e.* solubilities and diffusion of $CO_2$ with these solvents. The knowledge of Fick diffusion coefficients is important for designing mass transfer equipment in industry. The thermodynamic factor is needed for converting a gradient in chemical potential into a concentration gradient. Existing methods to compute thermodynamic factors which are used in calculating the Fick diffusivities are either inefficient, inaccurate or require a non-trivial interpretation of the results. In chapter 2, we have presented a new approach to compute the matrix of thermodynamic factors $[\Gamma]$ of $n$-component systems using the Permuted Widom particle insertion method. The key advantage of our approach is that we can compute the matrix of thermodynamic factors $[\Gamma]$ from a single simulation without any additional computational cost. We have computed the thermodynamic factors for binary and ternary Lennard-Jones systems and compared our results with the thermodynamic factors obtained from a numerical differentiation of activity coefficients using the central difference method and also with the physically-based NRTL model. The results for the thermodynamic factors from the methods are in excellent agreement. The Permuted Widom test particle insertion method also serves as an independent check to confirm the applicability of the newly formulated Kirkwood-

Buff theory for closed systems when applied to salt solutions.

Molecular simulations in open ensembles are convenient for the computation of thermodynamic properties of systems with $CO_2$. Efficiencies and accuracies of Monte Carlo methods in open ensembles crucially depend on the probability of successful insertions and deletions of molecules. At higher densities, these probabilities are very low due to overlaps with the existing molecules. Advanced methods like Configurational-Bias Monte Carlo (CBMC) and the Continuous Fractional Component Monte Carlo (CFCMC) have been developed to increase the efficiencies of insertions in high density systems. In chapter 3, we compare the efficiencies of CBMC and CFCMC at high densities. We have also developed a new method combining the Continuous Fractional Component Monte Carlo and Configurational-Bias (CB/CFCMC). We have derived the acceptance rules for this method in different ensembles and compared this method with CBMC and CFCMC. We find that, at medium and high densities, the efficiency of insertion can be summarized by CB/CFCMC > CFCMC > CBMC > MC. CB/CFCMC has a clear advantage for long chain molecules, since it avoids having to generate ideal gas configurations for the CFCMC insertions. Although this generation might be cheap, for increasing chain lengths the molecular configurations increasingly deviate from their ideal gas configuration. The CFCMC will be inefficient here while the CB/CFCMC could still work by growing the molecule atom by atom. These methods are extensively used in our research.

The chemisorption process using chemical solvents for post-combustion $CO_2$ capture is mainly driven by the reactions that take place between the $CO_2$, monoethanolamine (MEA) and water. For a complete molecular understanding on how a chemical absorption process works, it is necessary to obtain the equilibrium speciations of the different molecules and to study the impact of different reaction pathways. In chapter 4, Monte Carlo simulations in the Reaction Ensemble using a Continuous Fractional Component method (RxMC/CFC) are used to compute the equilibrium speciation of all relevant species in the chemisorption of $CO_2$ with aqueous MEA solutions. The RxMC/CFC method in combination with the osmotic ensemble is used to compute the absorption isotherms of $CO_2$ in an aqueous MEA solvent. An excellent agreement with experimental results was observed. This RxMC/CFC methodology opens up possibilities to investigate the effect of the solvents in the reactions. Chemisorption of $CO_2$ in different solvents can be studied computationally to obtain the equilibrium concentrations and absorption isotherms. Only the thermodynamics need to be considered here and the different transition states or reaction pathways can be ignored. This method may also investigate the effect of the chemistry of the amines, for example by adding different functional groups.

Establishing the physical solubilities and diffusivities of $CO_2$ in chemical solvents is extremely difficult using experiments since diffusion and absorption of $CO_2$ molecules in a chemical solvent take place simultaneously. Due to reactions between $CO_2$ and the chemical solvents, the solubility of $CO_2$ measured in experiments is the total solubility. The total solubility combines both physical and chemical absorption as there are almost no unreacted $CO_2$ molecules remaining. To calculate

the physical solubilities and diffusivities, the so-called "$CO_2/N_2O$ analogy" is used which replaces $CO_2$ with the molecularly similar $N_2O$. In this way, the thermodynamic properties of $CO_2$ are estimated from those of $N_2O$. In chapter 5, we aim to validate the "$CO_2/N_2O$ analogy" using molecular simulations. Molecular simulations are the only way to validate the analogy since molecular simulations allow the possibility to switch the reactions on or off, unlike in experiments. The CFCMC method in the osmotic ensemble and Molecular Dynamics simulations were used to predict the Henry coefficients and diffusivities respectively, of $CO_2$ and $N_2O$ in water, ethanol, *n*-heptane, and a 30% MEA solution (with chemical reactions involving $CO_2$-MEA-$H_2O$ turned off) at a temperature of 303 K. We find that Monte Carlo simulations correctly predict the $CO_2/N_2O$ solubilities in the investigated solvents. The solubility of $CO_2$ in the solvents follows the order: heptane > ethanol > 30% MEA (without chemical reactions) > water. Molecular Dynamics simulations also correctly predict the observed diffusivities of $CO_2$ and $N_2O$ in these solvents, which obeys the following order: heptane > ethanol > water > 30% MEA (without chemical reactions). The simulation results indicate that the $CO_2/N_2O$ analogy is valid for water and 30% MEA solution at 303 K (with reactions involving $CO_2$-MEA-$H_2O$ turned off) with ca. 10% error. We perform additional simulations to investigate the effect of a chemical reaction between $CO_2$ and MEA on the physical solubility and self-diffusivity of $CO_2$. The simulation results indicate that both the physical solubility and the self-diffusivity of $CO_2$ are lower in the system containing reaction products of $CO_2$ and MEA, which is a result of the reaction between $CO_2$ and MEA.

The Monte Carlo methods described in chapter 3 are used to study the physical solubilities of single gases in ionic liquids (ILs). Chapter 6 provides the results of the Monte Carlo simulations that were used to compute the solubility of single gases $CO_2$, $CH_4$, CO, $H_2$, $N_2$, $H_2S$ in the IL 1-butyl-3-methylimidazolium bis(trifluoromethylsulfonyl)imide [bmim][$Tf_2N$] using the CFCMC method. The predicted gas solubilities and Henry constants are in good agreement with experimental data. The MC simulations correctly predict the experimentally observed solubility trend, which obeys the following order: $H_2S > CO_2 > CH_4 > CO > N_2 > H_2$. The $CO_2/CH_4$, $CO_2/CO$, $CO_2/N_2$, $CO_2/H_2$ and $CO_2/H_2S$ selectivities relevant for the pre-combustion $CO_2$ capture process were calculated from the ratio of pure gas Henry constants. The results indicate that [bmim][$Tf_2N$] can effectively capture $CO_2$ at pre-combustion conditions, but synthesis gas should be desulfurized prior to $CO_2$ removal, because $H_2S$ is three times more soluble than $CO_2$. We have shown that molecular simulations can be used to predict gas solubilities in complex systems like ILs.

There is a large demand in the industry for new solvents which are more efficient, less toxic and corrosive and are cheaper than the existing solvents. Designing such solvents is not straightforward. Extensive tests need to be performed to test the efficiency, toxicity, capacity, etc. which are challenging and time consuming. We feel that having efficient, accurate and fast tools to screen a large number of solvent molecules to find promising solvents will enable the early deployment of the new solvents in industry. The molecular simulation methods we have described in this thesis may be that perfect tool.

# Samenvatting

De toename van broeikasgassen is verantwoordelijk voor de opwarming van de aarde in de afgelopen jaren. Een groot deel van de uitgestoten broeikasgassen bevat koolstofdioxide ($CO_2$). De opvang van koolstofdioxide, het transport, en opslag is de meest veelbelovende methode om de opwarming van de aarde te matigen. Koolstofdioxide wordt voornamelijk uitgestoten als rookgassen van energiecentrales die op kolen, olie, en aardgas draaien. Post-combustion $CO_2$ opvang processen gebruiken hoofdzakelijk chemische oplosmiddelen zoals monoethanolamine (MEA) om $CO_2$ uit rookgas af te vangen. De regeneratie van de $CO_2$ gebonden oplosmiddelen is een energie-intensieve proces en zorgt voor een afname van het rendement van de energiecentrale. Andere factoren zoals de volatiliteit, corrosiviteit, toxiciteit, en de kosten van het oplosmiddel zijn essentieel voor het selecteren van het juiste oplosmiddel voor post-combustion opvang. Chemische oplosmiddelen zoals monoethanolamine worden sinds de jaren '60 veelal gebruikt in de industrie. Er is vraag naar nieuwe oplosmiddelen welke minder energie-intensief, toxisch, en corrosief zijn dan de bestaande oplosmiddelen in de industrie. Het ontwerpen van oplosmiddelen is een uitermate uitdagend probleem, omdat er miljoenen potentiele moleculen zijn die als oplosmiddel gebruikt kunnen worden voor post-combustion $CO_2$ opvang. Dit maakt het uitermate lastig om het beste oplosmiddel met behulp van experimenten te vinden. In dit proefschrift ontwikkelen we geavanceerde technieken en methoden die in potentie gebruikt kunnen worden om een groot aantal moleculen te screenen en veelbelovende oplosmiddelen te selecteren. Bestaande moleculaire simulatie methoden zijn ontoereikend om de chemisorptie en diffusie van $CO_2$ in vloeibare oplosmiddelen te beschrijven. We hebben nieuwe methoden ontwikkeld om de verschillende processen die tussen de $CO_2$ en het oplosmiddel moleculen plaatsvinden te beschrijven.

Om de interacties tussen $CO_2$ en de verschillende oplosmiddelen te beschrijven is het noodzakelijk om de verschillende thermodynamische grootheden, dat wil zeggen oplosbaarheden en diffusie van $CO_2$ in de oplosmiddelen, te kunnen beschrijven. De kennis van Fick diffusiecoëfficiënten is belangrijk voor het ontwerpen van reactoren en andere apparaten in de procesindustrie. De thermodynamische factor is nodig om gradiënten in de chemische potentiaal te kunnen converteren naar concentratie gradiënten. Bestaande methoden om thermodynamische factoren en Fick diffusiviteiten uit te rekenen zijn inefficiënt, onnauwkeurig of vereisen een niet-triviale interpretatie van de resultaten. In hoofdstuk 2 hebben we een nieuwe aanpak gepresenteerd om de matrix van de thermodynamische factoren $[\Gamma]$ van $n$-componenten systemen uit te rekenen door gebruik te maken van de zogenaamde "Permuted Widom particle insertion" methode. Het belangrijkste voordeel van onze aanpak is dat we maar één simulatie nodig hebben om de matrix van de thermodynamische factoren $[\Gamma]$ uit te rekenen. We hebben de thermodynamische factoren van binaire en ternaire Lennard-Jones systemen uitgerekend en de resultaten vergeleken met de thermodynamische factoren verkregen door de activiteitcoëfficiënten numeriek te

differentiëren en eveneens vergeleken met het fysisch-gebaseerde NRTL model. De resultaten van de thermodynamische factoren verkregen uit de verschillende methoden zijn met elkaar in overeenstemming. De "Permuted Widom particle insertion" methode dient ook als een onafhankelijk test om de toepasbaarheid van de nieuw geformuleerde Kirkwood-Buff theorie voor gesloten systemen toegepast op zout oplossingen te bevestigen.

Moleculaire simulaties in 'open ensembles' zijn uitermate geschikt om thermodynamische eigenschappen van systemen met $CO_2$ uit te rekenen. De efficiëntie en nauwkeurigheid van Monte Carlo methoden in 'open ensembles' zijn sterk afhankelijk van de kans op succesvolle 'insertions' en 'deletions' van moleculen. Bij hoge dichtheden zijn deze kansen heel erg laag, omdat moleculen meestal met elkaar overlappen. Geavanceerde methoden zoals Configurational-Bias Monte Carlo (CBMC) en de Continuous Fractional Component Monte Carlo (CFCMC) zijn ontwikkeld om de efficiëntie van de 'insertions' bij hoge dichtheden te verhogen. In hoofdstuk 3 vergelijken we de efficiëntie van CBMC en CFCMC voor systemen met hoge dichtheden. We hebben tevens een nieuw methode ontwikkeld die een combinatie is van Continuous Fractional Component Monte Carlo en Configurational-Bias (CB/CFCMC). We hebben de acceptatieregels voor deze methode in verschillende ensembles afgeleid en deze methode is vergeleken met CBMC en CFCMC. We vinden dat bij gemiddelde en hoge dichtheden de efficiëntie van 'insertion' als volgt is CB/CFCMC > CFCMC > CBMC > MC. CB/CFCMC heeft een duidelijk voordeel voor lange ketenmoleculen, omdat het niet nodig is om ideale gas configuraties te genereren voor de CFCMC insertions. Hoewel het CBMC gedeelte rekentijd kost, wijken de moleculaire configuraties van lange ketens in toenemende mate af van ideale gas configuraties. In dit geval zal CFCMC inefficiënt zijn, terwijl CB/CFCMC wel geschikt is omdat het molecuul atoom voor atoom wordt gegroeid. Deze methoden zijn uitgebreid gebruikt in ons onderzoek.

Het onderzoek van het chemisorptie proces van $CO_2$ door middel van chemische oplosmiddelen wordt gedomineerd door de reacties van $CO_2$ met monoethanolamine (MEA) en water. Voor een compleet moleculair inzicht in hoe chemische absorptie werkt, is het verkrijgen van de 'equilibrium speciation' van de verschillende moleculen en bestudering van verschillende reactie mechanismen noodzakelijk. In hoofdstuk 4 zijn Monte Carlo simulaties in de Reaction Ensemble en de Continuous Fractional Component methode (RxMC/CFC) gebruikt om de 'equilibrium speciation' van alle componenten die relevant zijn voor de chemisorptie van $CO_2$ in waterige MEA oplossingen uit te rekenen. De RxMC/CFC methode in combinatie met het osmotisch ensemble is gebruikt om de absorptie isothermen van $CO_2$ in een waterige MEA oplosmiddel uit te rekenen. Deze resultaten zijn in uitstekende overeenstemming met de experimentele resultaten. Deze RxMC/CFC methode biedt de mogelijkheid om het effect van oplosmiddelen op chemische reacties te onderzoeken. Chemisorptie van $CO_2$ in verschillende oplosmiddelen, evenwichtsconcentraties en absorptie isothermen kunnen met behulp van computersimulaties worden verkregen. Enkel thermodynamica moet hier in beschouwing worden genomen en de verschillende transition states en reactie mechanismen kunnen worden genegeerd. De RxMC/CFC methode kan ook gebruikt worden om het effect van de chemische eigenschappen

van amines te bestuderen, bijvoorbeeld door functionele groepen toe te voegen aan het amine.

Het voorspellen van fysische oplosbaarheden en diffusie coefficiënten van $CO_2$ in chemische oplosmiddelen door middel van. experimenten is uitermate moeilijk, omdat diffusie en absorptie van $CO_2$ in een chemische oplosmiddel gelijktijdig plaatsvinden. Door de reacties van $CO_2$ met de chemische oplosmiddelen is de gemeten oplosbaarheid van $CO_2$ in experimenten de totale oplosbaarheid. De totale oplosbaarheid is een combinatie van fysische en chemische absorptie. De zogenaamde $CO_2/N_2O$ analogie, waarbij $CO_2$ wordt vervangen door een moleculair vergelijkbaar $N_2O$ molecuul wordt gebruikt om fysische oplosbarheden en diffusiecoefficiënten uit te rekenen. Op deze manier worden de eigenschappen van $CO_2$ via $N_2O$ geschat. In hoofdstuk 5 hebben we de $CO_2/N_2O$ analogie gevalideerd door middel van moleculaire simulaties. Moleculaire simulatie is de enige manier om deze analogie te valideren, omdat deze in tegenstelling tot experimenten toestaan om reacties aan of uit te zetten. De CFCMC methode in het osmotisch ensemble en MD simulaties werden gebruikt om bij 303 K respectievelijk de Henry coëfficiënten en diffusie coefficiënten van $CO_2$ en $N_2O$ in water, ethanol, *n*-heptane, en een 30% MEA oplossing (met $CO_2$-MEA-$H_2O$ reacties uitgezet) te voorspellen. We hebben gevonden dat de Monte Carlo simulaties de CO2/N2O oplosbaarheden in de onderzochte oplosmiddelen correct voorspellen. De oplosbaarheid van $CO_2$ in de oplosmiddelen volgt de volgende trend: heptane > ethanol > 30% MEA (zonder chemische reacties) > water. $CO_2$ en $N_2O$ diffusiecoefficiënten in deze oplosmiddelen werden eveneens correct voorspeld door Moleculaire Dynamica simulaties: heptane > ethanol > water > 30% MEA (zonder chemische reacties). De simulatieresultaten tonen aan dat de $CO_2/N_2O$ analogie geldig is voor water en een 30% MEA (zonder reacties) oplossing bij 303 K, dit alles binnen een foutenmarge van 10%. We hebben extra simulaties uitgevoerd om te onderzoeken wat et effect is van een chemische reactie tussen $CO_2$ en MEA op het fysische oplosbaarheid en diffusiecoefficient van $CO_2$ heeft. De simulatieresultaten laten zien dat de fysische oplosbaarheid en de diffusiecoefficient van $CO_2$ lager zijn in systemen met reactie producten van $CO_2$ en MEA.

De Monte Carlo methoden beschreven in hoofdstuk 3 zijn gebruikt om fysische oplosbaarheden van pure gassen in ionic liquids (ILs) te bestuderen. Hoofdstuk 6 geeft een overzicht van de CFCMC simulaties die werden gebruikt om oplosbaarheden van de zuivere gassen $CO_2$, $CH_4$, CO, $H_2$, $N_2$, $H_2S$ in de IL 1-butyl-3-methylimidazolium bis(trifluoromethylsulfonyl)imide [bmim][$Tf_2N$] uit te rekenen. De voorspelde gas oplosbaarheden en Henry constanten zijn in goede overeenstemming met de experimentele data. De MC simulaties voorspellen de in de experimenten waargenomen trend voor de oplosbaarheid: $H_2S > CO_2 > CH_4 > CO > N_2 > H_2$. De verhouding van de Henry constanten voor de zuivere gassen werden gebruikt om de relevante selectiviteiten $CO_2/CH_4$, $CO_2$/CO, $CO_2/N_2$, $CO_2/H_2$, en $CO_2/H_2S$ voor het pre-combustion $CO_2$ opvang proces uit te rekenen. De resultaten tonen aan dat [bmim][$Tf_2N$] effectief $CO_2$ kan opvangen bij pre-combustion condities. Echter, het synthese gas moet eerst ontzwaveld worden, omdat $H_2S$ drie keer beter oplost dan $CO_2$. We laten zien dat moleculaire simulaties gebruikt kunnen worden om gas oplosbaarheden in complexe systemen zoals ILs te voorspellen.

Er is een grote vraag vanuit de industrie naar nieuwe oplosmiddelen die efficiënter, minder toxisch en corrosief, en goedkoper zijn dan de bestaande oplosmiddelen. Het ontwerpen en selecteren van zulke oplosmiddelen is niet eenvoudig. Uitdagende en tijdrovende experimenten moeten worden uitgevoerd om de efficiency, toxiciteit, capaciteit en dergelijke, te testen. Een efficiënte, accurate, en snelle tool zal bijdragen om een groot aantal oplosmiddelen te screenen en hierdoor veelbelovende kandidaten te vinden. Dit zal de vroegtijdige ingebruikname van nieuwe oplosmiddelen in de industrie bevorderen. De moleculaire simulatie methoden beschreven in dit proefschrift kan hiervoor een belangrijke bijdrage leveren

# Curriculum Vitæ

Sayee Prasaad Balaji was born in 1986, in Chennai, India. He started his long academic career as an undergraduate in the National Institute of Technology, Tiruchirappalli, India in 2004. He received his Bachelor of Technology degree in Chemical Engineering in 2008. He then continued his pursuit of knowledge by enrolling in Hamburg University of Technology, Germany in 2008 for his Master of Science in Process Engineering. It was during his time in Hamburg that he came across the group of Prof. Dr. Frerich Keil working in molecular simulations which interested him greatly. He then visited the MolSim group in University of California, Berkeley from 2009 to 2010 to develop his skills in classical molecular simulations under the supervision of Prof. Berend Smit. After successfully graduating from Hamburg University of Technology with a Master of Science in 2010, he joined Delft University of Technology, The Netherlands as a PhD student in 2010 in the Engineering Thermodynamics group of Prof. dr. ir. Thijs Vlugt. During his PhD, he enjoyed a fruitful collaboration with the group of Dr. David Dubbeldam at the University of Amsterdam. His research focused on developing advanced Monte Carlo techniques to study gas-liquid separations and to design newer solvents. After his PhD in 2015, he joined the Gasification group at Shell Global Solutions International, Amsterdam.

# List of Journal Publications

12. Ramdin M.; **Balaji S. P.**; Vivent-Luna J. M.; Torres-Knoop A.; Chen Q.; Dubbeldam D.; Calero S.; de Loos T. W.; Vlugt T. J. H., *Computing bubble-points of $CO_2/CH_4$ gas mixtures in ionic liquids from Monte Carlo simulations*, Fluid Phase Equilibria, in press

11. Ramdin M.; Chen Q.; **Balaji S. P.**; Vicent-Luna J. M.; Torres-Knoop A.; Dubbeldam D.; Calero S.; de Loos T. W.; Vlugt T. J. H., *Solubilities of $CO_2$, $CH_4$, $C_2H_6$ and $SO_2$ in Ionic Liquids and Selexol from Monte Carlo Simulations*, J. Comput. Sci., in press

10. Ramdin M.; **Balaji S. P.**; Torres-Knoop A.; Dubbeldam D.; de Loos T. W.; Vlugt T. J. H., *Solubility of Natural Gas Species in Ionic Liquids and Commercial Solvents: Experiments and Monte Carlo Simulations*, J. Chem. Eng. Data, in press

9. **Balaji S. P.**; Gangarapu S.; Ramdin M.; Torres-Knoop A.; Zuilhof H.; Goetheer E. L. V.; Dubbeldam D.; Vlugt T. J. H., *Simulating the reactions of $CO_2$ in aqueous monoethanolamine solution by Reaction Ensemble Monte Carlo using the Continuous Fractional Component method*, J. Chem. Theory Comput. **11**, 2661-2669 (2015)

8. Chen Q.; **Balaji S. P.**; Ramdin M.; Gutierrez-Sevillano J. J.; Bardow A.; Goetheer E. L. V.; Vlugt T. J. H., *Validation of the $CO_2/N_2O$ Analogy Using Molecular Simulation*, Ind. Eng. Chem. Res. **53**, 18081-18090 (2014)

7. Ramdin M.; **Balaji S. P.**; Vicent-Luna J. M.; Gutierrez-Sevillano J. J.; Calero S.; de Loos T. W.; Vlugt T. J. H., *Solubility of the Precombustion Gases $CO_2$, $CH_4$, CO, $H_2$, $N_2$, and $H_2S$ in the Ionic Liquid [bmim][$Tf_2N$] from Monte Carlo Simulations*, J. Phys. Chem. C **118**, 23599-23604 (2014)

6. Torres-Knoop A.; **Balaji S. P.**; Vlugt T. J. H.; Dubbeldam D., *A Comparison of Advanced Monte Carlo Methods for Open Systems: CFCMC vs CBMC*, J. Chem. Theory Comput. **10**, 942-952 (2014)

5. Schnell S. K.; Englebienne P.; Simon J. M.; Krüger P.; **Balaji S. P.**; Kjelstrup S.; Bedeaux D.; Bardow A.; Vlugt T. J. H., *How to apply the Kirkwood–Buff theory to individual species in salt solutions*, Chem. Phys. Lett. **582**, 154-157 (2013)

4. **Balaji S. P.**; Schnell S. K.; Vlugt T. J. H., *Calculating Thermodynamic Factors of Ternary and Multicomponent Mixtures using the Permuted Widom Test Particle Insertion Method*, Theo. Chem. Acc. **132**, 1-8 (2013)

3. **Balaji S. P.**; Schnell S. K.; McGarrity E. S.; Vlugt T. J. H.,*A Direct Method for Calculating Thermodynamic Factors for Liquid Mixtures using the Permuted Widom Test Particle Insertion Method*, Mol. Phys. **111**, 287-296 (2013)

2. Zimmermann N. E. R. ; **Balaji S. P.**; Keil F. J., *Surface Barriers of Hydrocarbon Transport Triggered by Ideal Zeolite Structures*, J. Phys. Chem. C **116**, 3677-3683 (2012)

1. Brüggemann T. C.; Przybylski M. D.; **Balaji S. P.**; Keil F. J., *Theoretical Investigation of the Mechanism of the Selective Catalytic Reduction of Nitrogen dioxide with Ammonia on H-form Zeolites and the Role of Nitric and Nitrous Acids as Intermediates*, J. Phys. Chem. B **114**, 6567-6587 (2010).

# Acknowledgement

The acknowledgement section is usually written at the end of the dissertation, because it signifies that your time as a PhD researcher has come to an end. Every PhD journey has its own fair share of crests and troughs, but it would have been incomplete if not for the invaluable guidance and support from many people. During my time as a PhD researcher, I had the good fortune to be associated with many people who truly made my PhD journey very enjoyable and memorable and I am very grateful for that. While I would like to thank everyone, I will without doubt, forget to mention some people. I apologize to those that I might forget to mention.

First and foremost, I would like to thank my promoters, Prof. dr. ir. Thijs Vlugt and Dr. David Dubbeldam for their excellent guidance. Thijs, you are an exceptional researcher. I remember our discussions on molecular simulations and thermodynamics and it was then I came to understand the meaning of the term "sky is the limit". I greatly admire your "out-of-the-box thinking" approach to solving many problems. The occasion when you helped me sort out my accommodation issues showed that you truly cared about the well-being of your students. Any acknowledgement about you will be incomplete if I do not thank you for your extremely fast comments and email replies, even at midnight on Sundays.

David, I came to know about you from Thijs as the person who wrote the RASPA code. A quick glance at the program demonstrated the kind of researcher you are - remarkable and methodical. One can just read the program and understand Monte Carlo and molecular dynamics. Our discussions, both in Amsterdam and Delft made me look at molecular simulations from a different perspective.

At this juncture, I would also like to thank a few more people: Prof. Yashonath Subramanian for introducing me to the world of molecular simulations; Prof. Frerich Keil who made the abstract world of statistical thermodynamics very interesting and to Prof. Berend Smit for giving me a wonderful opportunity to work in his lab at Berkeley. I would like to thank my physics teacher and mentor, Mr. C. S. Ravishankar for inspiring hundreds of young minds, including myself, to be inquisitive and to pursue a career in science. Sir, you have been a great teacher and mentor to me and I can say that everything that I am now started one fine Sunday afternoon in Aminjikarai.

I thank my colleagues in CATO and ETh, Process & Energy for the numerous discussions. In random order, I thank Prof. dr. Hans Zuilhof, Dr. Earl Goetheer, Univ.-Prof. Dr.-Ing. Andre Bardow, Dr. Ton Marcelis, Dr. ir. Theo de Loos, Dr. Brian Tighe, Prof. dr. Wim Buijs, Dr. ir. Carlos Infante Ferreira for their valuable inputs. Many thanks to the support staff Judith, Ilona, Leslie, Eveline, Helma, Rob for all their help.

My PhD journey would have been quite uneventful if not for my office colleagues. Both Leeghwaterstraat 44 and Leeghwaterstraat 39 were filled with great memories. Special thanks to Mahinder, Marloes, Sondre, Somnath, Dennis for providing excellent topics for discussion during the coffee breaks. The old office could have never

been more fun without Thijs vW, Bernardo, Albert, Samir, Guido, Pablo, Erin, Xin, Fan, Christian, Nobert and David. Special thanks to Hassan, Mariette, Aditya TT, Yash, Tiggy, Uttiyo, Jurriaan, Julia, Hongxia, Tim, Ali, Frank, Juanjo, Rohit, Weiwei and Lalit for making the new office as enjoyable as the old one. I thank Satesh, Alex, Ariana and Jose Manuel for their critical input and fruitful discussions.

Delft was a wonderful place where many life-long friendships were forged. Many thanks to Aditya, Harish, Jaikishen, Bharadwaj, Supraja, Nirupa, Sriram, Saashwath, Akshey, Jeyakrishna, Anand, Vasu, Gautam, Kamakshi for all the wonderful times we have had over the past 4 years.

Dear Amma, Appa, Thatha and Thetha, I owe this thesis to you. I cannot imagine the unconditional love, affection and the support that I have received from you over the last 28 years. It has been your dream, more than mine, to pursue research, and I am glad to have shared the dream as well. Dear Haripriya, you have been a pillar of strength to me and shown me unconditional love and support. I am grateful to the long hours that you spent proof-reading my thesis. This thesis would not be complete if not for you. I thank my in-laws for all their support and encouragement as well.

Finally, I offer my namaskarams to Mama, without whom this would not have been possible.